Doctoral Dissertation
Doctoral Program in Civil and Environmental Engineering (XXXII cycle)

Turbulence Properties of Smooth-Bed Open-Channel Flows with and without Collinear Gravity Waves

By

Cosimo Peruzzi

******

Supervisor(s):
Prof. Costantino Manes, Supervisor
Prof. Davide Poggi, Co-Supervisor
Prof. Luca Ridolfi, Co-Supervisor

Doctoral Examination Committee:
Prof. Paolo Blondeaux, Università degli Studi di Genova, Italy
Prof. Maurizio Brocchini, Referee, Università Politecnica delle Marche, Italy
Prof. Carlo V. Camporeale, Politecnico di Torino, Italy
Prof. Michele Guala, University of Minnesota, USA
Prof. Vladimir I. Nikora, Referee, University of Aberdeen, UK

Politecnico di Torino
2020

Declaration

I hereby declare that, the contents and organisation of this dissertation constitute my own original work and does not compromise in any way the rights of third parties, including those relating to the security of personal data.

Cosimo Peruzzi
2020

* This dissertation is presented in partial fulfillment of the requirements for **Ph.D. degree** in the Graduate School of Politecnico di Torino (ScuDo).

To my beloved father Sergio (1956 - 2020)

Acknowledgements

The road to the PhD degree is not straight but turns out to be rather tortuous and full of unexpected obstacles. Without the right guide, one risks giving up at the first challenge or throwing the towel in prematurely. On this journey I was lucky enough to have not one but three guides.

The first guide was Costantino Manes, who supported me all the way, sharing burdens, doubts and joys. He believed in me more than anybody else and helped me grow steadily by both making me notice my mistakes and praising me for my achievements. He influenced me with his passion for experimental fluid mechanics in such a way that it will be very difficult for another subject to find its way so deeply into my heart.

The second guide was Davide Poggi, who led me in the impervious environment of the hydraulic laboratory. The Giorgio Bidone Hydraulic Laboratory is a kind of playground for a hydraulic engineer, but it is necessary to have a great competence in order to achieve results. He shared with me some crucial information to update the wave open-channel flume used for the experiments.

The third guide was Luca Ridolfi, who has the remarkable capability to motivate someone with just a few words, a call or an email. His knowledge helped me to go beyond the obstacles and created that sense of wonder for every new discovery. Thanks for all the words of encouragement and advice.

Furthermore, I had the possibility to work with Bharathram Ganapathisubramani that hosted me for four months at the University of Southampton (United Kingdom). I really appreciate his passionate way of working and I will have a fond memory of all his research group.

A special thanks also to Davide Vettori for the dedication that he has shown in correcting some parts of this dissertation and for the stimulating discussions arisen.

I dedicate my efforts to my family that is always at my side in good and bad times. Unfortunately, father, you are not more here to see the end of this journey, but I know that you continue to see me through a ray of sunshine and to caress me through a gust of wind.

In addition, the unique environment of PhD students, post-docs and fellow researchers at the DIATI department creates a sort of second family. I shared everything with you, guys! Each of you left me with or taught me something that I will always remember. A special mention goes to my office mates (Matteo, Sofia, Irene and Tiziano), the Lab group and Melissa, who has irreparably entered my life.

Finally, I am also thankful to my lifetime friends, who cheered me up even from afar, even though they have often good-naturedly made fun of me because of my passion for water sciences.

Abstract

Turbulence plays a key role in most of the processes related to open-channel flows, e.g. rivers, tidal channels, irrigation canals and waterways. For instance, the transport and mixing of substances, the scour around submerged hydraulic structures, and the design of more performing hydro-kinetic turbine are some of the fields that benefit from a better understanding of turbulent properties in open-channel flows.

Among the various coherent structures that populate wall-bounded flows, Large- and Very-Large-Scale Motions (LSMs and VLSMs) are attracting significant scientific interest, not only from a merely academic perspective but also for their practical implications. Although dynamics and evolution of LSMs and VLSMs have been investigated in so-called canonical wall-flows (i.e. boundary layer, pipe and closed-channel flow), what happens to them in open-channel flows has been overlooked so far. In order to investigate the scaling of such large scale structures, novel experiments were carried out at the Giorgio Bidone Hydraulic Laboratory (Politecnico di Torino) where turbulent open-channel flows could be generated in a large-scale flume facility with and without the presence of collinear waves. The idea of perturbing open-channel flows with waves steams from the fact that waves and currents coexist in many environments and hence their interaction is relevant for many of the previously mentioned engineering applications. Moreover, gravity waves can be interpreted as perturbations whose effects can clarify issues related to turbulence in more canonical (i.e. without waves) open-channel flows. Longitudinal and vertical velocity components were measured at a high sampling frequency using a 2-D Laser Doppler Anemometer (LDA).

The first set of experiments was devoted to investigating the scaling of LSMs and VLSMs in absence of waves. Results indicate that, contrary to other wall flows, in smooth-bed open-channel flows the presence of both LSMs and VLSMs is detectable from 1-D pre-multiplied spectra even at relatively low values of the von Kármán number Re_{τ}. Moreover, the spectral footprint of such scales is present across the entire depth of the investigated flows, whereas, in closed-channels, pipes and boundary layers, is limited to 60% of their vertical extension. Results also confirm that, while LSMs' wavelength follows the same scaling as reported for other wall flows, VLSMs' wavelength depends strongly on the aspect ratio of the flow.

In the second set of experiments, a benchmark open-channel flow was perturbed with collinear gravity waves with varying wave amplitude and frequency. From the velocity signal time-series, the wave and turbulent components were extracted using the Empirical Mode Decomposition (EMD) technique. When the appropriate outer velocity and length scales were employed, it was found that the flows exhibited two distinct regions: (i) a current-dominated flow region near the bed, where the turbulence shares many analogies with that typical of wall-flows; (ii) a wave-dominated flow region, where turbulence is fed by a Langmuir-type mechanism near the free-surface. Within the current-dominated flow region, the longitudinal turbulent intensities are weakly affected by the passage of the gravity waves, whereas the vertical turbulent intensities are strongly damped. This damping is more evident as the vertical wave strength (wave amplitude times wave frequency) increases with respect to the shear velocity of the current. From the spectral analysis, it is argued that the VLSMs presence vanishes when the wave strength exceeds a certain value, likely because the orbital wave motion inhibits the trigger mechanism for VLSMs. Conversely, in the wave-dominated flow region, new spectral peaks at wavelengths commensurate to those normally associated with LSMs and VLSMs become visible as the wave steepness increases. It is indeed speculated that these long structures are Langmuir-type cells.

Contents

List of Figures x

List of Tables xviii

Nomenclature xx

1 Introduction 1

1.1 Overview and background 1

1.2 Aims and objectives 5

1.3 Dissertation outline 5

1.4 Novel contributions and publications 6

2 Turbulence properties in open-channel flows over smooth-bed: velocity statistics and spectral analysis 7

2.1 Introduction 8

2.1.1 Large- and Very-Large-Scale Motions in canonical wall-bounded flows: a brief review 12

2.2 Laboratory set-up and methodology 16

2.3 Experimental hydraulic conditions 26

2.4 Estimation of the shear velocity 31

2.5 Results 35

2.5.1 One-point statistics 35

2.5.2 Spectral analysis of the u-component 42

2.6 Conclusion 51

3 The influence of collinear gravity waves on turbulence in smooth-bed open-channel flows 53

3.1 Introduction 54

3.2 Methodology 61

3.2.1 Equipment and hydraulic conditions 61

3.2.2 Waves characterisation 69

3.2.3 Signal Decomposition 78

3.3 Results 89

3.3.1 Mean velocity profiles 89

3.3.2 Second order velocity moments 96

3.3.3 Quadrant Analysis 102

3.3.4 Spectral analysis 105

3.4 Summary and discussion 109

4 Conclusions and future works 114

4.1 Recommendations for future studies 117

References 119

List of Figures

1.1 Coherent structures in open-channel flows and associated phenomena (adapted from Adrian and Marusic, 2012). The filaments in cyan and blue indicate large-scale structures. 3

2.1 Outer-scaled (a) spectrum and (b) pre-multiplied spectrum of the streamwise velocity fluctuation in a turbulent pipe flow ($y/R = 0.084$ and $Re_\tau \approx 2000$, where R is the pipe radius). In pannel (a) also the Townsend -1 and Kolmogorov $-5/3$ spectrum scalings are reported for comparison, while in pannel (b) the LSM and VLSM spectral peaks are hilighted. Figure adapted from Guala et al. (2006). 12

2.2 Countour plots of streamwise velocity fluctuations u' (a) in a turbulent pipe flow ($y/R = 0.15$ and $Re_\tau = 3472$) and (b)–(d) in a turbulent closed-channel flow ($y/\delta_{CC} = 0.08$, $y/\delta_{CC} = 0.14$ and $y/\delta_{CC} = 0.56$, respectively, and $Re_\tau = 3178$, where δ_{CC} is the half-channel height). The measurement were carried out by using a rake of hot-wire probes (15 for the pipe and 10 for the closed-channel). Figure adapted from Monty et al. (2007). . . . 13

2.3 Contour maps of the pre-multiplied 1-D spectra of the stremwise velocity fluctuation as a function of streamwise wavelength λ_x and the distance from the wall y for (a)–(b) a turbulent boundary layer, (c)–(d) a closed-channel flow, and (e)–(f) a pipe flow. The Re_τ is around 3000 for each case. The pannels at the left-and side have a logaritmic x-axix, while the pannels at the rigth-hand side have a linear x-axix. Figure adapted from Monty et al. (2009). 14

2.4 Outer-scaled LSM and VLSM wavelegth peaks, where δ is the appropriate outer-length scale. Symbols are referred to turbulend boundary layer, closed-channel and pipe flow experiments, see Balakumar and Adrian (2007) for more detailed information. . 16

2.5 Photo of the large-scale open-channel flume at the Giorgio Bidone Hydraulics Laboratory of the Politecnico di Torino (upstream-downstream view). 17

2.6 Technical overview of the flume used for the experiments: (a) sketch of the whole hydraulic circuit; (b) and (c) details of the inlet flow conditions and the test section, respectively. Panel (c) also shows the system of coordinate axes chosen in the present study (i.e. the streamwise x, wall-normal y and spanwise z directions) and defines the flow depth h and the channel width W. Please note that the coordinate x has its origin at the downstream end of the ramp (see panel b). 18

2.7 Velocity streamlines pattern computed from a 3-D CFD simulation of the fifth-order polynomial-shaped ramp (top view, flow from left to right). 19

2.8 Details of the test section configuration. 22

2.9 Dantec Dynamics 2-D LDA measurement system at the test section. It can be noted how the vertical laser beam near the wall passes through the thin gap between the concrete slabs. . . 23

2.10 Identification of the origin the vertical coordinate: (A) the LDA laser beams are approaching the extremity of sharp point gauge; (B) the LDA measurement volume perfectly coincide with the extremity of sharp point gauge. 25

2.11 Estimated β values along the channel flume. The grey vertical lines indicate the positions of the five ultrasonic gauges. 30

2.12 Variation of the Ψ function for the various tests. 33

2.13 Inner scaling: (a) normalised streamwise mean velocity; (b) normalised standard deviation of the streamwise velocity fluctuations; (c) normalised standard deviation of the wall-normal velocity fluctuations; (d) normalised Reynolds shear stress. The dashed and continuous lines represent the linear and the log law of the wall. 36

2.14 Outer scaling: (a) normalised streamwise mean velocity; (b) normalised standard deviation of the streamwise velocity fluctuations; (c) normalised standard deviation of the wall-normal velocity fluctuations; (d) normalised Reynolds shear stress. The continuous line is the velocity-defect law. 37

2.15 Variance of streamwise turbulence in: (a) inner and (b) outer scaling. The continuous line is the Townsend-Perry log law (Eq. (2.14)). Only the tests with a $Re_\tau > 1700$ exhibit a logarithmic zone. 39

2.16 Measured (a) streamwise skewness; (b) wall-normal skewness; (c) streamwise kurtosis; (d) wall-normal kurtosis. 40

2.17 Contour maps of the outer-scaled pre-multiplied 1-D spectra of the longitudinal velocity component $(E_{xx}k_x/u_\tau^2)$ as a function of non-dimensional streamwise wavelength (λ_x/h) and distance from the wall (y/h). The dashed lines indicate the bed-normal elevations where measurements were taken. 43

2.18 Pre-multiplied 1-D spectra of the longitudinal velocity component taken at $y/h = 0.2$. The red line indicates $\lambda_x/h = 14$. 45

2.19 LSM and VLSM h-normalised wavelengths peaks in the pre-multiplied 1-D spectra of the longitudinal velocity component. The light grey markers indicate situations where LSM or VLSM peaks were not clearly detectable because poorly pronounced. The red line corresponds to the relation between normalised VLSM-wavelengths and normalised elevations proposed by Monty et al. (2009) for duct flows. 46

2.20 (a) Spectral energy associated with LSM peaks normalised with u_τ^2; (b) spectral energy associated with VLSM peaks normalised with u_τ^2. The light grey markers have the same meaning as described in Fig. 2.19. The error bars indicate the confidence interval bounds (with a 95% confidence level). 48

2.21 (a) Spectral energy associated with LSM peaks normalized with σ_u^2; (b) spectral energy associated with VLSM peaks normalized with σ_u^2. The light grey markers have the same meaning as described in Fig. 2.19. The error bars indicate the confidence interval bounds (with a 95% confidence level). 48

2.22 Pre-multiplied 1-D spectra of the longitudinal velocity fluctuations for tests 5−5d at eight different outer locations. Test 5 was measured in the centreline of the flume, while tests 5a, 5b, 5c and 5d were measured at z/W = 0.08, 0.16, 0.24 and 0.33, respectively. Panels (a)−(h) refer to spectra measured at different bed-normal elevations y/h. Note the different y-axes limits of panels (a), (g) and (h) with respect to the others. . . . 50

3.1 Evidence of the non-linear interaction between waves and current (data from Kemp and Simons (1982), tests CA and WCA5, smooth bed and waves propagating with the current). The mean longitudinal velocity profiles are referred to the current alone case (A), the current plus waves case (B), and the difference between the profile B and A (C). The discrepancy of C with respect to the wave-induced net mass transport (determined with the Stoke drift formula, Eq. (3.1)) in the case of waves alone clearly indicates that the linear superposition does not hold. 57

3.2 Detail of the flume inlet with the piston-type wavemaker (dark green) and the concrete bottom with the steel ramp (dark grey). 61

3.3 Sketch of the ultrasonic gauges (orange circle) and LDA (red square) locations along the open-channel flume. 63

3.4 Image of the checkerboard pattern fixed to the side glass wall of the open-channel flume at the test section. 63

3.5 Range of applicability of the different wave theories (adapted from Qi et al., 2019). The blue markers indicate the WA experiments reported in Tab. 3.1. 65

3.6 (a) Photo of the surface wave profile (case WA−T2); (b) spatial evolution of the surface wave profile for WA−T2. The blue markers represent the free-surface extracted by the image processing. The red solid line represents the Airy linear theory, while the black dashed line represents the Stokes II order theory. 70

3.7 Temporal evolution of the surface wave profile for WA−T2. The blue solid line represents the free-surface measured from the ultrasonic gauge in proximity to the LDA location. The red solid line represents the Airy linear theory, while the black dashed line represents the Stokes II order theory. 71

3.8 Temporal evolution of the surface wave profile for WA−T5. The blue solid line represents the free-surface measured from the ultrasonic gauge in proximity to the LDA location. The red solid line represents the Airy linear theory, while the black dashed line represents the Stokes II order theory. 71

3.9 Wave attenuation along the flume. The black solid line represents the equation (Eq. (3.7)) introduced by Hunt (1952). In particular, the markers represent mean values and the bars are twice the standard deviation. 72

3.10 Coefficient of variation of (a) the wave period, and (b) the wave height. Alongside the WC tests, also the representative WA−2 test is reported for comparison. 75

3.11 Normalised histograms and relative data-estimated probability density functions (PDF) of wave heights for all the WC experiments recorded at gauge 1 (first column) and gauge 4 (second column). 76

3.12 (a) Semi-logarithmic and (b) logarithmic scale representation of the frequency spectrum of the free-water surface for the case WC−T5. 77

3.13 Identification of the signal extrema (blue dots), construction of the upper and lower envelopes and computation of the mean envelope. 81

3.14 Example of EMD application (test WC−T2, $y/h = 0.1$, longitudinal velocity component). In this case, the wave motion is entirely enclosed inside the IMFs number 6, 7 and 8, as it can be seen in Fig. 3.15. Note that only a small portion of the time series is reported. 84

3.15 Fourier spectrum of the original signal (thick black line), IMFs (various coloured lines) and residual (magenta line) reported in Fig. 3.14. The straight red line is the Kolmogorov -5/3 spectrum scaling. 85

3.16 (a) Original signal (blue line) and mean velocity (red line); (b) wave component and (c) turbulent component (test WC−T2, $y/h = 0.1$, longitudinal velocity component). 86

3.17 Spectral representations of the longitudinal velocity measurement at $y/h = 0.03$ for test WC−T2. Black, red and blue lines respectively indicate the turbulent component, the wave component and the reconstructed signal. The main plot shows the spectra in linear scale, while the sub-plot reports the same spectra in a log-log scale. 87

3.18 Vertical profiles of the mean longitudinal velocity component for the CA (current alone) and WC experiments (complete waves plus current signal). 90

3.19 Sketch of a wave with the definitions of the relevant parameters used in the continuity equation. 91

3.20 Normalised mean velocity profiles for the longitudinal component: (a) inner, and (b) outer scaling. In (b) the vertical coordinate is normalised using h_0, which represents the distance from the bottom to the elevation where U reaches its maximum. 93

3.21 The normalised outer length scale h_0 as a function of the dimensionless parameter $a\,f_w/u_{\tau_c}$. Results from Kemp and Simons (1982), Umeyama (2005), Roy et al. (2017) and Zhang and Simons (2019) are reported for comparison. 95

3.22 Dimensional second-order velocity moments. Complete waves plus current signal: (a) standard deviation of the longitudinal velocity; (b) standard deviation of the vertical velocity; (c) shear stresses. Wave component: (d) standard deviation of the longitudinal velocity; (e) standard deviation of the vertical velocity; (f) shear stresses. Turbulent component: (g) corrected standard deviation of the longitudinal velocity; (h) corrected standard deviation of the vertical velocity; (i) Reynolds shear stresses. Note the different x-axis limits of panels (g), (h) and (i) with respect to the others. 97

3.23 Vertical profiles of the mean wall-normal velocity component for the CA (current alone) and WC experiments (complete wave plus current signal). 99

3.24 Normalised second-order moments of the turbulent component. Inner scaling: (a) corrected standard deviation of the longitudinal and (b) vertical velocity; (c) Reynold shear stress. Outer scaling: (d) corrected standard deviation of the longitudinal and (e) vertical velocity; (f) Reynold shear stress. 101

3.25 Distributions of the quadrant contributions to the Reynolds shear stress for each experiment (turbulent component) in outer scaling: (a) CA; (b) WC−T1; (c) WC−T2; (d) WC−T3; (e) WC−T4; and (f) WC−T5. In particular, $\overline{u'v'}_{Q1}$ is the outward interaction, $\overline{u'v'}_{Q2}$ is the ejection, $\overline{u'v'}_{Q3}$ is the inward interaction, and $\overline{u'v'}_{Q4}$ is the sweep. The vertical grey line indicates $y = h_0$. 103

3.26 Ratio between the contribution of quadrant 2 ($\overline{u'v'}_{Q2}$) and quadrant 4 ($\overline{u'v'}_{Q4}$) to the Reynolds shear stress in outer scaling (turbulent component). 104

3.27 Outer-scaled pre-multiplied 1-D spectra of the longitudinal velocity component (complete wave plus current signal). Each panel reports spectra at different elevations for one experimental condition. Black lines identify vertical elevations below h_0 (i.e. in the current-dominated flow region) whereas purple lines above it (i.e. in the wave-dominated flow region). Red and green arrows in panel a) identify spectral peaks associated with LSMs and VLSMs, respectively. Black arrows in panel (f) identify spectral peaks presumably associated with Langmuir-type turbulence in WC experiments; peaks at similar wavenumbers are also observed in panels (c), (d) and (e). 106

3.28 Outer-scaled pre-multiplied 1-D spectra of the vertical velocity component (complete wave plus current signal). Each panel reports spectra at different elevations for one experimental condition. Black lines identify vertical elevations below h_0 (i.e. in the current-dominated flow region) whereas purple lines above it (i.e. in the wave-dominated flow region). 107

3.29 (a) Contours of the transverse stream function associated with the first instability mode as detected by Huang and Mei (2006); (b) contours of the transverse stream function of the second mode of instability detected by Huang and Mei (2006). Figure adapted from Huang and Mei (2006). 110

3.30 Phenomenology of longitudinal vorticity production in wave-current interaction flows (taken from Huang and Mei (2006)). In particular, U_S is the Stokes drift velocity; U_0 is the mean longitudinal current velocity; w_0 is the vertical velocity; ξ_0 is the longitudinal vorticity; ζ_0 is the vertical vorticity; and K is the dimensionless transverse wave number (it is important to note that Huang and Mei (2006) adopts a different coordinate system compared to the one used in this study, see Fig. 2.6c). 111

List of Tables

2.1 Characteristics of the used LDA system (Dantec Dynamics, 2011). 23

2.2 Standard errors of the velocity statistics calculated for Test 1. . 25

2.3 Summary of experiments and associated hydraulic conditions. The columns indicate respectively: the water depth h, the bulk velocity U_b, the shear velocity u_τ, the viscous length scale $\delta_\nu = \nu/u_\tau$ where ν is the kinematic viscosity, the viscous-scaled LDA measurement length $l^+ = d_z u_\tau/\nu$ where d_z is the longest ellipsoidal axis of the LDA measurement volume, the bulk Reynolds number $Re_b = R_h U_b/\nu$ where $R_h = Wh/(W+2h)$ is the hydraulic radius and W is the channel width, the von Kàrmàn number $Re_\tau = hu_\tau/\nu$, the Froude number $Fr = U_b/\sqrt{gh}$ where g is the gravitational acceleration, the aspect ratio W/h and the non-dimensional distance from the inlet x/h. Finally, z/W indicates the normalised spanwise position for the velocity measurements, where z is the spanwise coordinate starting from the flume centreline. 27

2.4 Estimated values of u_τ (in m/s) at the mid cross-section using the Clauser method applied to the measured mean velocity profiles and the empirical approach by Knight et al. (1984). The last row of the table reports the percentage relative error R.E. between the two estimates. 34

3.1 Summary of the hydraulic conditions for the waves alone (WA) cases. The columns indicate, respectively: the mean water depth h; the wave frequency f_w; the wave period $T = 1/f_w$; the characteristic wave amplitude a; the characteristic wave height $H = 2a$; the characteristic wave length L; the relative depth h/L; the wave steepness $\epsilon = ak$, where $k = 2\pi/L$ is the wave number; the relative height H/h and the Ursell number $U_R = HL^2/h^3$. . . 65

3.2 Summary of the hydraulic conditions for the current alone (CA) and waves plus current (WC) cases. The columns indicate, respectively: the mean water depth h; the shear velocity u_τ; the current bulk velocity U_b; the wave frequency f_w; the characteristic wave amplitude $a = H/2$, where H is the wave height; the characteristic wave length L; the longitudinal water particle semi-excursion due to the orbital motion at the bottom A_b; the longitudinal wave orbital velocity at the bottom U_w; the current bulk Reynolds number $Re_b = R_h U_b/\nu$, where R_h is the hydraulic radius and ν is the kinematic viscosity of the water; the wave Reynolds number $RE = A_b^2\omega/\nu$, where $\omega = 2\pi f_w$ is the radial frequency; and the k_s/A_b relative roughness, where k_s is the Nikuradse equivalent sand roughness. Note that the symbol $\upharpoonleft$ denotes values determined in the current alone case (CA, see Tab. 2.3); the symbol ‡ denotes values determined in the waves alone case (WA, see Tab. 3.1); the symbol † denotes values calculated by using the Airy linear wave theory (Dean and Dalrymple, 1991). 66

3.3 Statistics of the surface waves in the case of waves plus current: $\overline{T}$ is the mean period; T_{sd} is the period standard deviation; $CV_T = T_{sd}/\overline{T}$ is the period coefficient of variation; $\overline{H}$ is the mean wave height; H_{sd} is the wave height standard deviation and $CV_H = H_{sd}/\overline{H}$ is the wave height coefficient of variation. The values of $\overline{T}$ and T_{sd} are in seconds, while the values of $\overline{H}$ and H_{sd} are in centimetres. 74

Nomenclature

Acronyms

1-D	One-Dimensional
2-D	Two-Dimensional
3-D	Three-Dimensional
CA	Current Alone
CFD	Computational Fluid Dynamic
EMD	Empirical Mode Decomposition
IMF	Intrinsic Mode Function
LDA	Laser Doppler Anemometer
LSM	Large Scale Motion
PDF	Probability Density Function
PMF	Proto-Mode Function
PIV	Particle Image Velocimetry
RANS	Reynolds-Averaged Navier-Stokes
R.E.	Relative Error
TKE	Turbulent Kinetic Energy
VLSM	Very Large Scale Motion

WA	Wave Alone
WC	Wave plus Current
WCI	Wave Current Interaction

Greek symbols

α	Wave attenuation modulus [-]
β	Open-channel non-uniformity parameter [-]
δ	Characteristic outer-length scale [m]
δ_{BL}	Boundary layer thickness [m]
δ_{CC}	Half-channel height [m]
δ_w	Wave boundary layer thickness [m]
δ_ν	Viscous length scale [m]
ϵ	Wave steepness [-]
η	Water surface elevation [m]
η_A	Water surface elevation predicted by Airy theory [m]
η_{II}	Water surface elevation predicted by Stokes II order theory [m]
η_k	Kolmogorov dissipative length-scale [m]
κ	von Kármán constant [-]
λ_x	Streamwise wavelength [m]
ν	Fluid kinematic viscosity [m^2/s]
Π	Wake strength parameter (Coles' wake parameter) [-]
π	Archimedes' constant [-]
ρ	Fluid density [kg/m^3]

σ_u	Standard deviations of the streamwise velocity or streamwise standard deviations of the waves plus current signal [m/s]
$\sigma_{\tilde{u}}$	Standard deviations of the streamwise wave component [m/s]
$\sigma_{u'}$	Standard deviations of the streamwise velocity [m/s]
$\hat{\sigma}_{u'}$	Corrected standard deviations of the streamwise velocity [m/s]
σ_v	Standard deviations of the wall-normal velocity or wall-normal standard deviations of the waves plus current signal [m/s]
$\sigma_{\tilde{v}}$	Standard deviations of the wall-normal wave component [m/s]
$\sigma_{v'}$	Standard deviations of the wall-normal velocity [m/s]
$\hat{\sigma}_{v'}$	Corrected standard deviations of the wall-normal velocity [m/s]
τ_m	Mean shear stress in wave-current flow [N/m^2]
τ_{max}	Maximum shear stress in wave-current flow [N/m^2]
τ_{tot}	Total shear stress [N/m^2]
τ_0	Wall shear stress [N/m^2]
Ψ	Diagnostic function [-]
ω	Wave radial frequency [Hz]

Latin symbols

A	Wetted area [m^2]
A_b	Wave-induced longitudinal water-particle semi-excursion at the bottom [m]
a	Wave amplitude [m]
B	Constant in the log-law (smooth-wall condition) [-]
B_1	Constant in the velocity-defect law (smooth-wall condition) [-]

CV_H	Coefficient of variation of the wave height [-]
CV_T	Coefficient of variation of the wave period [-]
D	Spheres' diameter [m]
d_x	Ellipsoidal x-axis of the LDA measurement volume [m]
d_y	Ellipsoidal y-axis of the LDA measurement volume [m]
d_z	Ellipsoidal z-axis of the LDA measurement volume [m]
E	Specific energy [m]
$E(f)$	Frequency spectrum [m^2/s]
$E_{xx}(k_x)$	1-D wavenumber spectrum of the streamwise velocity [m^3/s^2]
$E_{yy}(k_x)$	1-D wavenumber spectrum of the wall-normal velocity [m^3/s^2]
ED_u	Relative spectral energy deficit for the stremwise component [%]
ED_v	Relative spectral energy deficit for the wall-normal component [%]
F_h	Free-water surface fluctuations [m]
Fr	Froude number [-]
F_U	Longitudinal depth and time-averaged velocity fluctuations [m/s]
$\overline{F_h F_U}$	Covariance between F_h and F_U [m/s]
f	Frequency [Hz]
f_s	Sampling frequency [Hz]
f_w	Wave frequency [Hz]
g	Gravitational acceleration [m/s^2]
H	Wave height [m]
H_i	Wave heigh of the incoming wave [m]
H_r	Wave heigh of the reflected wave [m]

H_{sd}	Wave heigh standard deviation [m]
$\overline{H}$	Mean wave height [m]
h	Flow depth [m]
h_0	Outer length-scale for wave plus current flows [m]
K_r	Reflection coefficient [-]
K_u	Kurtosis of the streamwise velocity component [-]
K_v	Kurtosis of the wall-normal velocity component [-]
k	Wave number [1/m]
k_s	Nikuradse equivalent sand roughness [m]
k_x	Streamwise wavenumber [1/m]
k_s^+	Roughness Reynolds number [-]
L	Wave length [L]
l	Characteristic length of the LDA measurement volume [m]
l_η	LDA measurement resolution [-]
l_S	Stokes length [m]
l^+	Viscous-scaled LDA measurement length [-]
N	Sample size [-]
p	Probability distribution [-]
Q	Flow rate (or discharge) [m^3/s]
$\overline{Q}$	Time-averaged flow rate (or discharge) [m^3/s]
R	Pipe radius [m]
R_h	Hydraulic radius [m]
RE	Wave Reynolds number [-]

Re_b	Bulk Reynolds number [-]
Re_τ	von Kármán number [-]
S_0	Bottom slope [-]
S_f	Energy-grade-line slope [-]
S_u	Skewness of the streamwise velocity component [-]
S_v	Skewness of the wall-normal velocity component [-]
S_w	Free-water surface slope [-]
s	Longitudinal spatial coordinate [m]
T	Wave period [s]
T_{sd}	Wave period standard deviation [s]
$\overline{T}$	Mean wave period [s]
t	Time [s]
U	Time-averaged streamwise velocity [m/s]
U_b	Bulk velocity [m/s]
U_c	Convection velocity [m/s]
U_e	Edge velocity [m/s]
U_{max}	Maximum velocity [m/s]
U_R	Ursell number [-]
U_S	Stokes drift velocity [m/s]
U_w	Longitudinal wave orbital velocity [m/s]
U^+	Mean streamwise velocity normalized by the shear velocity [-]
u	Streamwise component of the instantaneous velocity field [m/s]
u_τ	Shear (or friction) velocity [m/s]

u_{τ_c}	Shear (or friction) velocity for the current [m/s]
$u_{\tau_{wc}}$	Shear (or friction) velocity for the waves plus current [m/s]
$\tilde{u}$	Periodic component of the streamwise velocity [m/s]
u'	Fluctuating component of the streamwise velocity [m/s]
$\langle u \rangle$	Phase-averaged of the streamwise velocity [m/s]
$-\overline{uv}$	Shear stress for the waves plus current signal [m^2/s^2]
$-\overline{\tilde{u}\tilde{v}}$	Shear stress for the wave component [m^2/s^2]
$-\overline{u'v'}$	Reynolds shear stress [m^2/s^2]
$\overline{u'v'}_{Q1}$	Contribution of the first quadrant (outward interaction) [m^2/s^2]
$\overline{u'v'}_{Q2}$	Contribution of the second quadrant (ejection) [m^2/s^2]
$\overline{u'v'}_{Q3}$	Contribution of the third quadrant (inward interaction) [m^2/s^2]
$\overline{u'v'}_{Q4}$	Contribution of the four quadrant (sweep) [m^2/s^2]
V	Time-averaged wall-normal velocity [m/s]
v	Wall-normal component of the instantaneous velocity field [m/s]
v'	Fluctuating component of the wall-normal velocity [m/s]
W	Channel width [m]
w	Spanwise component of the instantaneous velocity field [m/s]
x	Longitudinal coordinate [m]
y	Vertical coordinate [m]
y^+	Wall units [-]
z	Spanwise coordinate [m]

Chapter 1

Introduction

1.1 Overview and background

Turbulent open-channel flows are ubiquitous in natural and anthropised environments. Classical examples include rivers, irrigation canals, waterways, tidal channels and marine currents. With respect to other, more canonical, wall-bounded flows (i.e. flat-plate boundary layers, pipe and closed-channel flows), they are characterised by particular properties that make their study a fascinating subject. These include (Cameron et al., 2017; Duan et al., 2020; Shen et al., 1999): (i) the presence of the free air-liquid surface that acts as a mobile boundary and significantly affects the underlying turbulence; (ii) the corners, located at the intersections between the bed, the side-walls and the free-surface, generate turbulence anisotropy inducing cellular secondary currents (i.e. persistent vortices in the streamwise direction) whose effects on turbulence seem to be non-negligible even for very wide channels; (iii) the boundary layer thickness is delimited by the free-surface; (iv) the frequent presence of a movable bed that leads to bedforms and suspended load; (v) the presence of gravity waves in tidal, coastal or estuarine contexts. In addition, natural rivers have bends or compound cross-sections, leading to the formation of other kinds of secondary flows (Van Balen et al., 2009) or macrovortices (Proust and Nikora, 2020; Soldini et al., 2004; Stocchino and Brocchini, 2010; Stocchino et al., 2011) that further influence the flow.

Due to its unique features and its importance in engineering, industrial and ecological applications, the study of turbulence in open-channel flows has attracted remarkable attention from the scientific community. Some examples of problems where a deeper understanding of turbulence in open-channel flows is fundamental are: the transport and mixing processes (e.g., sediments, nutrients, chemicals, seeds, and pollutants, Grant et al., 2018; Jirka et al., 2010; Moog and Jirka, 1999; Pähtz et al., 2020), quantifying fish swimming performance and schooling dynamics (Piper et al., 2015; Trinci et al., 2017), the design of hydraulic structures (such as fishways, spillways or hydro-kinetic turbines, Chamorro et al., 2013; Dargahi, 2006; Quaranta et al., 2017), the mechanisms of local scouring (Coscarella et al., 2020; Dargahi, 1990), the riparian vegetation restoration and management (Errico et al., 2018, 2019), the vegetation-flow-sediment interactions (Calvani et al., 2019; Caroppi et al., 2019; Nepf, 2012; Vettori and Nikora, 2019), and the wave-current interaction (Kemp and Simons, 1982, 1983; Klopman, 1994; Musumeci et al., 2006; Umeyama, 2005). Turbulence properties of open-channel flows have been investigated by varying extensively the bed-surface characteristics (smooth, rough, movable, porous and relative submergence, Dey et al., 2011; Manes et al., 2007, 2011; Nezu and Nakagawa, 1993; Nikora and Goring, 2000b), the flow uniformity (accelerating and decelerating flows, Auel et al., 2014; Cardoso et al., 1991; Kironoto and Graf, 1995; Onitsuka et al., 2009; Pu et al., 2018; Song and Chiew, 2001), the Froude number (Auel et al., 2014; Tominaga and Nezu, 1992; Xinyu et al., 1995) and the Reynolds number (Kirkgöz, 1989; Nezu and Nakagawa, 1993; Poggi et al., 2002; Roussinova et al., 2008). Besides, growing attention has been paid to the structure of turbulence, which is characterised by vortices, coherent structures and other cyclical events with different length and time scales (Bagherimiyab and Lemmin, 2018; Jackson, 1976; Nakagawa and Nezu, 1981; Roy et al., 2004; Shvidchenko and Pender, 2001; Sukhodolov et al., 2011; Tamburrino and Gulliver, 1999; Zhong et al., 2015).

Roughly speaking, coherent structures are regions of the flow characterised by a detectable spatial and temporal organization compared to the surrounding random flow field. Coherent structures can be envisaged as the skeleton of wall turbulence and they contribute significantly to dictate turbulent kinetic energy levels and transport phenomena (Hussain, 1986; Jiménez, 2018; Porporato and Ridolfi, 2002; Robinson, 1991). In open-channel flows (Fig. 1.1), the study of

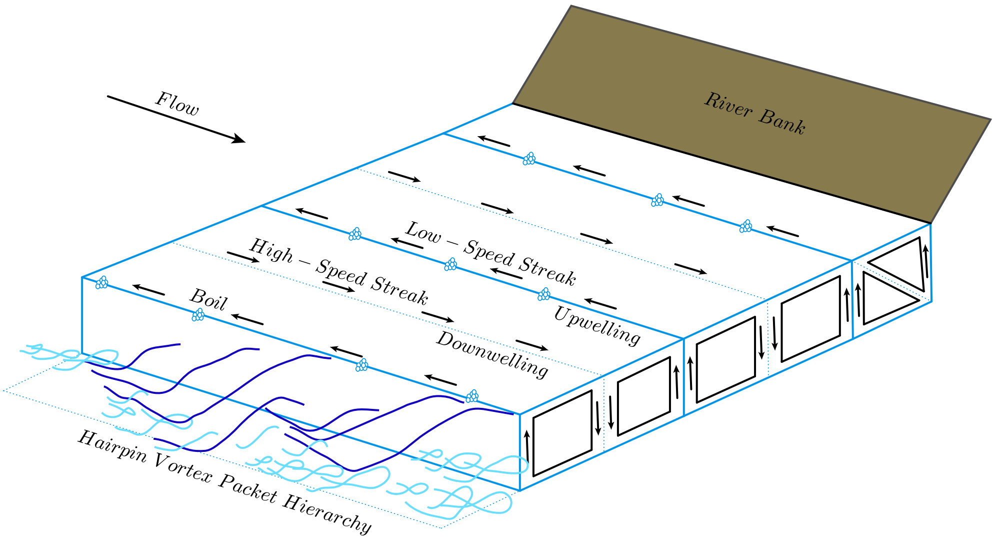

Fig. 1.1 Coherent structures in open-channel flows and associated phenomena (adapted from Adrian and Marusic, 2012). The filaments in cyan and blue indicate large-scale structures.

coherent structures is complicated by the presence of cellular secondary currents (counter-rotating cells with vertical and spanwise dimensions approximately equal to the water depth, Nezu and Nakagawa, 1993), that strongly interact with the main flow and turbulence phenomena. Moreover, in coastal, estuarine and lagoon environments, also gravity waves exacerbate the complexity of turbulence by introducing additional characteristic length-scales in the flow (i.e. surface wave amplitude, surface wave length and orbital motion).

This Dissertation intends to contribute to the ongoing research efforts by addressing the scaling of turbulence in open-channel flows with and without the presence of gravity waves. In particular, this work can be essentially divided into two distinct contributions. The first addresses turbulence in smooth-bed open-channel flows with the main aim of investigating the scaling of large-scale structures usually referred to as Large- and Very-Large-Scale Motions (LSMs and VLSMs). The second part addresses, more in general, the scaling of turbulence in open-channel flows perturbed by collinear gravity waves.

With respect to the first part, LSMs and VLSMs have been revealed experimentally through observation of persistent statistical coherence in the streamwise velocity, where two prevalent length-scales emerge. The importance of LSMs and VLSMs lies on the large amount of turbulent kinetic energy and momentum that they transport across the flow. In canonical wall-flows different aspects of LSMs and VLSMs have been studied (e.g. scaling, origin, evolution, interaction with other length-scales) and it has been found that LSMs extend up to $2-3\delta$ in the longitudinal direction while VLSMs can exceed 20δ, where δ is the appropriate outer length-scale - i.e. the boundary layer thickness, the half-channel height or the pipe radius (Balakumar and Adrian, 2007; Guala et al., 2006; Hutchins and Marusic, 2007a,b; Kim and Adrian, 1999). Conversely, in open-channel flows a clear picture of LSMs and VLSMs is still lacking, even though some studies in this direction have been recently undertaken (Cameron et al., 2017; Duan et al., 2020; Zampiron et al., 2020). In earlier works, the presence of long turbulent structures has been recognised multiple times in open-channel flows and linkages with river morphodynamics have been proposed. For instance, Shvidchenko and Pender (2001) suggested that the formation of longitudinal ridge and trough patterns in erodible channels is associated with the presence of turbulent structures extending around ten flow depths and taking the form of high-speed and low-speed wedges. Further, da Silva and Yalin (2017) speculated that coherent structures with longitudinal and spanwise vorticity trigger the formation of dunes and alternate bars, respectively. It was also discovered that LSMs and VLSMs in open-channel flows have many practical implications related with the modulation of pressure fluctuations or the entrainment of sediment particles (Cameron et al., 2019, 2020), the performance of hydro-kinetic turbines (Chamorro et al., 2015), and hydraulic resistance (Zampiron et al., 2020).

With respect to the second part, the scaling of turbulence properties in coexisting open-channel flows with waves has never been accurately addressed. This stems from the fact that research so far has been mainly devoted to studying the bulk properties of the flow (i.e. mean velocity, bottom shear stress and wave alterations in the presence of currents, Soulsby et al., 1993). Therefore, in the relevant literature the results of turbulence velocity statistics are almost always presented in dimensional form (Fredsøe et al., 1999; Kemp and Simons, 1982, 1983; Klopman, 1994; Umeyama, 2005; van Hoften and Karaki, 1977) and nobody really knows the fate of large-scale structures such as LSMs and VLSMs. Perhaps, one difficulty underlying these topics that has hindered the development of a more solid understanding is the signal decomposition. Indeed, a common methodology that can be applied to extract the turbulence signal from velocity measurements regardless of the environment in which data are collected (i.e. laboratory or field), and so that results of different studies can be compared, does not exist.

1.2 Aims and objectives

In order to contribute to bridge these knowledge gaps, this Dissertation presents results from an extensive experimental campaign carried out in a large-scale laboratory flume facility, which allows for the generation of both open-channel flows and gravity waves. Longitudinal and vertical velocity components were accurately measured by means of a 2-D Laser Doppler Anemometer (LDA) at high sampling frequencies. Alongside the velocity measurements, also the water surface level, the flow rate and the water temperature were continuously measured. Experimental data were gathered and analysed to pursue the following objectives:

1) to identify the presence of LSMs and VLSMs in smooth-bed open-channel flows, highlighting the differences compared to canonical wall-flows;

2) to study the progressive alteration of LSMs and VLSMs induced by the presence of the side walls, including a comprehensive scaling picture that considers open-channel flows with different aspect ratios;

3) to assess the effect of gravity waves on turbulence in open-channel flows depending on wave frequencies and amplitudes, with a special focus on:

    3.1) the scaling of first and second-order velocity statistics;

    3.2) the fate of LSMs and VLSMs.

1.3 Dissertation outline

The Dissertation is organised in four Chapters. Chapters 2 and 3 are structured as stand-alone (i.e. paper-like), with dedicated Introduction reporting the relevant literature review, Methodology, Results, and Conclusions. Chapter 2 deals with the measurement of LSMs and VLSMs in turbulent smooth-bed open-channel flows and the effects of cellular secondary currents. The methodological Section 2.2 contains details of the flume facility, instrumentation and experimental setup that were used to acquire data for both Chapters 2 and 3. Chapters 3 describes the effects of gravity waves on a turbulent smooth-bed open-channel flow by analysing the modification of turbulent intensities, Reynolds stresses and energy distribution across frequencies. In Chapter 4 the main findings are summarised together with suggestions for future research on this topic.

1.4 Novel contributions and publications

The following publication in international journals were extracted from this Dissertation:

- **C. Peruzzi**, D. Poggi, L. Ridolfi, C. Manes. On the Scaling of Large-Scale Structures in Smooth-Bed Turbulent Open-Channel Flows, *Journal of Fluid Mechanics*, Vol. 889, A1, 2020.
https://doi.org/10.1017/jfm.2020.73

Moreover, some parts of this work have been/will be presented (as poster or oral presentation) at the following events:

- *XXXVII Convegno Nazionale di Idraulica e Costruzioni Idrauliche (IDRA)*, Reggio Calabria, Italy, September 2020.
- *6th International Association for Hydro-Environment Engineering and Research (IAHR) European Congress*, Warsaw, Poland, September 2020.
- *European Geosciences Union (EGU) General Assembly*, Vienna, Austria, April 2019.
- *Phd Days del Gruppo Italiano di Idraulica (GII)*, Catania, Italy, June 2018. (Award for the Best Presented Poster)
- *Phd Days del Gruppo Italiano di Idraulica (GII)*, Torino, Italy, June 2017.

Chapter 2

Turbulence properties in open-channel flows over smooth-bed: velocity statistics and spectral analysis

Part of this Chapter forms the scientific publication Peruzzi et al. (2020).

This Chapter presents some experimental results to describe turbulence properties of smooth-bed open-channel flows and focuses, in particular, on the scaling of large scale turbulence structures, normally referred to as Large-Scale-Motions (LSMs) and Very-Large-Scale-Motions (VLSMs). Longitudinal and bed normal velocities were measured at high sampling frequency by means of a Laser Doppler Anemometry system, in non-uniform (but fairly in equilibrium) open-channel flows developing in a recirculating laboratory flume. Pre-multiplied spectra of the longitudinal velocity fluctuations revealed the existence of two peaks occurring at wavelengths consistent with those associated with LSMs and VLSMs as detected in the past literature pertaining to wall turbulence. However, contrary to the so-called canonical wall-flows (i.e. flat plate boundary layers, pipe and closed-channel flows), LSM and VLSM-peaks, that were observed in the open-channel flows investigated herein, are detectable over a much larger extent of the wall-normal coordinate. Furthermore, the VLSM-peak appears at von Kármán numbers Re_τ[1] as low as 725, whereas in other wall-flows much higher values are normally required. Finally, as conjectured by a recent study on uniform rough-bed open-channel flows (Cameron et al., 2017), the present paper confirms that LSM-wavelengths scale nicely with the flow depth, whereas the channel aspect ratio (i.e. the ratio between channel width and flow depth) is the non-dimensional parameter controlling the scaling of VLSMs-wavelengths. The intensity and wavelengths of the VLSM-peaks were also observed to depend on the spanwise coordinate. This result suggests that VLSMs might be dynamically linked to secondary currents as these are known to vary in strength and size across the channel width.

2.1 Introduction

In wall-flows, the study of large-scale coherent structures has received particular attention because such structures carry a large portion of the Turbulent Kinetic Energy (TKE) and contribute significantly to the transport of momentum and relevant scalars such as heat, oxygen and pollutants (Jiménez, 2018; Marusic et al., 2010; Robinson, 1991). There is now compelling evidence that, in canonical smooth-wall flows - which include (flat-plate) turbulent boundary layers, closed-channel and pipe flows - two distinct large-scale structures occur. They are commonly referred to as Large-Scale Motions (LSM) and Very-Large-Scale Motions (VLSM). Although there are several methods to visualise and identify such structures, the most employed diagnostic tool is based on pre-multiplied one-dimensional spectra, where LSMs and VLSMs impose two well-defined peaks (Hutchins and Marusic, 2007b; Kim and Adrian, 1999). Many studies have proven that such peaks occur at wavenumbers which scale with the characteristic outer length-scale of the flow δ (Adrian et al., 2000; Balakumar and Adrian, 2007; de Silva et al., 2018; del Álamo and Jiménez, 2003; Ganapathisubramani et al., 2003; Guala et al., 2006; Hutchins and Marusic, 2007a,b; Hutchins et al., 2005; Kim and Adrian, 1999; Monty et al., 2007, 2009; Sillero et al., 2014; Tomkins and Adrian, 2003).

---

[1] The von Kármán number is defined as $Re_\tau = u_\tau\delta/\nu = \delta/\delta_\nu$, where δ and δ_ν are the characteristic outer length-scale (equal to the flow depth h in open-channel flows) and the viscous length-scale of the flow, respectively. In hydrodynamically-smooth flows, this number quantifies the inner-outer length scale separation.

However, Hutchins and Marusic (2007b) recommend that the von Kármán number $Re_\tau = \delta u_\tau / \nu$ (where u_τ is the shear velocity and ν is the kinematic viscosity) of the flow should not be less than 1700 in order to obtain a clear distinction between the two aforementioned peaks. This value is just a reference that ensures one order of magnitude of length-scale separation between LSMs and VLSMs in turbulent boundary layers. When this condition is satisfied, Hutchins and Marusic (2007a,b) showed that the wavenumbers associated with LSM and VLSM peaks correspond to structures whose longitudinal size is $2-3\delta$ and 6δ, respectively. It was also observed that LSM-peaks persist throughout most of the outer layer while VLSM-peaks vanish above the logarithmic region.

As far as pipe and channel flows are concerned, the picture is significantly different from boundary layers because spectral peaks corresponding to VLSMs are detectable well within the outer layer (Monty et al., 2007, 2009; Sillero et al., 2014) and correspond to scales up to 20δ. More similarly to turbulent boundary layers, LSM-peaks were observed to scale as 3δ and to persist up to the channel/pipe centreline (see also Balakumar and Adrian, 2007; Guala et al., 2006; Kim and Adrian, 1999; McKeon and Morrison, 2007).

About the generation mechanism of LSMs and VLSMs, the literature proposes two potential explanations associated with two approaches. There is a so-called "parent-offspring" approach whereby LSMs are considered to emerge out of the alignment of several hairpin-vortices forming a packet and VLSMs, in turn, as groups of aligned LSM packets (Adrian, 2007; Adrian and Marusic, 2012; Hommema and Adrian, 2002; Katul, 2019). The second approach, instead, claims that VLSMs and LSMs are a direct consequence of a mean-flow instability process and their existence is independent of the dynamics of smaller-scale structures, such as hairpin vortices, which, in the first approach, are instead considered as the building-block of wall-turbulence (Hwang and Cossu, 2010). In the second approach VLSMs are interpreted to be the principal actors of a self-sustaining "outer-layer" cycle, given their streaky and meandering nature and their marked longitudinal vorticity. The "outer-layer" cycle shares analogies with its better understood near-wall (i.e. in the buffer layer) counterpart, and VLSMs play the same role as the so-called elongated streamwise vortices (Cossu and Hwang, 2017; Hwang and Bengana, 2016; Hwang et al., 2016; Rawat et al., 2015).

Large-scale coherent structures have been extensively studied also in open-channel flows, which are the subject of the present study, as they influence ecologically-relevant scalar transport processes (such as oxygen, nutrients and sediments), river morphodynamics and even the power output of hydro-kinetic marine turbines (Cameron et al., 2019, 2020; Chamorro et al., 2013; Jirka et al., 2010; Moog and Jirka, 1999; Nepf, 2012; Trinci et al., 2017; Venditti et al., 2013). Laboratory and field experiments have detected the presence of large-scale wedge-type structures, whose sizes in the streamwise, spanwise and wall-normal direction is expressed as a function of the outer-scale, namely, the water depth h (Bagherimiyab and Lemmin, 2018; Cellino and Lemmin, 2004; da Silva and Yalin, 2017; Franca and Lemmin, 2015; Ghesemi et al., 2019; Hurther et al., 2007; Jackson, 1976; Nakagawa and Nezu, 1981; Nezu and Nakagawa, 1993; Rashidi, 1997; Rashidi and Banerjee, 1988; Roy et al., 2004; Shen and Lemmin, 1999; Shvidchenko and Pender, 2001; Tamburrino and Gulliver, 1999; Zhong et al., 2016).

Some studies indicate the presence of long structures with streamwise vorticity, which resemble the VLSMs as defined in canonical flows (Grinvald and Nikora, 1988; Nezu, 2005; Sukhodolov et al., 2011; Zhong et al., 2015). Nevertheless, Cameron et al. (2017) were the first to provide insights into the occurrence and scaling of VLSMs in turbulent open-channel flows. In this study, the authors present long-duration Particle Image Velocimetry (PIV) measurements in fully-rough open-channel flows over a bed made of spheres packed in a hexagonal arrangement. Among the numerous results, they report pre-multiplied spectra of the longitudinal velocity component, which display the characteristic double-peak behaviour observed for canonical wall-flows. They also report that one of the peaks occurs at wavelengths of about $6-7h$ and nicely scales with the water depth. This peak is associated with the presence of LSMs. The other peak occurrs at wavelengths consistent with those pertaining to VLSMs, but not scaling with the flow depth. Moreover, such wavelengths are recorded to be up to 50 times the water depth h. If h is taken as the representative outer length-scale (as it is normally assumed), this means that the non-dimensional length of VLSMs in open-channels flows (as detected from pre-multiplied spectral peaks) is much greater than in other canonical wall-flows. Due to the mismatch between the VLSM and LSM scaling, the authors concluded that, in open-channel flows, these two types of structures might be generated by independent and, possibly, different mechanisms.

Unfortunately, due to the fact that the experiments were performed in rough-wall conditions, Cameron et al. (2017) could not unambiguously identify the non-dimensional parameter controlling the scaling of VLSMs among the following: the aspect ratio W/h, the relative submergence h/D and the von Kármán number Re_τ (where W is the channel width and D is the spheres' diameter). The number of factors further increased when, in a subsequent study, the same authors (Cameron et al., 2018) noticed that VLSMs wavelengths were also dependent on the non-dimensional distance from the flume inlet x/h. Despite the large number of parameters involved, Cameron et al. (2017) argued that the aspect ratio W/h was the most plausible "culprit" for the variation of depth-normalised VLSM wavelengths. The authors justify this hypothesis on the basis that VLSMs and W are of the same order of magnitude and hence W might constrain VLSMs' growth.

The main aim of the present Chapter is to further explore the scaling of LSMs and VLSMs in open-channel flows. Towards this end, the results from a series of smooth-bed experiments are presented, as they are free from complicating factors associated with rough-beds. In fact, in smooth-bed open-channel flows, the number of non-dimensional parameters that may influence the scaling of large-scale structures reduce from four to three, namely:

$$Re_\tau \qquad W/h \qquad x/h \tag{2.1}$$

It should be emphasized that the experiments reported herein were carried out in non-uniform flow conditions, which can represent a potential complicating factor. As extensively discussed in Section 2.3, though, non-uniformity levels were kept mild and constrained within a limited range. Besides guaranteeing for self-similar flow conditions to be established, this allowed for a comparative analysis between different tests, where the effects of Re_τ, W/h and x/h on velocity statistics (with a specific focus on velocity spectra) could be reasonably isolated and explored.

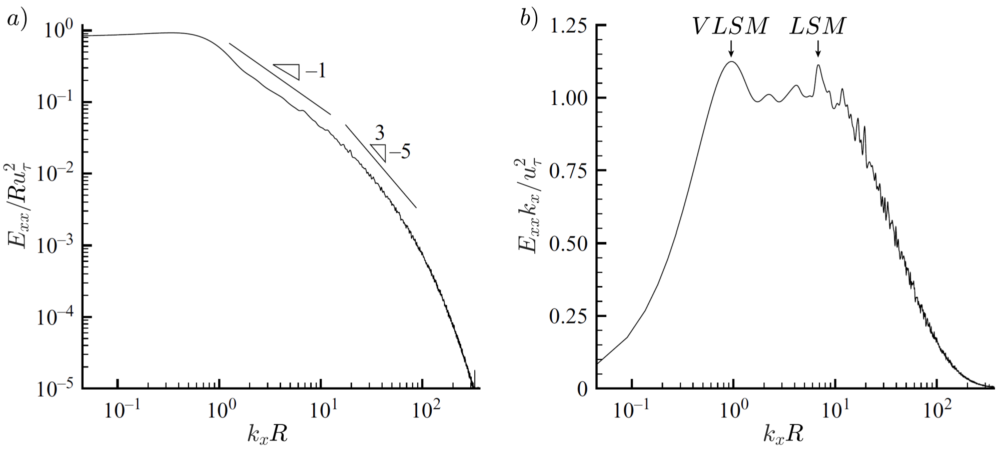

Fig. 2.1 Outer-scaled (a) spectrum and (b) pre-multiplied spectrum of the streamwise velocity fluctuation in a turbulent pipe flow ($y/R = 0.084$ and $Re_\tau \approx 2000$, where R is the pipe radius). In pannel (a) also the Townsend −1 and Kolmogorov −5/3 spectrum scalings are reported for comparison, while in pannel (b) the LSM and VLSM spectral peaks are hilighted. Figure adapted from Guala et al. (2006).

2.1.1 Large- and Very-Large-Scale Motions in canonical wall-bounded flows: a brief review

Until the end of the last century, the importance of large-scale structures in wall-bounded flows has often been overlooked because being in force Townsend's idea of 'inactive' large-scale motions (Townsend, 1976), i.e. turbulent structures longer than $\approx \delta$ give a negligible contribution to the Reynolds stress. This idea was difficult to scrutinise for difficulties encountered at that time in the study of large-scale structures both in computational and experimental studies. The seminal works of Kim and Adrian (1999) and Guala et al. (2006) have rekindled the interest in the study of LSMs and VLSMs owing the compelling evidence of the large amount of kinetic energy and Reynolds stress that they carry. The primary tool for the identification and analysis of LSMs and VLSMs was the pre-multiplied spectrum of puntual long-lasting velocity time-series as shown in the example shown in Fig. 2.1(b). In a pre-multiplied spectrum, equal areas under the curve have equal energies and a bi-modal distribution can be glimpsed. The occurrence of the maxima in the bi-modal distribution identifies the VLSMs and LSMs presence (Kim and Adrian, 1999). Guala et al. (2006) quantified that, irrespectively of the Reynolds number, more than 35%

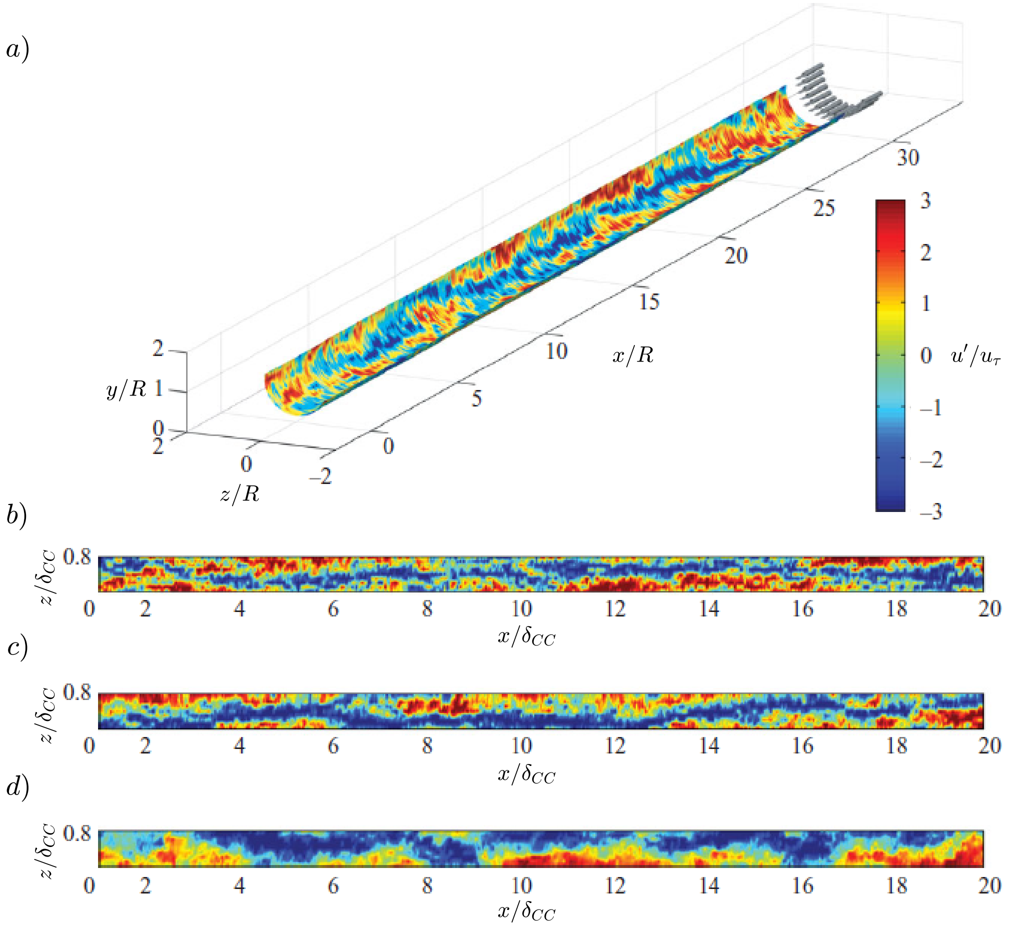

Fig. 2.2 Countour plots of streamwise velocity fluctuations u' (a) in a turbulent pipe flow (y/R = 0.15 and Re_τ = 3472) and (b)−(d) in a turbulent closed-channel flow (y/δ_{CC} = 0.08, y/δ_{CC} = 0.14 and y/δ_{CC} = 0.56, respectively, and Re_τ = 3178, where δ_{CC} is the half-channel height). The measurement were carried out by using a rake of hot-wire probes (15 for the pipe and 10 for the closed-channel). Figure adapted from Monty et al. (2007).

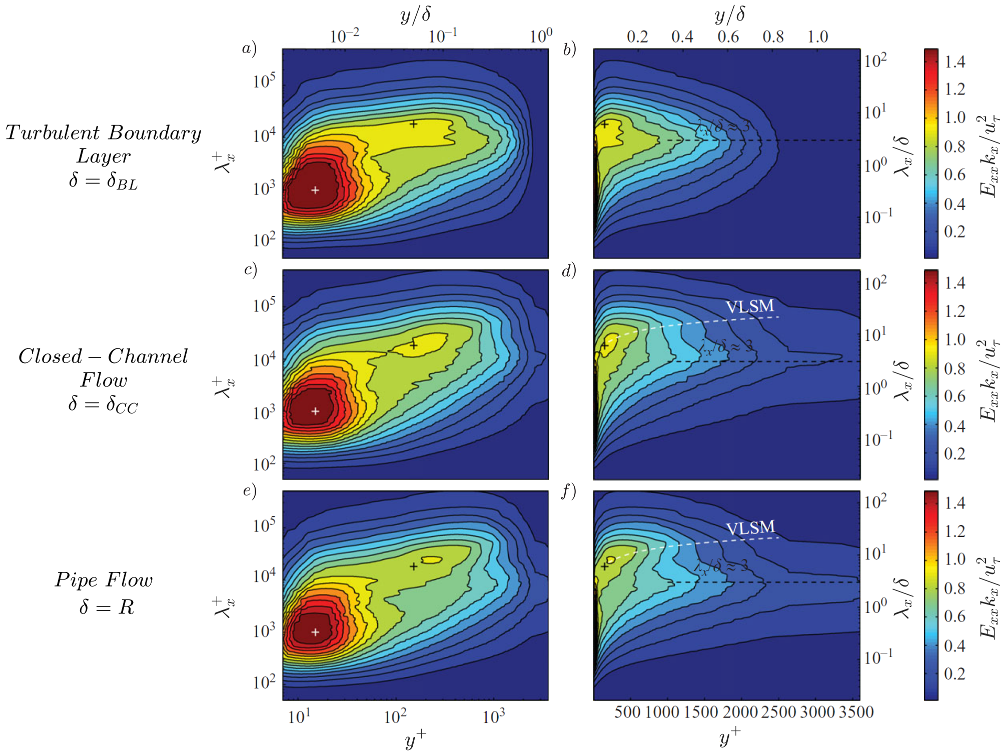

Fig. 2.3 Contour maps of the pre-multiplied 1-D spectra of the stremwise velocity fluctuation as a function of streamwise wavelength λ_x and the distance from the wall y for (a)–(b) a turbulent boundary layer, (c)–(d) a closed-channel flow, and (e)–(f) a pipe flow. The Re_τ is around 3000 for each case. The pannels at the left-and side have a logaritmic x-axix, while the pannels at the rigth-hand side have a linear x-axix. Figure adapted from Monty et al. (2009).

of the turbulent kinetic energy and more than 50% of the Reynolds shear stress are to attribute to VLSMs.

From a morphological point of view, LSMs and VLSMs are highly elongated regions of uniform streamwise momentum. Particle Image Velocimentry (PIV) measurements strongly aid in the visualisation of LSMs and VLSMs in the log layer (Ganapathisubramani et al., 2003; Hutchins et al., 2005; Tomkins and Adrian, 2003), showing regions of low- and hight-speed fluid with a spanwise extension of $0.3{-}0.5\delta$. However, the longitudinal length of these structures usually exceed the ordinary PIV field-of-view and so a more general picture was obtained using rake of hot-wire probes (Hutchins and Marusic, 2007a; Monty et al., 2007). Fig. 2.2(a–d) reports examples of hot-wire rake measurements in pipe and closed-channel flows, where the longitudinal extent of VLSMs can be clearly seen. It can be noted that these structures have a meandering configuration while the width is visibly increasing with distance from the wall (Fig. 2.2b–d). Hutchins and Marusic (2007a) obtained similar results for turbulent boundary layers. The typical meandering configuration of these structures suggests that the VLSM length detected from single-point statistics could be smaller with respect to the real one since the meandering tendency masks it (i.e. the one-point measurements reveal the meander wavelength instead of the VLSM wavelength). Furthermore, Kevin et al. (2019) found that the VLSM meandering signature increase with the distance from the wall.

Nevertheless the similar morphology of VLSMs in canonical wall-flows, there are some quantitative differences between internal flows (closed-channel and pipe) and external flows (boundary layers), as clearly visible from Fig. 2.3(a–f). In particular, VLSMs footprint vanishes beyond $y/\delta \approx 0.25$ in turbulent boundary layers (Fig. 2.3b), while the VLSMs presence is detectable up to $y/\delta \approx 0.6$ for pipe and closed-channel flows (Fig. 2.3d and Fig. 2.3e). Also the maximum VLSM wavelength differ, as $\lambda_x \approx 6\delta$ and $\lambda_x \approx 20\delta$ for internal and external flows, respectively. The situation is slightly different for the LSMs, where the maximum wavelength is the same in each case ($\lambda_x \approx 3\delta$), while their presence is detectable up to $y \approx \delta$ in internal flow, but only up to $y \approx 0.8\delta$ in external flows.

Interestingly, as reported in Fig. 2.4, a common features of LSMs and VLSMs in canonical wall-flows is that their wavelengths well collapse when scaled with the outer-length scale δ. The lower and upper curves reported in

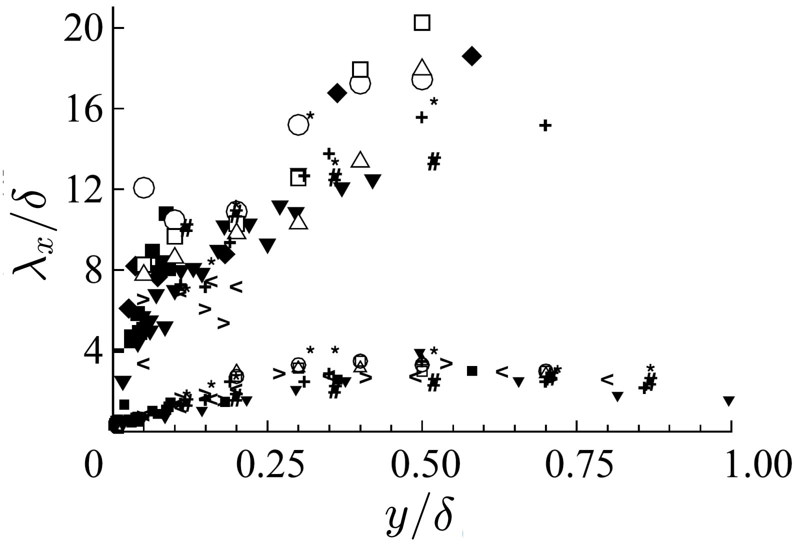

Fig. 2.4 Outer-scaled LSM and VLSM wavelegth peaks, where δ is the appropriate outer-length scale. Symbols are referred to turbulend boundary layer, closed-channel and pipe flow experiments, see Balakumar and Adrian (2007) for more detailed information.

Fig. 2.4 show the LSMs and VLSMs scaling, respectively, for experimental data taken from boundary layers, closed-channel and pipe flows.

2.2 Laboratory set-up and methodology

Experiments were carried out in a large-scale, non-tilting, recirculating, open-channel flume at the Giorgio Bidone Hydraulics Laboratory of the Politecnico di Torino. Fig. 2.5 gives an overview of the arrangement of the flume within the laboratory while Fig. 2.6a reports the technical drawing of the flume. The main part of the facility is composed of a rectangular channel, which is 50 m long, 0.61 m wide and 1 m deep. The flume has glass side-walls and a bed that is made mainly of steel and, in some parts, of glass.

The flume bottom needed to be raised in order to allow for near-wall LDA measurements, which were carried out following the technique proposed by Poggi et al. (2002) and described later. To this end, smooth concrete blocks (2 m long, 0.6 m wide and 0.1 m thick) were placed over the original bed of the flume along its entire length. The Nikuradse's equivalent sand roughness k_s for hand-

Fig. 2.5 Photo of the large-scale open-channel flume at the Giorgio Bidone Hydraulics Laboratory of the Politecnico di Torino (upstream-downstream view).

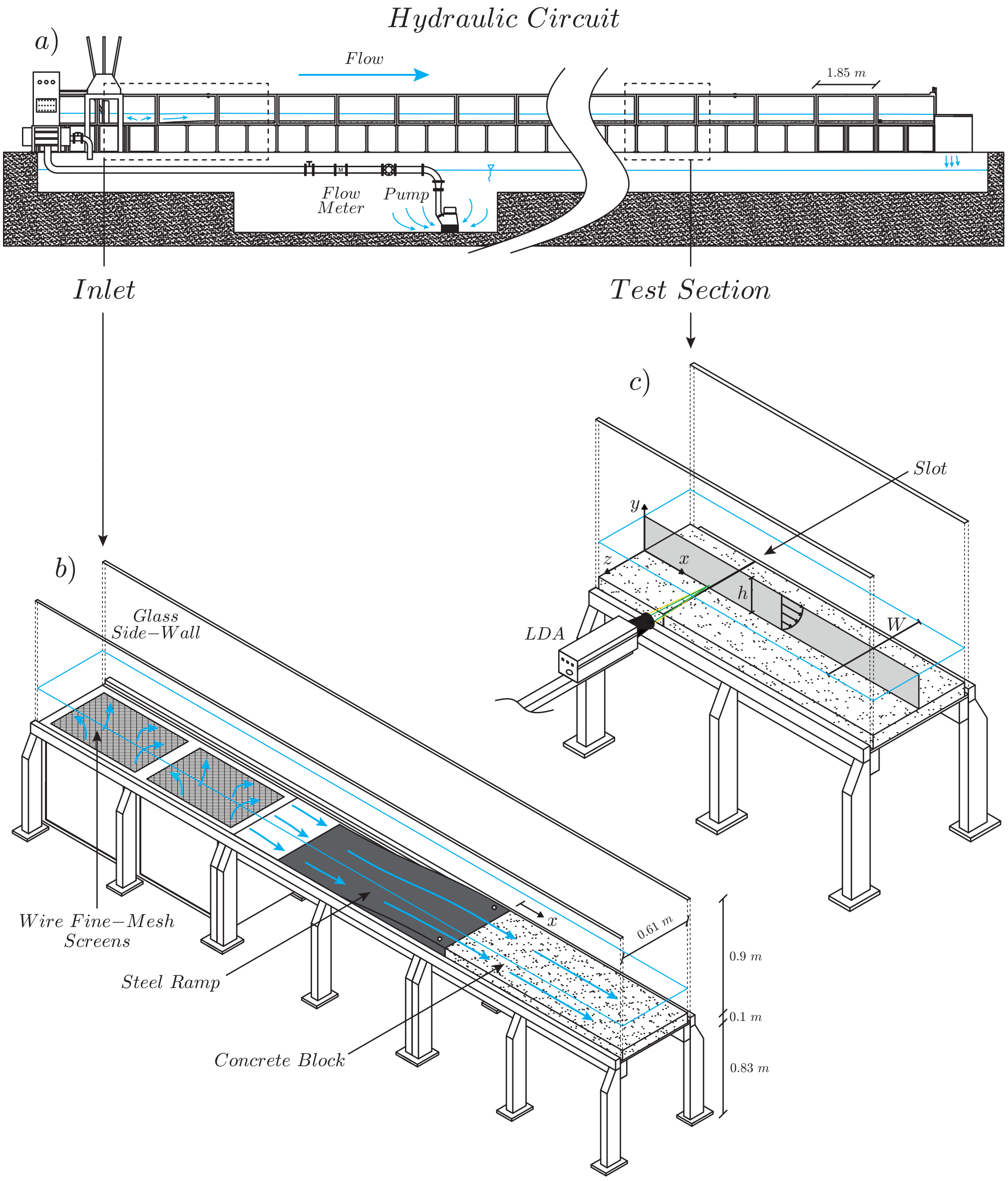

Fig. 2.6 Technical overview of the flume used for the experiments: (a) sketch of the whole hydraulic circuit; (b) and (c) details of the inlet flow conditions and the test section, respectively. Panel (c) also shows the system of coordinate axes chosen in the present study (i.e. the streamwise x, wall-normal y and spanwise z directions) and defines the flow depth h and the channel width W. Please note that the coordinate x has its origin at the downstream end of the ramp (see panel b).

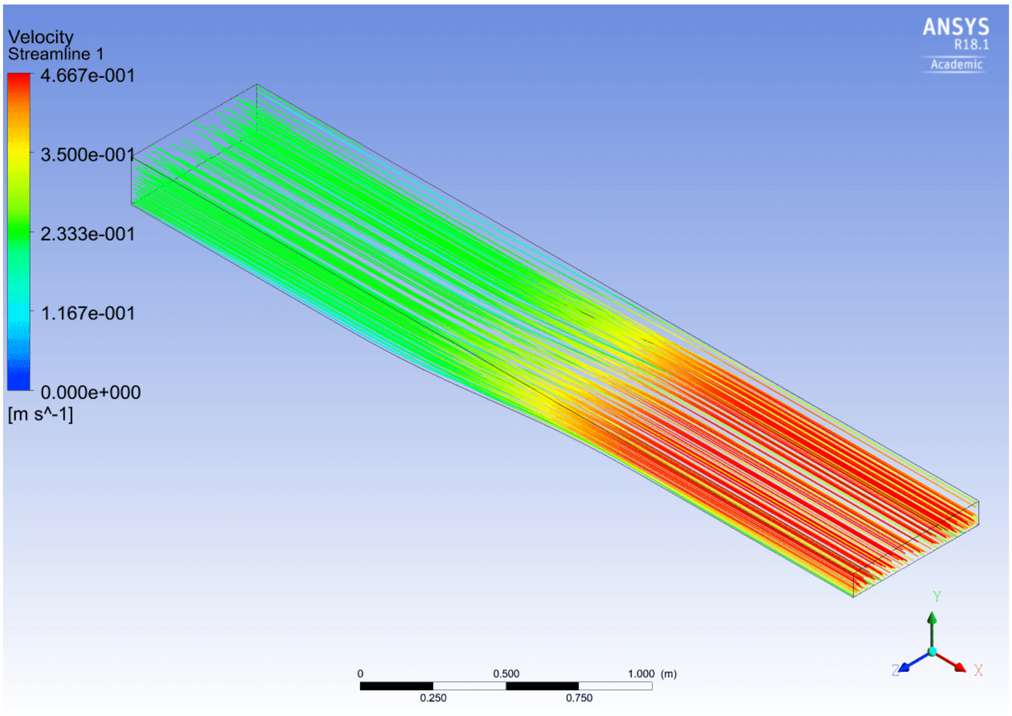

Fig. 2.7 Velocity streamlines pattern computed from a 3-D CFD simulation of the fifth-order polynomial-shaped ramp (top view, flow from left to right).

finished concrete without irregularities was estimated to be equal to 0.25 mm. This value corresponds to the mean value of those obtained by fitting the log law of the wall to experimental mean velocity data for each test, and it is coherent with literature data, as tabulated in Henderson (1966). Some considerations on the achievement of hydraulically smooth-bed conditions are reported in Section 2.3. In the proximity of the upstream-end of the flume, the original bed and the concrete blocks were gently connected by a stainless steel ramp (1.6 m long) designed to follow the shape of a fifth-degree polynomial (Bell and Mehta, 1988) to avoid boundary layer separation (Fig. 2.6b). Computational Fluid Dynamics (CFD) was employed to test the design of the ramp. A computational model of the ramp was implemented by using the commercial code ANSYS Fluent. Results in the form of streamlines, for an incoming turbulent flow with bulk velocity $U_b = 0.22$ m/s and flow depth $h = 0.2$ cm are reported in Fig. 2.7. The streamlines are coloured by the values of the flow velocity. The turbulence closure used for the simulation was the classical $k-\varepsilon$ scheme (Pope, 2000). It can be seen that the fifth-degree polynomial conformation guaranteed no flow separation as the streamlines closely follow the geometry of the contraction. In order to further reduce turbulence generated by the hydraulic circuit, a series of wire fine-mesh screens were placed in the sump underlying the flume inlet (Fig. 2.6b).

The water depth inside the flume was regulated by means of a vertical slot-weir placed at the downstream-end of the flume, which modifies the backwater profile of the flowing water. Five ultrasonic distance sensors (company Fae s.r.l., model FA 18-800/I-S) were arranged along the length of the flume in order to monitor the slope of the mean water depth (distances from the x origin: 3.1 m, 21.1 m, 27.1 m, 30.8 m and 39.8 m). Each probe emits an ultrasonic signal, which propagates with a divergence-angle of 8 degrees and is characterized by an optimal sensing distance ranging between 10−80 cm from the sensor. In this specific application, each probe was positioned at 80 cm from the concrete bottom, which means that free-surface fluctuations were measured over an area of 0.025 m^2 for a water depth of 20 cm and over an area of 0.039 m^2 for a water depth of 5 cm. The accuracy of the measured distance is ±1 mm, which results to be a constant value if the gauge works inside the optimal sensing distance[2].

A digital thermometer (precision of ±0.2 °C) was employed to monitor the temperature of the water and estimate its kinematic viscosity ν, for each experiment.

A submerged pump (company ITT Flygt AB, model BIBO 2151, impeller n° 231) enabled water recirculation between the channel and a large under-ground sump, which was connected to the inlet through a pipe with diameter 200 mm where an electromagnetic flow-meter (company Euromag International, model

---

[2] The uncertainty in the water surface slope determination can be estimated taking into account the error propagation, assuming that the measurement errors in the water levels are random and uncorrelated. Considering the quantity $\mathcal{Q}$ as the algebraic sum of the measured quantities $\mathcal{A}$ and $\mathcal{B}$ with uncertainty equal to $\delta\mathcal{A}$ and $\delta\mathcal{B}$, the measurement error $\delta\mathcal{Q}$ can be estimated as $\delta\mathcal{Q} = \sqrt{\left(\delta\mathcal{A}\right)^2 + \left(\delta\mathcal{B}\right)^2}$. Now, if the quantity $\mathcal{Q}$ is given by the multiplication or division of the measured quantities $\mathcal{A}$ and $\mathcal{B}$, the measurement error is $\delta\mathcal{Q} = |\mathcal{Q}|\sqrt{\left(\delta\mathcal{A}/\mathcal{A}\right)^2 + \left(\delta\mathcal{B}/\mathcal{B}\right)^2}$. Since the water surface slope is defined as $S_w = \mathrm{d}h/\mathrm{d}x = (h_i - h_j)/L_{ij}$ (where h_i and h_j are the water levels recorded at the ultrasonic gauges i and j, respectively, and L_{ij} is the distance between them), a combination of the aforementioned expressions gives the measurement error for S_w. For instance, considering the water levels recorded for the test 3 (see Tab. 2.3) at the third and fourth gauges (27.1 m and 30.8 m from the x origin) with the random error equal to ±1 mm and assuming a random error of ±1 cm in the L_{ij} length, $S_w = 8.15 \cdot 10^{-5} \pm 0.15 \cdot 10^{-5}$.

MC 608A 6-3) was mounted to monitor the flow rate for each experimental test (Fig. 2.6a).

As already mentioned, near-wall LDA measurements were made possible by adopting the technique developed and extensively tested by Poggi et al. (2002) and subsequently utilised in many other studies (Escudier et al., 2009; Manes et al., 2011; Poggi et al., 2003, 2007). This technique is very simple but effective. It involves the making of a thin vertical slot in the bed that allows for the passage of the vertical LDA laser-beams (Fig. 2.6c). To this end, in the proximity of the test section, the vertical slot was created simply by leaving a 3 mm gap between two adjacent concrete blocks. The lower part of the gap was filled by consolidated sand and blocked using Teflon tape (see Fig. 2.8 for details). The measurement point was slightly shifted beyond the end of the slot towards the middle of the flume. The slot created in this way proved to be effective for the undisturbed propagation of the vertical laser-beams while avoiding measurable alterations of near-wall turbulence properties (see Section 2.5.1, which shows how the first, second and higher order velocity-statistics collapse fairly well into canonical curves). It is also important to highlight that the main aim of the present Dissertation is to study large-scale structures for $y/h \geq 0.1$, since the Taylor frozen-turbulence hypothesis adoption leads to significant distortions in the results coming from spectral analysis in the near-wall region (Nikora and Goring, 2000a).

The instantaneous velocity fluctuations were measured by means of a 2-D LDA working in back-scatter configuration. The LDA system is a Dantec Dynamics Flow Explorer DPSS working with two pairs of laser beams having a wavelength of 532 nm (green) for the longitudinal component u and 561 nm (yellow) for the wall-normal component v. The intersection between these four beams creates two ellipsoidal volumes of $2.96 \cdot 10^{-3}$ mm^3 (ellipsoidal axes: $d_x = 0.083$ mm, $d_y = 0.082$ mm and $d_z = 0.828$ mm) and $2.52 \cdot 10^{-3}$ mm^3 (ellipsoidal axes: $d_x = 0.078$ mm, $d_y = 0.078$ mm and $d_z = 0.785$ mm) for the measurement of u and v, respectively (these estimates are provided by the manufacturer on the basis of the e^{-2} light-intensity cut-off principle, see Dantec Dynamics, 2011). The maximum laser power is 300 mW for each pair of laser beams. The LDA characteristics are summarised in Tab. 2.1, while the LDA measurement system is displayed in Fig. 2.9. Specific details about the LDA functioning can be found in e.g. Albrecht et al. (2003) and Tropea et al. (2007).

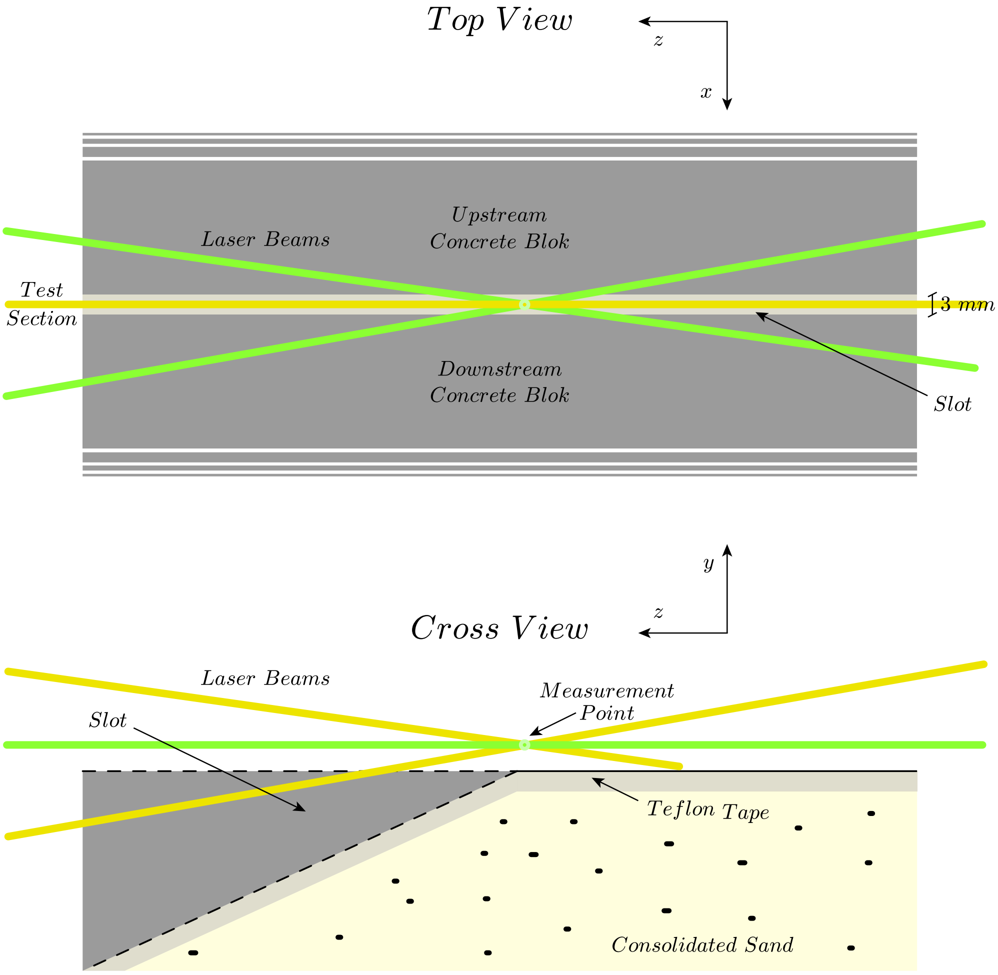

Fig. 2.8 Details of the test section configuration.

Parameter	**Units**	**Green Laser Beam**	**Yellow Laser Beam**
Wavelength	mm	532	561
Focal length	mm	300	300
Beam diameter	mm	2.6	2.6
Beam half-angle	°	5.711	5.711
Fringe spacing	μm	2.82	2.63
Number of fringes	-	29	29
Maximum power	mW	300	300
Probe volume	mm^3	$2.96{\cdot}10^{-3}$	$2.52{\cdot}10^{-3}$
Ellipsoidal axis d_x	mm	0.083	0.078
Ellipsoidal axis d_y	mm	0.082	0.078
Ellipsoidal axis d_z	mm	0.828	0.785

Table 2.1 Characteristics of the used LDA system (Dantec Dynamics, 2011).

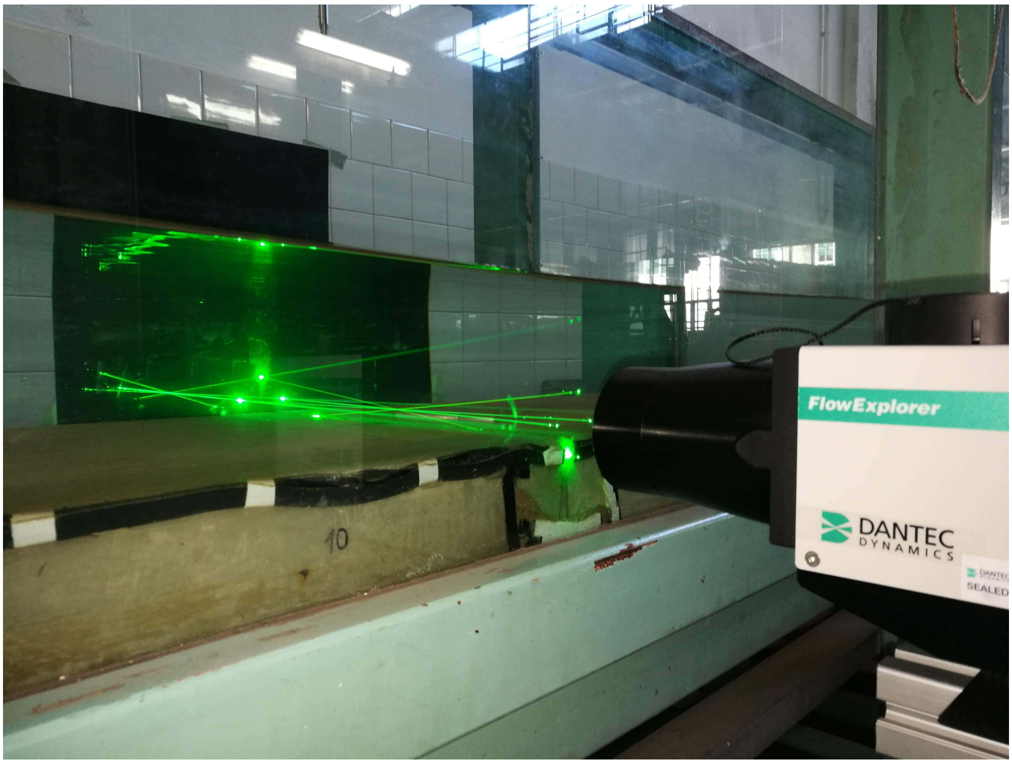

Fig. 2.9 Dantec Dynamics 2-D LDA measurement system at the test section. It can be noted how the vertical laser beam near the wall passes through the thin gap between the concrete slabs.

Signal processing was carried out with two Dantec Dynamics Burst Spectrum Analyzers (BSA F600-2D) and a dedicated Dantec software (BSA Flow Software v6.5) set up on a local PC network station. Data were always acquired in coincidence mode to allow for the estimation of the Reynolds shear stresses. The sampling frequency f_s was always between 100 Hz and 400 Hz (depending on the hydraulic conditions) and more than 500 000 velocity measurements were collected for each measurement point over a minimum duration of 40 minutes. This amount of data ensured a negligible sampling error for all the statistics presented in Section 2.5.1 (i.e. the sampling error results much smaller than the size of the marker-symbols used in the plots). The standard error SE was estimated by means of the following expressions for the mean, the variance, the standard deviation, the skewness and the kurtosis, respectively (McCrary, 2015):

$$SE_{mean} = \frac{\sigma_u}{\sqrt{N}} \tag{2.2}$$

$$SE_{variance} = \sigma_u^2 \sqrt{\frac{2}{N-1}} \tag{2.3}$$

$$SE_{std} = \sigma_u \frac{1}{\sqrt{2(N-1)}} \tag{2.4}$$

$$SE_{skewnees} = \sqrt{\frac{6N(N-1)}{(N-2)(N+1)(N+3)}} \tag{2.5}$$

$$SE_{kurtosis} = 2\sqrt{\frac{6N(N-1)}{(N-2)(N+1)(N+3)}}\sqrt{\frac{N^2-1}{(N-3)(N+5)}} \tag{2.6}$$

where, σ_u is the standard deviation of the streamwise velocity component and N is the sample size. For the wall-normal velocity component, the expressions are the same. In Tab. 2.2 the standard errors for the various statistics are reported for the representative Test 1 (see Tab. 2.3); the other tests show standard errors of the same order.

Velocity Component	SE_{mean}	$SE_{variance}$	SE_{std}	$SE_{skewness}$	$SE_{kurtosis}$
u	$6.1 \cdot 10^{-8}$	$1.8 \cdot 10^{-6}$	$3.0 \cdot 10^{-5}$	$3.5 \cdot 10^{-3}$	$6.9 \cdot 10^{-3}$
v	$2.2 \cdot 10^{-8}$	$2.4 \cdot 10^{-7}$	$1.1 \cdot 10^{-5}$	$3.5 \cdot 10^{-3}$	$6.9 \cdot 10^{-3}$

Table 2.2 Standard errors of the velocity statistics calculated for Test 1.

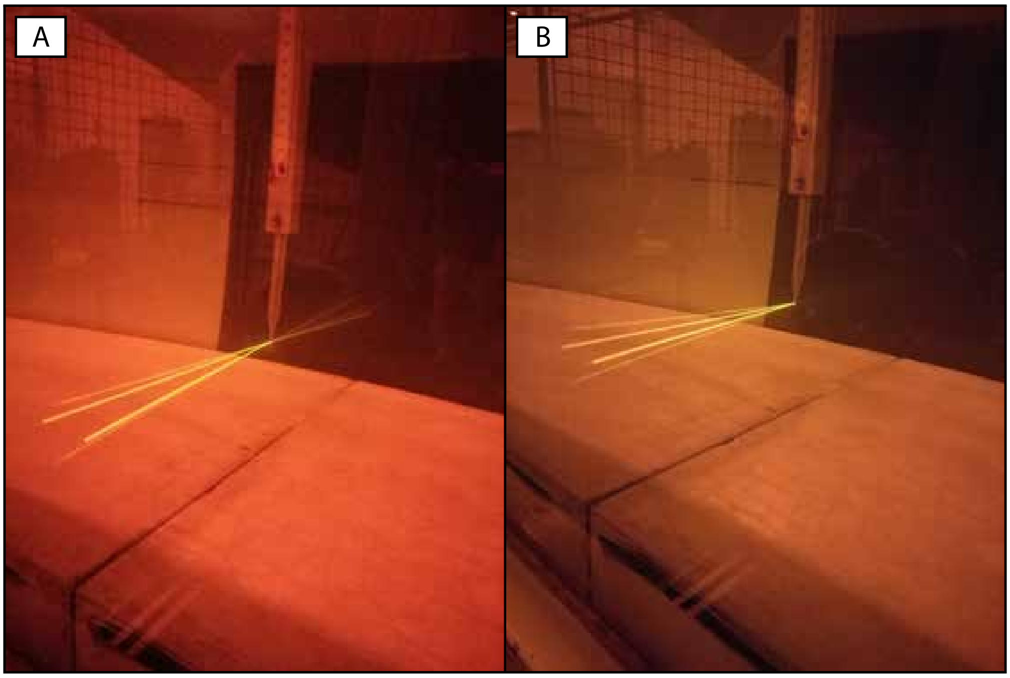

Fig. 2.10 Identification of the origin the vertical coordinate: (A) the LDA laser beams are approaching the extremity of sharp point gauge; (B) the LDA measurement volume perfectly coincide with the extremity of sharp point gauge.

The 2-D LDA optics was traversed by means of a 3-D computer-controlled Dantec Dynamics traversing system (ISEL iMC-S8 Traverse) which allows for movements along three directions with a resolution of 6 μm.

For each experiment, particular attention was dedicated to ensure that the LDA beams were perfectly aligned with the horizontal and vertical (i.e. gravity) directions. To this end, the flume was filled with water in quiescent conditions (this was possible by sealing the outlet of the flume with a steel cap). Consequently, the resulting free-surface was a perfectly horizontal plane, which was then used as a reference for the four laser-beams alignment. The origin of the vertical coordinates was identified by means of a sharp point gauge connected to a vernier calliper (accuracy of 0.05 mm) and located at a known distance from the bed. The LDA sampling volume was then moved towards the pointer and the backscatter signal monitored with the BSA Flow Software (Fig. 2.10A). While gently approaching the sampling volume towards the pointer, the backscatter signal was monitored and when it began to be disturbed by the pointer, it was assumed that the pointer and the LDA sampling volume coincided and the elevation above the bed recorded as a reference to identify the origin of the vertical axis (Fig. 2.10B). By repeating this method for multiple heights above the bed, it was observed that the zero reference level could be detected with an accuracy of about ±0.1 mm (in wall units this uncertainty varies according to the test, with an averaged value of ±1.5). It is important to note that the uneven edges of the slot, evidenced in Fig. 2.10(A–B) and mainly due to natural wear, do not affect LDA velocity measurements.

2.3 Experimental hydraulic conditions

The main parameters describing the hydraulic conditions associated with each experiment are reported in Tab. 2.3. All the experiments were carried out with a flat bed as the flume is non-tilting. This clearly implies that all the investigated flows were non-uniform. It is therefore important to specify that all the parameters reported in Tab. 2.3 refer to flow conditions measured at the test section of each trial.

For most of the experiments, the test section was located at $x = 30$ m (the longitudinal, wall-normal and spanwise coordinates are indicated with x, y and z, and defined as in Fig. 2.6c) from the origin of the x coordinate (Fig. 2.6b). Test 4 is the only exception as it was carried out at $x = 15$ m, at flow conditions similar to test 5. Test 4 was used to investigate and isolate the effects of x/h on VLSMs' scaling, while maintaining constant all the other relevant non-dimensional parameters.

Note that, all the LDA measurements related to tests 1–7 were carried in the central cross-section of the flume (i.e. $z/W = 0$, where z originates in the centreline of the flume, see Fig. 2.6c), except for tests 5a–5d (Tab. 2.3). In these tests, the flow conditions were the same as test 5, but the LDA system was traversed at four spanwise positions across the flume half-width (i.e.

Experiment	h [cm]	U_b [m/s]	u_τ [m/s]	δ_ν [μm]	l^+	Re_b	Re_τ	Fr	W/h	x/h	z/W	**Symbol**
Test 1	20.0	0.2195	0.00985	89.3	9	30150	2240	0.157	3.05	150	0.00	◆
Test 2	15.0	0.3146	0.01432	75.4	11	29310	1990	0.259	4.07	200	0.00	●
Test 3	12.0	0.1517	0.00755	120.1	7	14400	999	0.140	5.08	250	0.00	★
Test 4	10.3	0.4036	0.01836	58.7	14	28800	1752	0.402	5.92	145	0.00	✶
Test 5	10.1	0.4442	0.02016	53.1	15	31510	1904	0.446	6.04	297	0.00	■
Test 5a	10.1	0.4442	0.02016	53.1	15	31510	1904	0.446	6.04	297	0.08	▲
Test 5b	10.1	0.4442	0.02016	53.1	15	31510	1904	0.446	6.04	297	0.16	▸
Test 5c	10.1	0.4442	0.02016	53.1	15	31510	1904	0.446	6.04	297	0.24	▼
Test 5d	10.1	0.4442	0.02016	53.1	15	31510	1904	0.446	6.04	297	0.33	◂
Test 6	8.5	0.4849	0.02221	45.1	18	32180	1886	0.531	7.18	353	0.00	✖
Test 7	5.0	0.2916	0.01518	69.0	12	11960	725	0.414	12.20	600	0.00	✚

Table 2.3 Summary of experiments and associated hydraulic conditions. The columns indicate respectively: the water depth h, the bulk velocity U_b, the shear velocity u_τ, the viscous length scale $\delta_\nu = \nu/u_\tau$ where ν is the kinematic viscosity, the viscous-scaled LDA measurement length $l^+ = d_z u_\tau/\nu$ where d_z is the longest ellipsoidal axis of the LDA measurement volume, the bulk Reynolds number $Re_b = R_h U_b/\nu$ where $R_h = Wh/(W+2h)$ is the hydraulic radius and W is the channel width, the von Kàrmàn number $Re_\tau = hu_\tau/\nu$, the Froude number $Fr = U_b/\sqrt{gh}$ where g is the gravitational acceleration, the aspect ratio W/h and the non-dimensional distance from the inlet x/h. Finally, z/W indicates the normalised spanwise position for the velocity measurements, where z is the spanwise coordinate starting from the flume centreline.

$z/W = 0.08; 0.16; 0.24; 0.33$). For each z/W position, LDA measurements were taken over 19 different locations along the bed-normal coordinate. These tests were carried out to quantify the effects of lateral boundaries on the intensity and wavenumber of LSMs and VLSMs peaks in pre-multiplied spectra.

The flow depth h was determined by the ultrasonic gauge positioned in close proximity of the test section, and by doing the mean of a 30-minutes long time-series. This value was compared with the value read on a ruler (accuracy of 0.5 mm) positioned just next to the LDA. The difference in h measured by means of the two methods was well within both instruments' uncertainty.

Note that tests 1 and 2 were carried out at flow depths corresponding to aspect-ratio values below 5, which is considered the minimum to allow for turbulence statistics in the central cross-section of the flume to be independent of lateral-wall effects (Nezu and Nakagawa, 1993). These tests were carried out as they impose extreme "constraining conditions" of the lateral walls to VLSMs. Following the conjecture made by Cameron et al. (2017), it was expected that the non-dimensional length of VLSMs for these two tests was significantly lower than those pertaining to the other tests presented herein. It should be pointed out that tests 1 and 2 were made possible thanks to the remarkable length of the flume, which allowed for the development of a boundary layer as deep as the water depth (i.e. up to 20 cm). This condition is not obtained easily in standard flumes working in smooth-bed conditions.

The bulk flow velocity U_b is herein defined as the mean fluid velocity averaged over the flow depth, namely:

$$U_b = \frac{1}{h}\int_0^h U(y)\,dy \tag{2.7}$$

where $U(y)$ is the time-averaged longitudinal velocity profile measured at the test section (the averaging time window is equal to the measuring time of each test).

The shear velocity u_τ was estimated following the procedure outlined in Section 2.4. These values were then used to compute the viscous length scale $\delta_\nu = \nu/u_\tau$ and, in turn, the roughness Reynolds number $k_s^+ = k_s/\delta_\nu$, which resulted to be always lower than 5.5, hence indicating hydraulically smooth-bed flow conditions for all the tests.

Tab. 2.3 also reports the characteristic length of the LDA sampling volume l normalised with the viscous length scale, $l^+ = l/\delta_\nu$. In an attempt to provide a conservative estimation of l^+, l was taken equal to d_z as it is the largest dimension of the LDA measurement volume. The obtained values of l^+ are aligned with (and in some instances lower than) those reported in past studies about wall-turbulence (see e.g. Hutchins et al., 2009; Monty et al., 2009). Furthermore, in turbulence research, the measurement resolution is also provided by using the Kolmogorov dissipative length-scale η_k, i.e. $l_\eta = l/\eta_k = d_z/\eta_k$. The Kolmogorov length-scale η_k can be estimated as (Poggi et al., 2003):

$$\eta_k(y^+) = \frac{\nu}{u_\tau}\left(\kappa y^+\right)^{1/4}. \tag{2.8}$$

By computing η_k at the lowest y^+ for each test, the LDA resolution l_η results to span between 4.15 and 9.62.

The level of non-uniformity caused by the flat bed conditions was characterized by means of the parameter β, which was estimated as follows:

$$\beta(x) = \frac{gh(x)}{u_\tau(x)^2}\left(S_w(x) - S_0\right), \tag{2.9}$$

where S_0 is the bottom slope (clearly zero due to the flat bed conditions of the flume), $S_w = \mathrm{d}h/\mathrm{d}x$ is the gradient of the free surface and g is the gravitational acceleration. With this definition, $\beta = -1$ indicates uniform flow conditions (i.e. the flow depth has a null gradient along x), $\beta > -1$ indicates decelerating flow conditions (i.e. the flow depth has a positive gradient along x) and $\beta < -1$ stands for accelerating flow conditions (i.e. the flow depth has a negative gradient along x). In non-uniform open-channel flows, constant values of β along the longitudinal coordinate x are a signature of equilibirum flows (Kironoto and Graf, 1995) (i.e. flows where appropriately-normalised vertical profiles of velocity statistics do not depend on the streamwise coordinate and can therefore be considered self-similar). Moreover, Kironoto and Graf (1995), Song and Chiew (2001) and Pu et al. (2018) indicate that in equilibrium open-channel flows, vertical profiles of velocity statistics are dependent on β. Thus, it is important to estimate the variations of the parameter β, across all the experimental tests, to assess to what extent vertical profiles of velocity

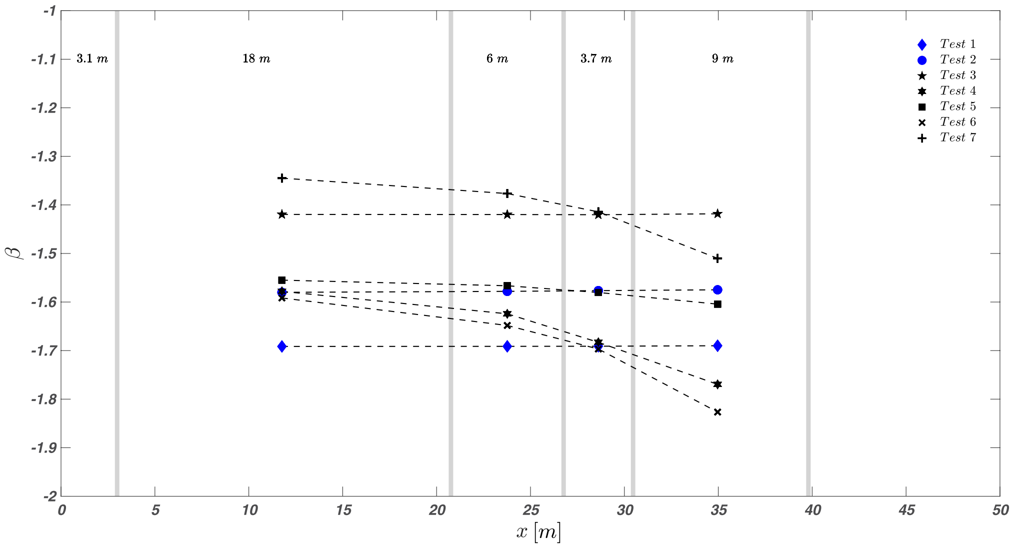

Fig. 2.11 Estimated β values along the channel flume. The grey vertical lines indicate the positions of the five ultrasonic gauges.

statistics measured at the test section are expected to collapse (or not) due to either lack of self-similarity or non-uniformity levels (i.e. local values of β).

Towards this end, the β parameter (Eq. (2.9)) was estimated as follows: the free-surface water profile was approximated by linearly connecting each water depth measurement $h(x)$ provided by the ultrasonic gauges. This allowed for the estimation of four values of the water-surface gradient $S_w(x)$, which were considered representative of four cross-sections located halfway between two subsequent ultrasonic gauge positions. In those positions, also the water depth $h(x)$ was estimated. In Eq. (2.9), the shear velocity $u_\tau(x)$ was estimated, through the bulk momentum-balance principles, as: $u_\tau = \sqrt{gS_fR_h}$, where $S_f = \mathrm{d}E/\,\mathrm{d}x$ is the energy-grade-line slope, E is the specific energy and R_h is the hydraulic radius.

The results are reported in Fig. 2.11. As can be seen, the parameter β varies at most of 7% for each individual test, whereas, it varies between -1.35 and -1.83 among all tests. The literature pertaining to non-uniform open-channel flows (Kironoto and Graf, 1995; Pu et al., 2018; Song and Chiew, 2001) indicates that, such variations in β are associated with variations in the second-order velocity statistics of less than 6% for each individual tests and 10% among all the tests. These variations are rather small and, as discussed in the next

Section, comparable to the relative error associated with the estimation of the shear velocity u_τ. It is therefore expected that appropriately-normalised profiles of velocity statistics pertaining to different tests should collapse with a general scatter of about 10%.

In support of the presence of self-similar flows, it is worth noting that test 4 and test 5 were carried out at two different test sections (i.e. 15 m and 30 m from the origin of the x coordinate, respectively) with very similar local values of β. When the velocity statistics for the two tests were compared, they displayed an excellent collapse (see plots in Section 2.5.1).

2.4 Estimation of the shear velocity

The shear velocity is defined as $u_\tau = \sqrt{\tau_0/\rho}$, where τ_0 is the bed shear stress and ρ is the fluid density. The total shear stress τ_{tot} at any water depth for smooth-bed flow can be estimated as:

$$\frac{\tau_{tot}(y)}{\rho} = -\overline{u'v'}(y) + \nu \frac{\mathrm{d}U(y)}{\mathrm{d}y} \tag{2.10}$$

where, u' and v' are the longitudinal and vertical fluctuating velocity components, respectively, and over-bar stands for time-averaging. In uniform-flow conditions, τ_{tot} depends linearly on the vertical coordinate and τ_0 can be easily determined from extrapolation of τ_{tot}-profiles to the bed.

In non-uniform flows (as in the present case) the estimation of τ_0 and, consequently, of u_τ, is much more difficult because the dependence of τ_{tot} on the vertical coordinate is not known a-priori and any extrapolation of τ_{tot} to the bed can be affected by significant errors. For tests 1−2, such estimation is further complicated by the fact that τ_{tot}-profiles might also be affected by the presence of secondary currents that, given the low aspect ratio of the tests, can contribute significantly to momentum transfer, especially in the outer part of the flows.

In light of these considerations, it was decided to estimate u_τ by means of the Clauser method (Clauser, 1956). Despite being based on fairly strong assumptions, the Clauser method (or its variations) is still widely used in turbulent wall-flows research (see e.g. Chauhan et al., 2009; Monty et al., 2009; Rodríguez-López et al., 2015; Vanderwel and Ganapathisubramani, 2019). The Clauser methods is based on the assumption that, in a flow region close to the wall, the vertical profile of the mean velocity follows a logarithmic behaviour. This hypothesis has been tested for uniform and non-uniform open-channel flows even at low aspect-ratios (Cardoso et al., 1989, 1991; Kironoto, 1998; Kironoto and Graf, 1995). The procedure adopted for quantifying the shear velocity for each test goes as follows. The classical logarithmic law for the longitudinal time-averaged mean velocity reads as:

$$U^+ = \frac{1}{\kappa} \ln\left(y^+\right) + B \tag{2.11}$$

where κ and B are the von Kàrmàn and the additive constant, respectively, and the superscript "+" refers to normalisation of lengths and velocities by means of the viscous length scale (ν/u_τ) and the shear velocity (u_τ), respectively. Assuming κ equal to 0.41, the best fit between Eq. (2.11) and the experimental velocity data located above $y^+ = 50$ and below $y/h = 0.2$ provides the estimation for the shear velocity and B. In particular, an average value of B equal to 5.5 guarantees the most suitable collapse among all the velocity profiles. In order to show better the reliability of the parameters obtained, also the diagnostic function Ψ was defined as the subtraction of Eq. (2.11) from the measured mean velocity profile:

$$\Psi = U^+ - \frac{1}{\kappa} \ln\left(y^+\right) - B \tag{2.12}$$

In the logarithmic region, Ψ must exhibits values approximately equal to zero for the chosen values of B, κ and u_τ. Fig. 2.12 demonstrates the good collapse of data within the range of elevations $50 \leq y^+ \leq 400$.

As shown in Section 2.5.1, the estimated values of u_τ lead to a satisfactory collapse of the first and second-order velocity moments. The values obtained for the constants κ and B well fall within the ranges identified by the literature pertaining to smooth-bed open-channel flows, i.e. $\kappa = 0.4 - 0.43$ and $B = 5 - 5.5$ (Cardoso et al., 1989, 1991; Kirkgöz, 1989; Kirkgöz and Ardiçlioğlu, 1997; Nezu and Nakagawa, 1993; Nezu and Rodi, 1986; Onitsuka et al., 2009; Pu et al., 2018; Roussinova et al., 2008; Steffler et al., 1985).

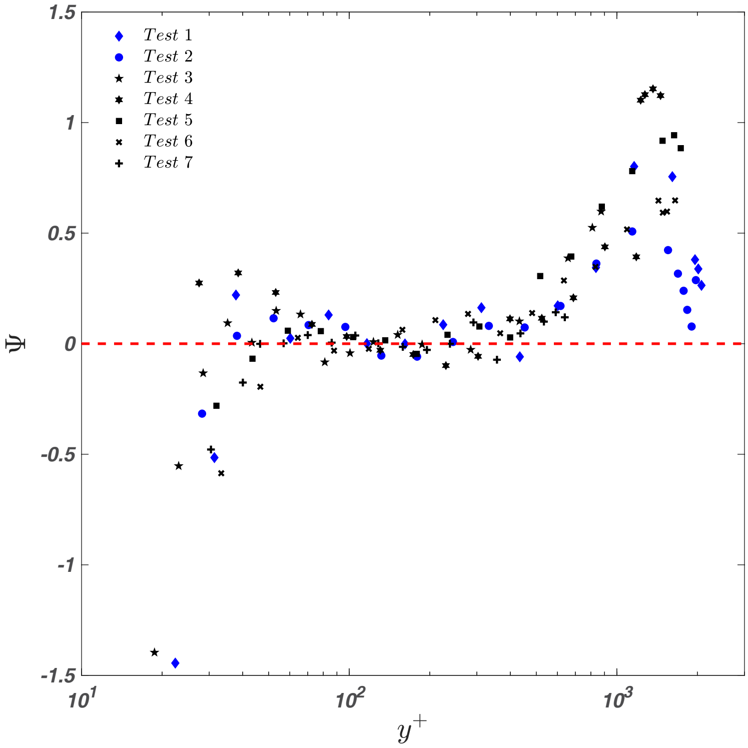

Fig. 2.12 Variation of the Ψ function for the various tests.

In order to further confirm the reliability of the procedure described above, the shear velocity u_τ was also estimated from bulk momentum-balance principles $u_\tau = \sqrt{gS_f h}$. These values were then corrected according to the empirical formulation provided by Knight et al. (1984) in order to obtain values that are representative of the mid cross-section and thereforehence comparable with those obtained from the Clauser method described above. Tab. 2.4 shows that the estimations of u_τ obtained by using the two methods are in good agreement among all tests. Relative errors (%R.E.) are bounded between 1.6% and 4.9% except for test 1, whereby estimated values of u_τ deviate of about 9.7%. Taking a conservative approach, it can be concluded that the u_τ-values provided by the Clauser method are subjected to an uncertainty of, at most, 10%. They are used to scale velocity statistics presented in Section 2.5.

Estimation method	**Test 1**	**Test 2**	**Test 3**	**Test 4**	**Test 5**	**Test 6**	**Test 7**
Clauser method	0.00985	0.01432	0.00755	0.01836	0.02016	0.02221	0.01518
Knight et al. (1984)	0.00890	0.01408	0.00742	0.01915	0.02091	0.02329	0.01597
R.E. (%)	9.7	1.6	1.8	4.1	3.6	4.6	4.9

Table 2.4 Estimated values of u_τ (in m/s) at the mid cross-section using the Clauser method applied to the measured mean velocity profiles and the empirical approach by Knight et al. (1984). The last row of the table reports the percentage relative error R.E. between the two estimates.

2.5 Results

Before addressing the issue of large-scale structures, an introductory section discussing classical one-point statistics is herein presented in order to validate the experimental methodology that has been described in the previous sections. This is achieved by providing evidence that such statistics, when appropriately scaled, are consistent with the data presented in the past literature. Furthermore, the following results might enrich the rather scarce set of published data on turbulence in smooth-bed open-channel flows and, perhaps, provide a benchmark for comparison with other canonical wall-flows.

2.5.1 One-point statistics

Fig. 2.13(a–d) reports the first and second-order velocity moments in classical inner scaling. Fig. 2.13(a) reports the normalised longitudinal mean velocity profile together with the logarithmic law (Eq. (2.11)). It can be seen that, although the Clauser method, which was used to estimate u_τ, was applied to a fixed range of elevations that range between $y^+ = 50$ and $y/h = 0.2$ (as often done in wall-turbulence studies), the upper boundary of the log-region extends further away from the bed, i.e. up to $y/h = 0.35$ (this is best seen in Fig. 2.14a).

Fig. 2.13(b) and Fig. 2.13(c) report the non-dimensional standard deviation of the longitudinal (σ_u/u_τ) and bed-normal velocity component (σ_v/u_τ), respectively. Starting from $y^+ > 35$, Fig. 2.13(b) shows a systematic dependence of σ_u/u_τ on Re_τ, as already extensively observed both in open-channel flows (Nezu and Nakagawa, 1993; Poggi et al., 2002) and in other wall-flows (De Graaff and Eaton, 2000; Durst et al., 1995; Marusic et al., 2010; Smits et al., 2011).

The σ_v/u_τ profiles shown in Fig. 2.13(c) exhibit a plateau that increases its extent with increasing Re_τ. The σ_v/u_τ value at the plateau is about $1 - 1.11$, consistently with previous works on smooth-bed open-channel flows (Nezu and Nakagawa, 1993; Poggi et al., 2002) as well as other wall-flows (Durst et al., 1995; Wei and Willmarth, 1989).

The normalised Reynolds shear stress profiles $-\overline{u'v'}/u_\tau^2$ follow a similar trend (Fig. 2.13d) showing a plateau which increases in extent (along the vertical coordinate) with increasing Re_τ. The value of $-\overline{u'v'}/u_\tau^2$ at the plateau also

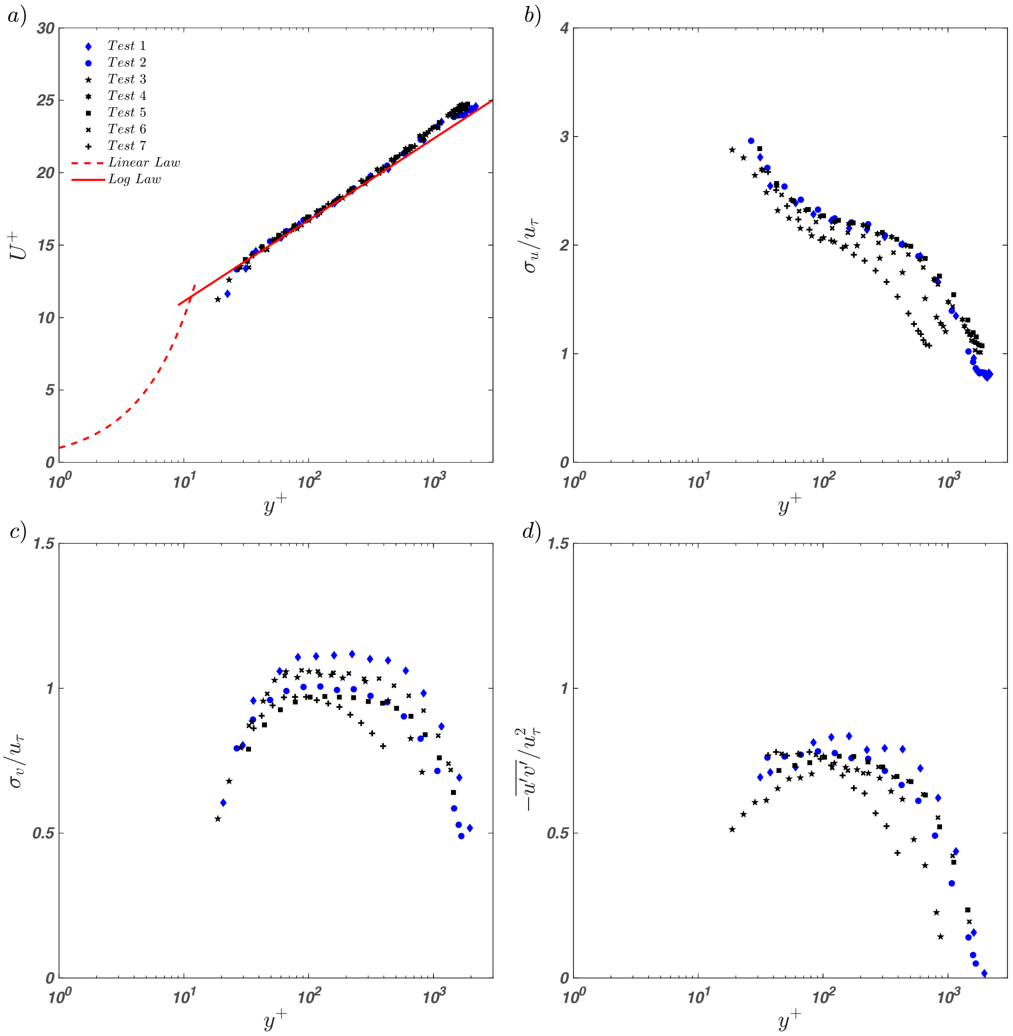

Fig. 2.13 Inner scaling: (a) normalised streamwise mean velocity; (b) normalised standard deviation of the streamwise velocity fluctuations; (c) normalised standard deviation of the wall-normal velocity fluctuations; (d) normalised Reynolds shear stress. The dashed and continuous lines represent the linear and the log law of the wall.

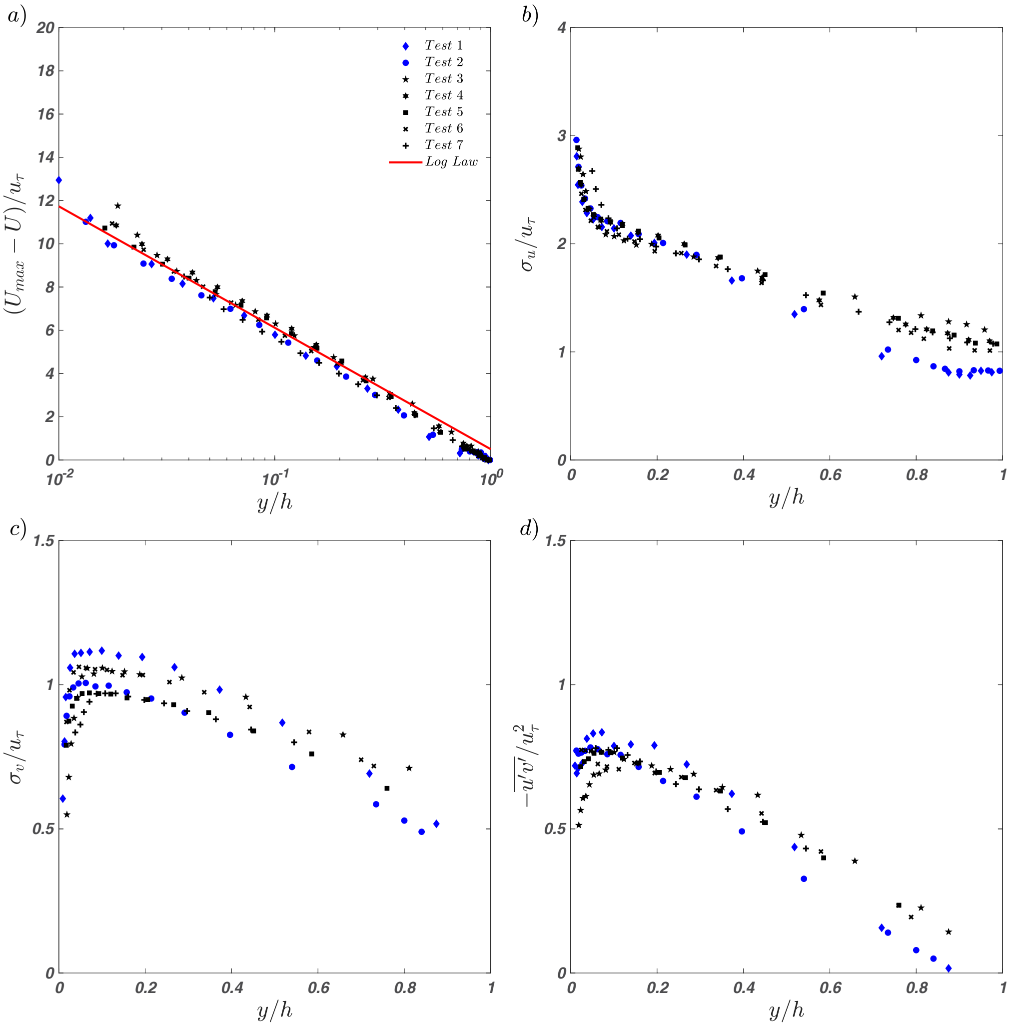

Fig. 2.14 Outer scaling: (a) normalised streamwise mean velocity; (b) normalised standard deviation of the streamwise velocity fluctuations; (c) normalised standard deviation of the wall-normal velocity fluctuations; (d) normalised Reynolds shear stress. The continuous line is the velocity-defect law.

increases with increasing Re_τ from 0.75 to 0.85, reflecting the weakening of the viscous shear stresses with increasing Reynolds number. This behaviour is also in good agreement with the past literature on open-channel flow studies (Nezu and Nakagawa, 1993; Poggi et al., 2002; Roussinova et al., 2008).

Fig. 2.14(a–d) reports first and second-order velocity moments in classical outer scaling. For $y/h > 0.03$, mean velocity-defects $U_{max} - U$ collapse very well (Fig. 2.14a) on a curve described by the well-known logarithmic law in outer-scale normalisation:

$$\frac{U_{max} - U}{u_\tau} = -\frac{1}{\kappa} \ln\left(\frac{y}{h}\right) + B_1 \tag{2.13}$$

where $B_1 = 0.5$ provides the best fit of the experimental data located at $y/h > 0.03$. In general, B_1 is related to the wake strength parameter Π as $B_1 = 2\Pi/\kappa$[3]. Kironoto and Graf (1995) reports that the wake strength parameter retains a dependence on the non-uniformity parameter β as $\Pi = 0.08\beta + 0.23$. By using $\beta = -1.59$, which is the average taken over all the measured values of β reported in Fig. 2.11, Π results equal to 0.103, which compares very well with $\Pi = \frac{1}{2}\kappa B_1 = 0.102$ if $\kappa = 0.41$.

Normalised standard deviations and shear Reynolds stresses (Fig. 2.14b–d) collapse fairly well, although, with respect to mean velocities, they display a slightly higher level of scatter. However, it should be noted that most of the scatter occurs for $y/h > 0.5$ and is due to the data pertaining to tests 1 and 2. This was reasonably expected because these experiments were characterised by a low aspect ratio that made velocity statistics susceptible to significant lateral-wall effects. Such effects are obviously expected to increase in significance with increasing distance from the bed. Focusing on the other high-aspect ratio experiments, the scatter is within 10%. As already discussed, this could be due to either different values of the β parameter among the tests or to inaccuracy in the estimation of u_τ.

In the flow region approximately located at $0.1 < y/h < 0.4$, data pertaining to σ_u/u_τ (Fig. 2.14b) do not collapse but seem to stratify following a Re_τ-

---

[3] More precisely, in the log-wake formulation, $B_1 = \frac{2\Pi}{\kappa}\cos^2\left(\frac{\Pi y}{2h}\right)$ (Nezu and Nakagawa, 1993), where $\cos^2\left(\frac{\Pi y}{2h}\right)$ is the so-called wake function that depends on the distance from the wall y/h. Hence, B_1 ranges from the value $\frac{2\Pi}{\kappa}$ at the wall to the null value at the free-surface.

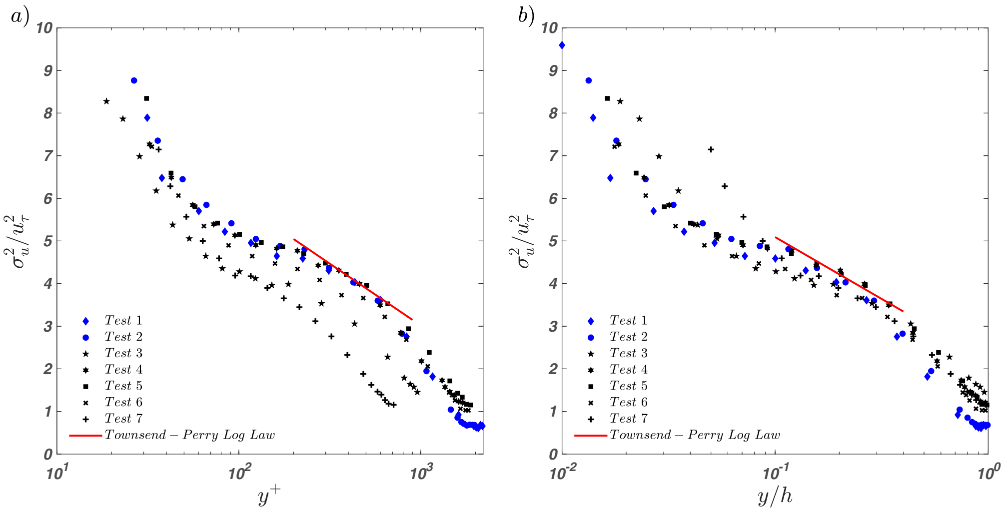

Fig. 2.15 Variance of streamwise turbulence in: (a) inner and (b) outer scaling. The continuous line is the Townsend-Perry log law (Eq. (2.14)). Only the tests with a $Re_\tau > 1700$ exhibit a logarithmic zone.

dependence. This is best seen and easier to interpret in Fig. 2.15(a–b), where variances are plotted in place of standard deviations using both inner and outer coordinates. In recent years, due to the availability of very high Reynolds-number experiments, great efforts have been directed in order to test and validate the Townsend attached-eddy hypothesis (Marusic and Monty, 2019; Perry and Chong, 1982; Perry et al., 1986; Townsend, 1976). Simply put, this theory propose that, somewhat close to a solid wall, the turbulent flow field is composed by a superposition of eddies that scale linearly with the wall distance y. From this concept, Townsend demonstrated that the non-dimensional variance of the longitudinal velocity component should follow a logarithmic behaviour in both inner and outer coordinates, as:

$$\frac{\sigma_u^2}{u_\tau^2} = D_I - A_1 \ln\left(y^+\right) = D_O - A_1 \ln\left(\frac{y}{h}\right) \tag{2.14}$$

In canonical wall-flows, the parameters D_I and D_O were shown to display flow-type and Reynolds-number dependence and being mutually linked by the following relation: $D_O = D_I - A_1 \ln Re_\tau$, where A_1 is the Townsend-Perry constant, which is considered to be constant and equal to 1.26 (Marusic et al., 2013; Meneveau and Marusic, 2013; Örlü et al., 2017). For open-channel flows, the existence of such a logarithmic behaviour has often been overlooked,

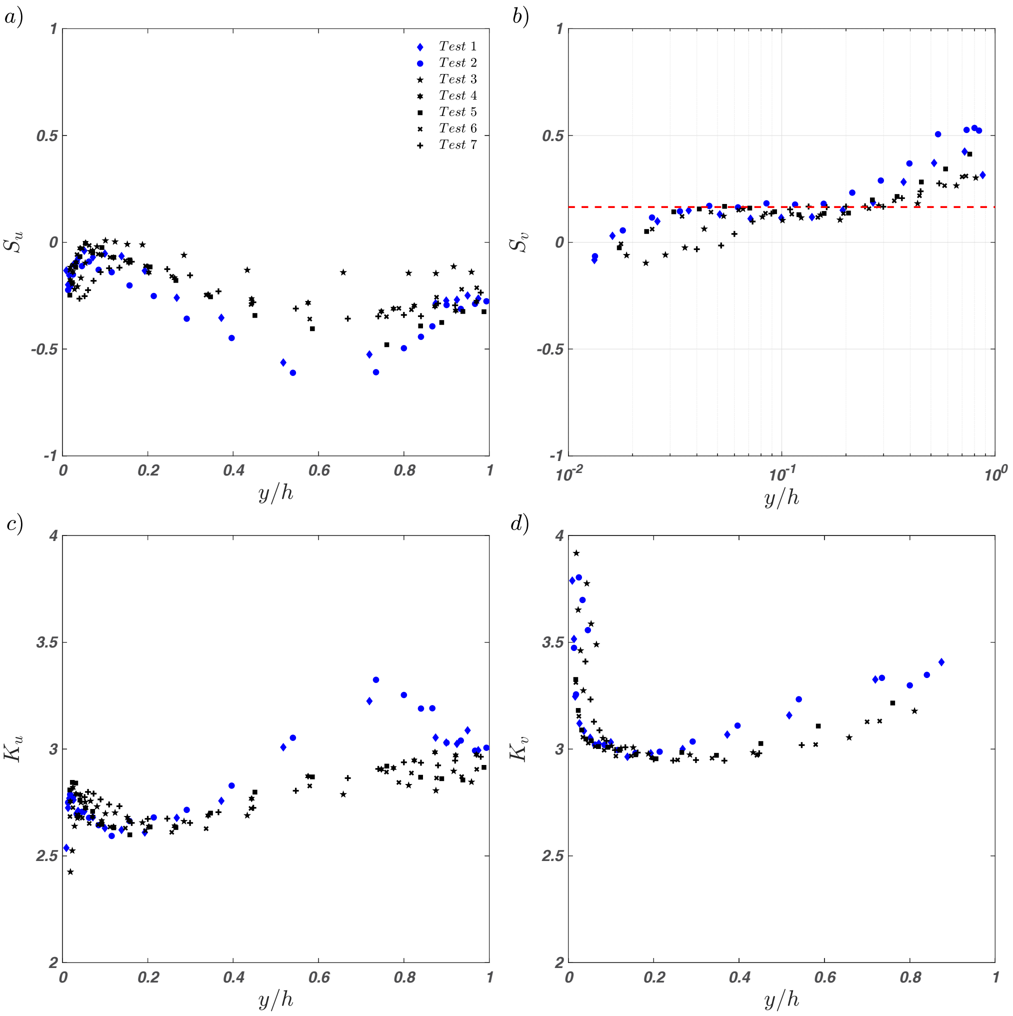

Fig. 2.16 Measured (a) streamwise skewness; (b) wall-normal skewness; (c) streamwise kurtosis; (d) wall-normal kurtosis.

although some other logarithmic-type relationships were proposed (see López and García, 1999; Nikora and Goring, 2000b). Fig. 2.15(a–b) shows that, for the highest Re_τ-experiments presented herein (i.e. tests with $Re_\tau > 1700$), a logarithmic layer seems to appear for $0.12 \leq y/\delta \leq 0.35$ and $200 \leq y^+ \leq 700$. The experimental data follow Eq. (2.14) (the continuous line in Fig. 2.15(a–b)) with a Townsend-Perry constant equal to 1.26, while the other parameters are $D_I = 11.72$ and $D_O = 2.19$. It is emphasized that the proposed logarithmic layer is clearly not developed enough (i.e. developed for at least one decade in logarithmic scale) to reach firm conclusions on its actual existence and, towards this end, experiments at much higher Re_τ should be carried out. However, the trend of the tests with $1700 < Re_\tau < 2000$ (test 1 and 2 were not analysed because they are associated with low aspect ratios, which implies velocity statistics being influenced by lateral wall effects) is in accordance with the shape exhibited in the other canonical flows with equivalent von Kármán (see the profile reported in De Graaff and Eaton, 2000; Fernholz and Finley, 1996; Hoyas and Jiménez, 2006; Hultmark et al., 2012; Morrison et al., 2004).

Fig. 2.16(a–d) presents the third and fourth-order standardised velocity moments (skewness and kurtosis) in usual outer-scale coordinates. From a hydrodynamic point of view, they are important factors in describing bursting events characteristics (Nezu and Nakagawa, 1993). The skewness gives information on the magnitude of sweep or ejection events (i.e. high-speed parcels of fluid approaching the wall and low-speed parcels of fluid parting ways from the wall; Wallace et al., 1972), while the kurtosis describes the intermittence of such turbulent events (Lacey and Roy, 2008; Nakagawa and Nezu, 1977). Except for tests 1 and 2, which display a different behaviour, all the experimental data for $y/h > 0.2$ collapse in curves that resemble those published in the literature pertaining to open-channel flows over smooth walls (Poggi et al., 2002). With respect to the other tests, for $y/h > 0.4$, tests 1 and 2 are characterised by significantly-higher absolute values of skewness and kurtosis of both velocity components. The sign of S_u and S_v (Fig. 2.16a–b) suggests that ejection events in the outer layer are relatively more energetic in test 1 and 2 than in the other tests. Furthermore, the higher values of K_u and K_v indicate that such events occur rather intermittently (i.e. more intermittently than in the other tests). The authors do not have an argument to explain why low-aspect-ratios should trigger such a different behaviour in terms of skewness and kurtosis so these results are left as the subject of future investigations.

It is interesting to note that, for all tests, the skewness of the vertical velocity component S_v displays a peculiar behaviour whereby a plateau of $S_v \approx 0.17$ occurs over a range of distances from the bed which increases in extent with increasing Re_τ but it is always bounded below $y/h = 0.2 - 0.3$ (Fig. 2.16b). As conjectured by Manes et al. (2011), the extent of the plateau and the way it depends on Re_τ share a lot in common with the overlap (logarithmic) layer of the mean velocities. This can be somewhat justified by the fact that S_v relates to part of the vertical turbulent flux of turbulent kinetic energy (i.e. the vertical turbulent transport of σ_v^2), which is expected to be constant in the overlap layer, where production and dissipation are in equilibrium (López and García, 1999; Townsend, 1961).

2.5.2 Spectral analysis of the u-component

The one-dimensional (1-D) power spectral density of the longitudinal velocity component $E_{xx}(k_x)$ in the wavenumber domain can be estimated from its frequency counterpart $E(f)$ by using the Taylor frozen-turbulence hypothesis (Taylor, 1938). In particular, defining the streamwise wavenumber k_x as:

$$k_x = \frac{2\pi f}{U_c} \tag{2.15}$$

where f is the frequency and U_c is the eddy-convection velocity, the two power spectral densities are related by:

$$E_{xx}(k_x) = \frac{U_c}{2\pi} E(f) \tag{2.16}$$

In what follows, U_c is taken as the local mean velocity $U(y)$ at each elevation y of interest.

It is well-known that 1-D spectra suffer of aliasing effects (Tennekes and Lumley, 1972), which artificially amplify the power spectral density of low frequency components. Further significant distortions may arise from the use of the Taylor hypothesis, when passing from the frequency to the wavenumber

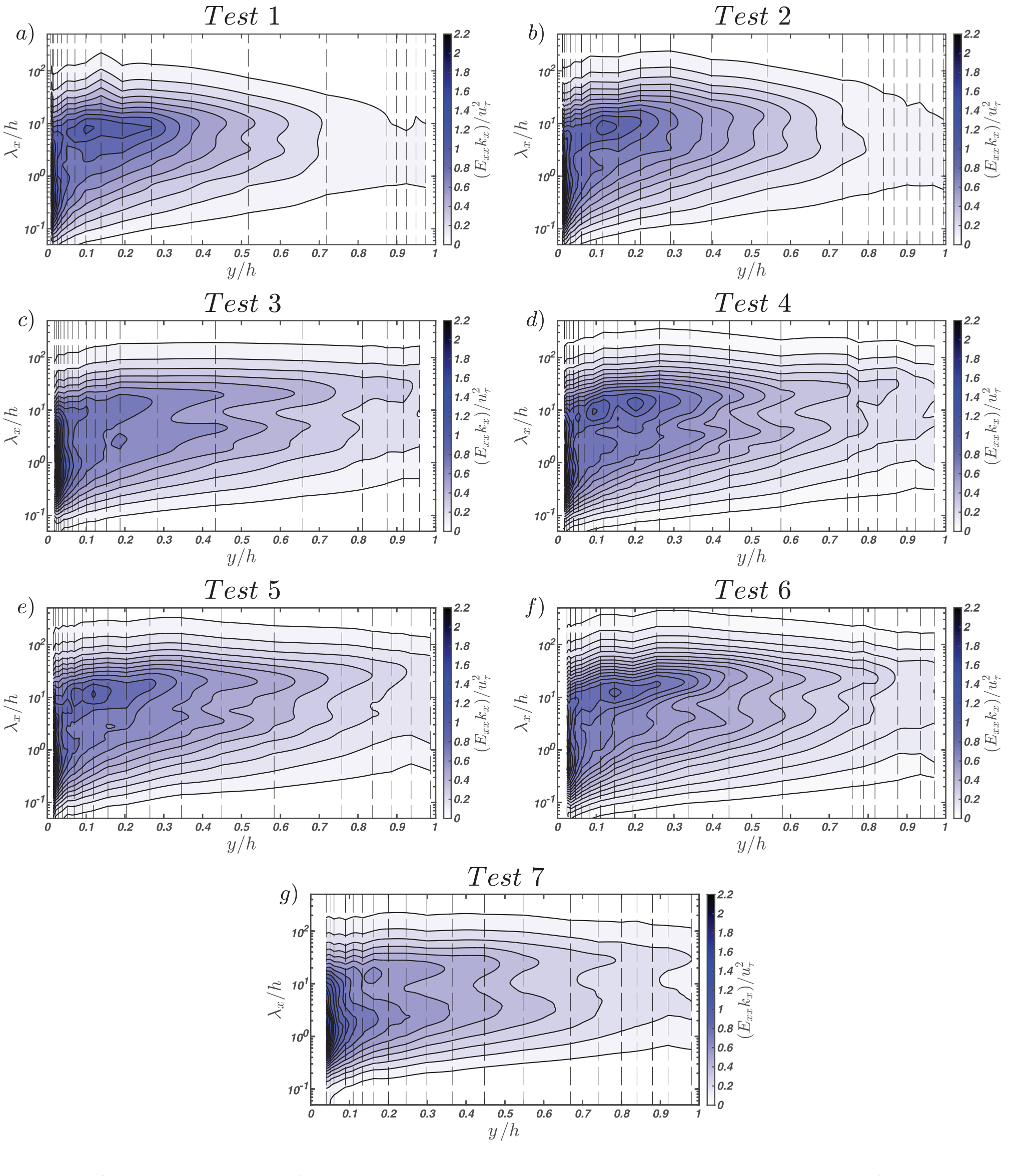

Fig. 2.17 Contour maps of the outer-scaled pre-multiplied 1-D spectra of the longitudinal velocity component $(E_{xx}k_x/u_\tau^2)$ as a function of non-dimensional streamwise wavelength (λ_x/h) and distance from the wall (y/h). The dashed lines indicate the bed-normal elevations where measurements were taken.

domain, especially when studying turbulence in the near-wall region (Cameron et al., 2017; del Álamo and Jiménez, 2009; Guala et al., 2006; Kim and Adrian, 1999).

Despite these shortcomings, 1-D spectra have represented the key method to infer the scaling of large-scale structures in wall-flows. Thus, they are also employed in the present paper to allow for a direct comparison with past studies. In order to minimize the spectral distortion due to the adoption of Taylor's hypothesis, in what follows the results are discussed for the flow region above $y/h = 0.1$, where such distortion is significantly weaker than in the near-wall region (Nikora and Goring, 2000a). Results for $y/h < 0.1$ are reported for completeness but are not discussed in depth and should be taken with care.

In order to provide a comprehensive picture of the energy distribution among different length-scales, contour maps of pre-multiplied spectra are displayed in Fig. 2.17(a–g) for all the tests. The horizontal and vertical axes of each panel in Fig. 2.17 report the distance from the wall in outer-scaling y/h and the normalised wavelength λ_x/h, respectively (where $\lambda_x = 2\pi/k_x$).

Fig. 2.17(a–g) demonstrates the existence of a double peak in the pre-multiplied spectra at wavelengths commensurate to those reported in the literature on wall-bounded flows for LSMs ($\lambda_x/h \approx \mathcal{O}(1)$) and VLSMs ($\lambda_x/h \approx \mathcal{O}(10)$).

For high aspect ratio experiments (i.e. tests 3, 4, 5, 6, and 7 with $W/h > 5$), the spectral footprint of both LSMs and VLSMs lasts up to and, in some cases even beyond, $y/h = 0.8$. This is at odds with what observed in turbulent boundary layers and duct flows (i.e. closed-channel and pipe) (Monty et al., 2009), where VLSMs disappear at much lower y/h. Indeed, in turbulent boundary layers and duct flows only LSMs persist beyond $y/\delta \approx 0.2$ (Adrian et al., 2000; Balakumar and Adrian, 2007; Monty et al., 2009) and $y/\delta \approx 0.6$ (Guala et al., 2006; Monty et al., 2009), respectively. The double-peak persistency in open-channel flows was also reported by Cameron et al. (2017) and hence it seems to be a peculiarity of this class of flows.

The double peak is evident also for test 7 (Fig. 2.17g), which is characterized by a fairly low $Re_\tau = 725$. This result supports the findings of Wang and Richter (2019), who reports bimodal pre-multiplied spectra of the streamwise velocity component for Re_τ as low as 550. Once again, this seems to be a peculiar characteristic of open-channel flows as, in canonical wall-flows, Hutchins and

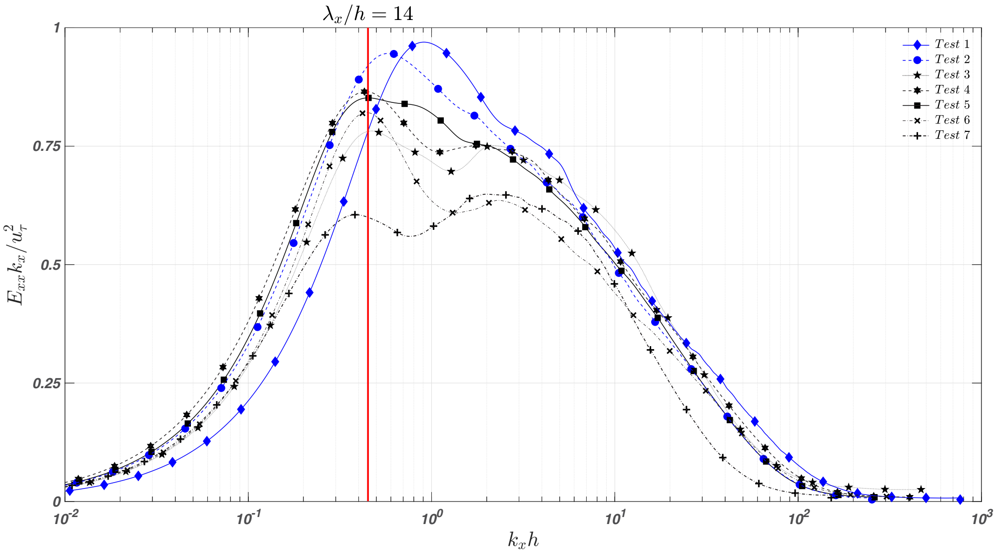

Fig. 2.18 Pre-multiplied 1-D spectra of the longitudinal velocity component taken at $y/h = 0.2$. The red line indicates $\lambda_x/h = 14$.

Marusic (2007b) identified a minimum $Re_\tau \approx 1700$ for the VLSM peak to clearly appear in pre-multiplied spectra.

Low aspect ratio experiments (i.e. tests 1 and 2 with $W/h < 5$) display some differences with respect to the other tests. In particular, the peak pertaining to VLSMs disappears at $y/h = 0.7$ and does not reach the water surface (Fig. 2.17a–b), whereas it happens instead for tests 3–7 (Fig. 2.17c–g). Most importantly, λ_x/h for tests 1 and 2 are significantly smaller than in all other tests.

From Fig. 2.18, the pre-multiplied spectra at $y/h = 0.2$ can be compared. The signature of the VLSMs is traceable for all the tests. In contrast, at this elevation, the LSMs footprint is not so clear for all the cases (in particular for tests 1, 2 and 5). It is evident how the VLSM peaks for tests 3, 4, 5 and 6 have almost the same values ($\lambda_x/h \approx 14$) while tests 1, 2 and also 7 start to deviate from this value.

In order to have a clearer and general picture about the size and scaling of large-scale structures, Fig. 2.19 reports the wavelengths corresponding to spectral peaks pertaining to both LSMs and VLSMs for all experimental tests. Fig. 2.19 also reports, for comparison, the empirical fit for VLSM-

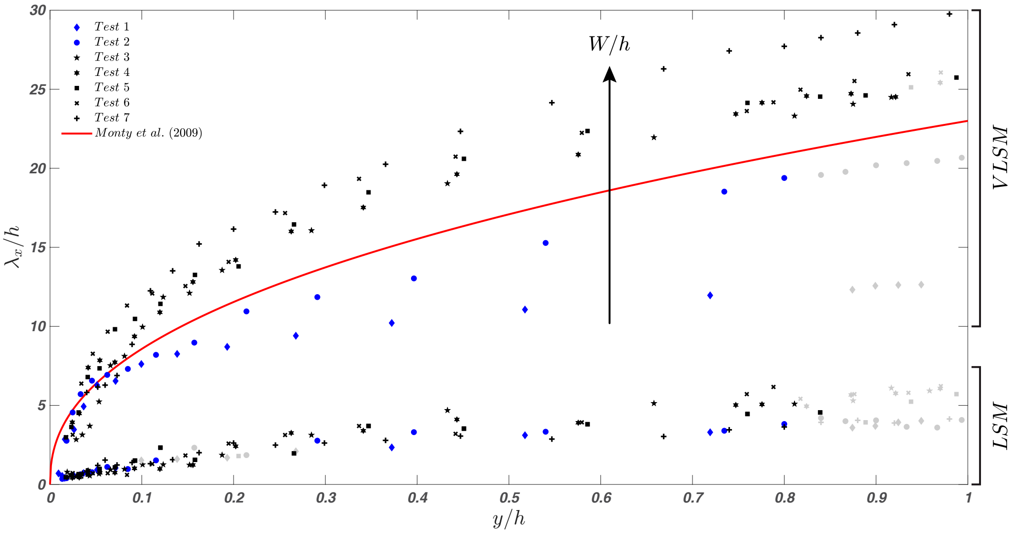

Fig. 2.19 LSM and VLSM h-normalised wavelengths peaks in the pre-multiplied 1-D spectra of the longitudinal velocity component. The light grey markers indicate situations where LSM or VLSM peaks were not clearly detectable because poorly pronounced. The red line corresponds to the relation between normalised VLSM-wavelengths and normalised elevations proposed by Monty et al. (2009) for duct flows.

wavelengths proposed by Monty et al. (2009) for pipe and closed-channel flows (i.e., $\lambda_x/\delta = 23\,(y/\delta)^{3/7}$, where $\delta = h$ for open-channel flows).

There are numerous interesting features that emerge from Fig. 2.19. Firstly, the LSM-wavelengths scale well with the flow depth h regardless of flow conditions and resemble quite closely the results presented by Cameron et al. (2017). VLSMs' wavelengths, instead, do not scale with the flow depth h and are strongly dependent on the aspect ratio W/h. In fact, tests 3–6, which were carried out with a similar aspect ratio (i.e. spanning between approximately 5 and 7), are characterised by non-dimensional VLSMs' wavelengths λ_x/h collapsing well in one curve. Test 7, instead, shows results deviating significantly from such curve (especially for $y/h > 0.35$) and it was carried out at a much higher aspect ratio ($W/h \approx 12$).

Perhaps the most interesting and striking result from Fig. 2.19 emerges from the data pertaining to the low aspect-ratio experiments, namely tests 1 and 2. The non-dimensional VLSM wavelengths pertaining to these tests decrease quite dramatically over a rather small variation of W/h between 4.07 (test 2) and 3.05 (test 1). Such wavelengths, also, drop well below the curve identified by Monty et al. (2009) for channel and pipe flows. On the contrary, LSM wavelengths keep scaling well with the flow depth h as for the other shallower flows.

One may argue that the effects of the aspect ratio W/h are not isolated in all these tests as also Re_τ and x/h vary extensively. A careful examination of the data, though, indicates that this is unlikely to occur. For example, a comparison between tests 4 and 5 allows to single out the effects of x/h (which varies extensively between 145 and 297) on VLSMs-scaling as W/h and Re_τ are kept reasonably constant. Fig. 2.19 indicates that such effects are indeed negligible. As far as Re_τ is concerned, its effects are singled out reasonably well in tests 3–6 where it varies between ≈ 1000 and ≈ 1900. Again, the results from Fig. 2.19 indicate that, non-dimensional VLSMs wavelengths for all the other tests seem to be Re_τ-independent. Therefore, the only parameter that explains well the variations of VLSMs' wavelengths observed across all the tests is the aspect ratio W/h. This result provides further evidence to support the conjecture made by Cameron et al. (2017) that VLSMs and LSMs scale with different parameters. In particular, our data demonstrate unambiguously that, while LSMs scale well with the flow-depth, the size of VLSMs is dictated by the aspect ratio W/h. To further corroborate this result, 1-D spectra were also computed using the bulk velocity U_b (Tab. 2.3) instead of the local velocity $U(y)$ in Eqs. (2.15) and (2.16) and the final conclusions proved to be independent on the choice of the convection velocity.

For completeness, Fig. 2.20(a–b) also shows the spectral energy associated with both LSM- and VLSM-peaks reported in Fig. 2.19. The 95% confidence interval for each spectral energy estimation is also provided to identify statistically significant differences between data. Since all data-points were characterised by very similar confidence intervals, these are reported only for one test to avoid figure overcrowding. In Fig. 2.20(a–b) the shear velocity squared provides a fairly good collapse of data, at least for $y/h > 0.4$. Below this level, namely for for $0.1 < y/h < 0.4$, the energy pertaining to LSM-peaks collapses very well for all tests (Fig. 2.20a). Instead, data-points related to VLSM-peaks seem to display some sort of stratification (Fig. 2.20b). It is difficult to discern whether this is dictated by Re_τ or the aspect ratio W/h. However, since tests 2 and 5 were carried out at very similar Re_τ (but very different W/h) and are characterized by the same energy in the VLSMs peaks, it can be reasonably

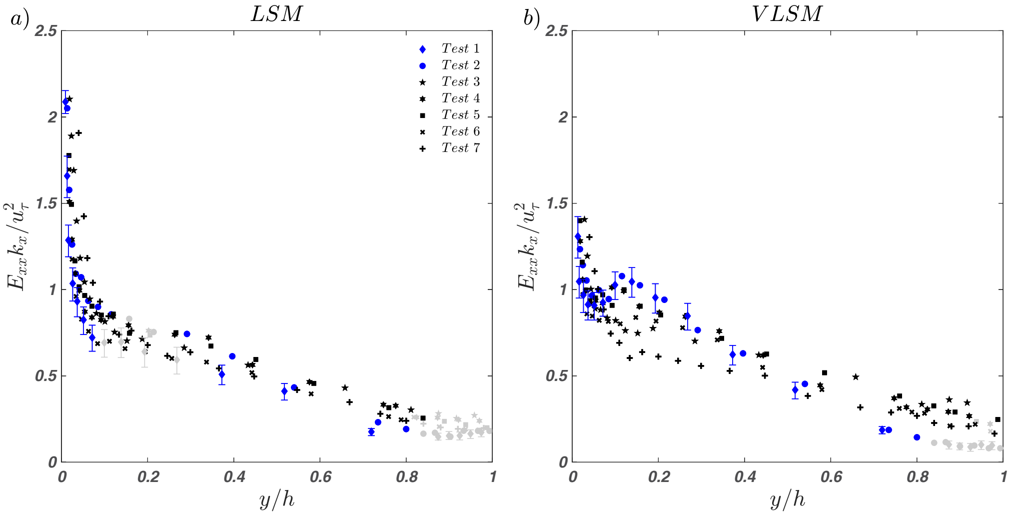

Fig. 2.20 (a) Spectral energy associated with LSM peaks normalised with u_τ^2; (b) spectral energy associated with VLSM peaks normalised with u_τ^2. The light grey markers have the same meaning as described in Fig. 2.19. The error bars indicate the confidence interval bounds (with a 95% confidence level).

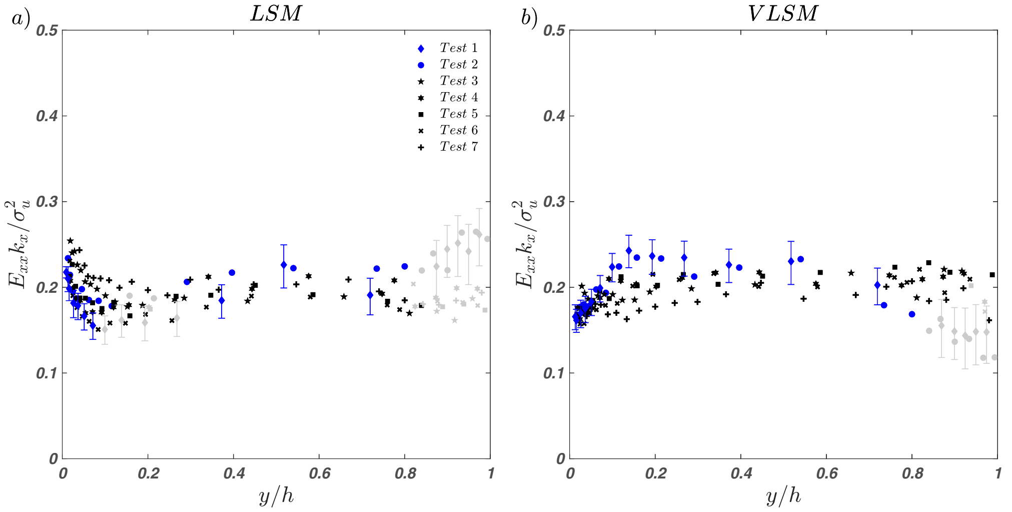

Fig. 2.21 (a) Spectral energy associated with LSM peaks normalized with σ_u^2; (b) spectral energy associated with VLSM peaks normalized with σ_u^2. The light grey markers have the same meaning as described in Fig. 2.19. The error bars indicate the confidence interval bounds (with a 95% confidence level).

argued that Re_τ-effects are more likely to dictate the stratification of data. This also agrees with results pertaining to canonical smooth-wall flows, where the Re_τ-dependence of the VLSM-peaks energy has already been extensively reported (Marusic et al., 2010; Smits et al., 2011).

However, a slightly different picture emerges when spectral energies are scaled with σ_u^2 (Fig. 2.21). This figure indicates that, despite some scatter, the energy associated with LSMs and VLSMs oscillates between the 15 and 25% of the total energy σ_u^2 (Fig. 2.21a–b).

Given the significant dependence of VLSMs wavelengths on the aspect ratio W/h (see Fig. 2.19), it comes natural to associate VLSMs with cellular secondary currents, normally observed in open-channel flows. These secondary flows are, indeed, known to be dictated in number, size and intensity by the aspect ratio W/h and whose topological resemblance to VLSMs has already been suggested by various authors, so much so one could speculate that secondary currents are the footprint of VLSMs on the mean-flow (Adrian and Marusic, 2012). Secondary currents can be described as cells of longitudinal vorticity whose height and width is approximately equal to the flow depth and whose intensity decreases with increasing distance from the lateral walls. In close proximity of such walls, secondary cells are somewhat split and their structure altered significantly due to the presence of corners (Nezu and Nakagawa, 1993; Rodríguez and García, 2008; Tominaga et al., 1989; Wang and Cheng, 2005).

On these premises, it becomes interesting to investigate the dependence of VLSMs' wavelengths (or wavenumbers) on the spanwise coordinate. Indeed, this is a way to test the response of VLSMs to variations in the structure and intensity of secondary currents, somewhat analogously to explore VLSMs' dependence on the aspect ratio W/h. This is precisely what was investigated in experiments 5a–5d (Tab. 2.3), whose results are reported in Fig. 2.22(a–h), where, each panel reports pre-multiplied spectra measured at a specific elevation from the bed and various locations along the spanwise coordinate. This figure indicates that for $y/h \geqslant 0.25$, the VLSM peak reduces in intensity and increases in wavenumber (i.e. reducing in wavelength) while approaching the lateral wall so much so in the proximity of the free-surface (i.e. $y/h = 0.98$, panel h) the VLSM peak occurs only in the central cross-section of the flow and disappears any closer to the lateral wall. This suggests that the lateral walls and,

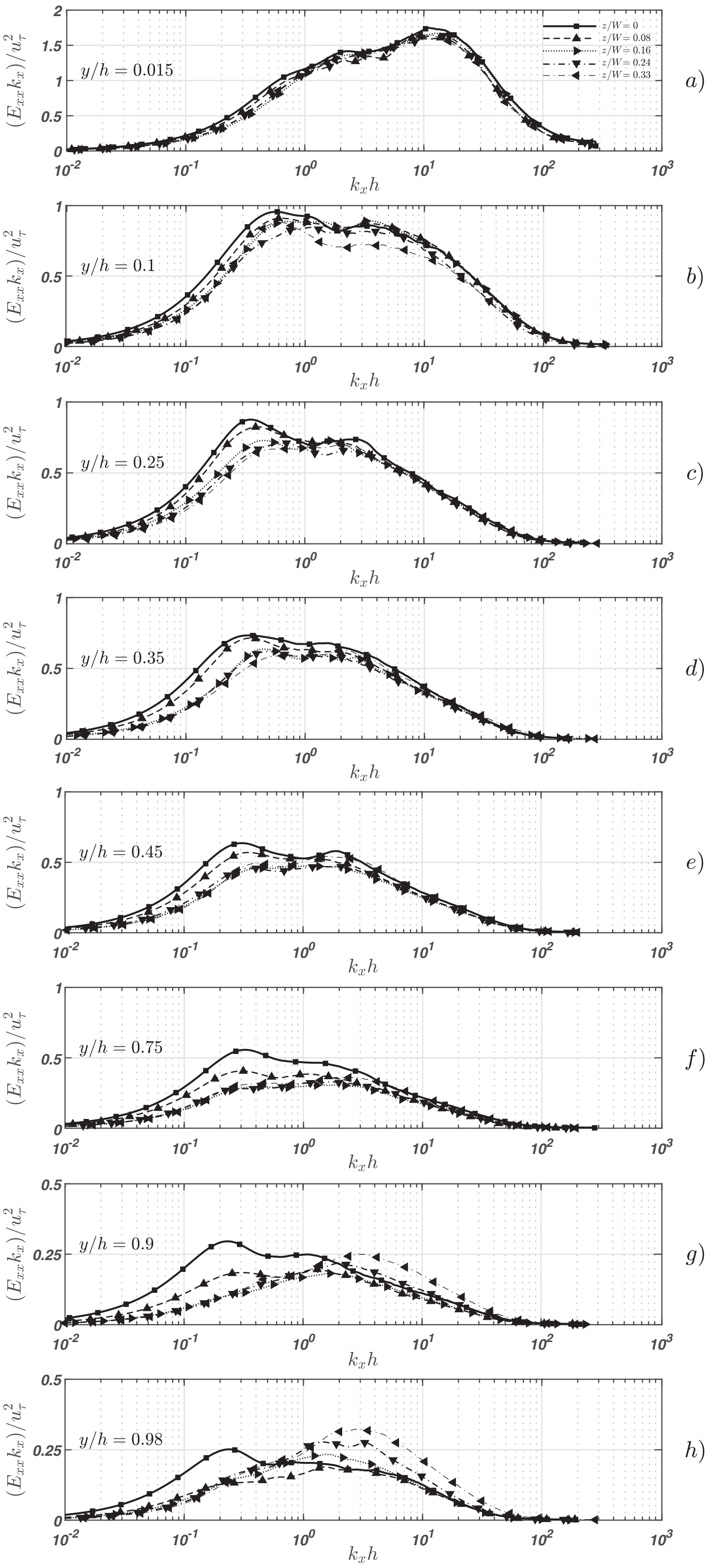

Fig. 2.22 Pre-multiplied 1-D spectra of the longitudinal velocity fluctuations for tests 5–5d at eight different outer locations. Test 5 was measured in the centreline of the flume, while tests 5a, 5b, 5c and 5d were measured at z/W = 0.08, 0.16, 0.24 and 0.33, respectively. Panels (a)–(h) refer to spectra measured at different bed-normal elevations y/h. Note the different y-axes limits of panels (a), (g) and (h) with respect to the others.

presumably the associated effects on the structure and intensity of secondary currents, alter VLSMs. Furthermore, these observations point towards the idea that the observed W/h effects on VLSMs might be mediated by variations that W/h imposes on the intensity and size of secondary currents.

Note that as per VLSMs, the LSM peak also decreases in intensity while approaching the lateral wall but is not altered in wavenumber (see, in particular panels c, d, e and f) until $y/h \geq 0.9$ (see panels g and h) where, however, spectra display peaks that are probably the signature of coherent structures developing within the side-wall boundary layer.

2.6 Conclusion

A dataset of velocity measurements was collected in non-uniform, smooth-bed, open-channel flows over a wide range of hydraulic conditions. In order to validate the experimental methodology and assess the quality of the experimental data, classical one-point statistics obtained from measurements taken mostly in the mid cross-section of the flume, were first computed and discussed against literature data pertaining to open-channel flows and other canonical wall-flows. Results revealed that, provided the aspect ratio of the flow is greater than 5, velocity-profiles resemble those reported in the literature on open-channel flows and other canonical flows. In contrast, flows with aspect ratio lower than 5 display velocity-statistics profiles that are significantly affected by the lateral walls. As one would expect, such effects were observed to increase with increasing distance from the bed and prevented data to collapse with those pertaining to high aspect-ratio experiments. This was particularly evident for the third and fourth order velocity statistics.

The key-results were obtained from spectral analysis of velocity time-series. Pre-multiplied 1-D spectra of the longitudinal velocity component revealed a double peak behaviour at wavenumbers consistent with those associated with LSMs and VLSMs, as observed in past studies on open-channel and canonical wall-flows. With respect to canonical wall-flows, three key differences were observed:

i) the double peak behaviour persists throughout most of the vertical extension of the flow domain, namely up to at least $y/h = 0.8$, while in canonical wall-flows it disappears beyond $y/\delta = 0.6$ at most (Monty et al., 2009);

ii) the VLSM-peak appears in pre-multiplied spectra for Re_τ as low as 725, whereas in canonical wall-flows much higher values are known to be required (Balakumar and Adrian, 2007; Hutchins and Marusic, 2007b; McKeon and Morrison, 2007);

iii) as argued by the recent study of Cameron et al. (2017) pertaining to uniform, rough-bed open-channel flows, these results confirm that the scaling of VLSMs-wavelengths is controlled by the aspect ratio W/h, as Re_τ and x/h effects were observed to be negligible. In particular, non-dimensional VLSM-wavelengths result to increase with increasing W/h. This work also confirms that LSM-wavelengths scale well with the outer length-scale of the flow, namely h.

For one hydraulic condition, vertical profiles of velocity time-series were measured not only in the mid cross-section of the flume, but also at various positions along the spanwise coordinate z/W. Results from spectral analysis indicated that the wavelength and magnitude of the VLSM-peaks were much more dependent on the spanwise coordinate, than wavelengths pertaining to LSM-peaks. It was argued that, since in open-channel flows the shape and intensity of secondary currents also vary across the spanwise extent of the channel, the dynamics of VLSMs and secondary currents might be closely linked, as suggested by Adrian and Marusic (2012).

Chapter 3

The influence of collinear gravity waves on turbulence in smooth-bed open-channel flows

This Chapter investigates how turbulence in open-channel flows is altered by the passage of collinear gravity waves. With the purpose of investigating a wide range of waves superimposed to the same current, new experiments were carried out with the same flume and LDA system that are described in the Chapter 2. Experimental data were used to compute mean velocity profiles, Reynolds stresses and 1-D spectra. Mean velocity profiles were obtained by time averaging the longitudinal velocity signal for each vertical elevation where data were sampled. Profiles of mean velocities clearly deviate from those of the current alone. However, it is here showed a possible theoretical explanation for which the mismatch is indicative of non-linear interactions between turbulence wave motions. By using the appropriate inner and outer length and velocity scales, an overlap layer in accordance with the classical asymptotic matching expansion theory is found for waves-current flows. The goodness of the outer length-scale herein proposed h_0 has both physical and experimental proofs. The Empirical Mode Decomposition (EMD) technique was employed to filter out the turbulence signal from velocity measurements. The filtered signal was then used to compute vertical profiles of second-order moments. In outer-scaling, the longitudinal turbulent intensity profiles result to be weakly affected by the wave motion, while the vertical turbulent intensity profiles are strongly reduced. This damping turns out to be tied to the strength of the wave vertical motion with respect to the current, i.e. $a\,f_w/u_{\tau_c}$ (where a is the wave amplitude, f_w is the wave frequency and u_{τ_c} is the current shear velocity). From the spectral analysis side, two interesting results come out: (i) as the wave strength increase, the VLSMs presence become increasingly blurred until they completely disappear; (ii) above h_0, a new spectral signature appears, associated with long turbulent structures (approximately 25 and 6 times the flow depth h). Here, it is hypothesised that these structures are associated to the passage of Langmuir-type cells, which produce new turbulence in the wave-dominated region of the flow (i.e. $y/h_0 > 1$, where y is the vertical coordinate). These Langmuir-type cells become more evident in the longitudinal 1-D pre-multiplied spectrum as the wave steepness increases.

3.1 Introduction

The wave-current interaction (WCI) is the engine behind many environmental, physical and biological processes of interest to oceanographers and engineers. For example, near the bottom the waves act as a stirring mechanism, reinforcing the entrainment of sediment particles by currents (Dyer and Soulsby, 1988; Madsen and Grant, 1976). The transport rate of seafloor sediments influences the formation and evolution of morphological patterns in the continental shelf and coastal region (Blondeaux, 2001; Charru et al., 2013). Besides sediment transport, flows resulting from wave-current interactions influence a plethora of ecologically-relevant processes. These include the pelagic larval dynamics and mortality, the feeding mechanisms of various biota, the nutrient uptake of planktonic microorganisms, and the mediation of dissolved substances such as oxygen and pollutants (Cowen and Sponaugle, 2009; de Souza Machado et al., 2016; Grant and Madsen, 1986; Guasto et al., 2012; Hannan, 1984; Huettel et al., 2014; Trowbridge and Lentz, 2018). For what concerns the engineering applications, the WCI is a key player in the power-output and the wake dynamics of hydro-kinetic marine turbines, the scour around marine and coastal structures, the navigation of ships near harbours and the erosion of salt marshes (Chamorro et al., 2015; Francalanci et al., 2013; Sumer, 2014; Sumer et al., 2013). Moreover, a deeper understanding of the WCI is fundamental to develop more reliable hydrodynamic models for coastal circulation. These models can be used to forecast coastal flooding and hence to improve the resilience of maritime cities against extreme events, which are now exacerbated by climate change (Hallegatte et al., 2013; Neumann et al., 2015).

Given the importance of the topic, many modelling and experimental studies in combined wave-current flows have been undertaken. On the modelling side, different analytical and numerical models of various complexity have been put forward in order to describe the WCI. A number of models have made use of the Reynolds-averaged Navier-Stokes (RANS) equations, whose closure is achieved by means of different methods, such as: the Prandtl's mixing-length model (Bakker and van Doorn, 1978; Bijker, 1967), time-invariant eddy-viscosity formulation (Christoffersen and Jonsson, 1985; Fernando et al., 2011b; Grant and Madsen, 1979, 1986; Huang and Mei, 2003; Humbyrd, 2012; Kim et al., 2001; Lundgren, 1972; Madsen, 1994; Myrhaug, 1984; Myrhaug and Slaattelid, 1990; Olabarrieta et al., 2010; Tambroni et al., 2015), time-varying eddy-viscosity formulation (Trowbridge and Madsen, 1984a,b) and two-equation models (Davies et al., 1988; Fredsøe et al., 1999; Holmedal et al., 2003; Zhang et al., 2014). Other modelling techniques have been used to investigate wave-current interaction, the most relevant being the momentum-defect model (Fredsøe, 1984), the Smoothed Particle Hydrodynamics (SPH) method (He et al., 2018), the lattice Boltzmann method (Cappietti, 2006) and the Generalized Lagrangian Mean (GLM) approach (Groeneweg and Battjes, 2003; Groeneweg and Klopman, 1998). Because of their main interest in sediment and scalar transport processes, most earlier models have focused on the effects of wave-current interactions at the bottom boundary layer in terms of mean velocity and bottom shear stress. However, as reported in Soulsby et al. (1993), among earlier models the predicted mean (τ_m) and maximum (τ_{max}) bed shear stress have discrepancies up to 30-40%. In these models, prevalently analytical, the mean velocity profile was obtained by dividing the water column in 2–3 layers based on the definition of rather arbitrary mixing lengths or eddy viscosity distributions and assuming that the vertical profile of the current followed the classical logarithmic law. Only in recent years efforts have been made to develop models that are able to characterise wave-current interactions across the whole water column (Huang and Mei, 2003; Olabarrieta et al., 2010;

Tambroni et al., 2015). As far as the mean velocity profile is concerned, these models perform fairly well as they successfully replicate experimental results.

Wave-current interaction has been studied extensively using different flume facilities (wave flume, wave basin, oscillatory water tunnel and oscillating bed). Here the focus is mainly directed on wave flumes where the waves are generated by paddles (or other oscillating mechanical elements) and currents imposed by a recirculating pump, as this is most relevant for the experimental set-up used herein. In general, different hydrodynamic and bottom surface conditions have been tested: waves and collinear current (Bakker and van Doorn, 1978; Brevik, 1980; Carstensen et al., 2010; George and Sleath, 1979; Kemp and Simons, 1982; Klopman, 1994; Lodahl et al., 1998; Mazumder and Ojha, 2007; Roy et al., 2017; Singh and Debnath, 2016; Umeyama, 2005, 2009b, 2011; van Doorn, 1981; van Hoften and Karaki, 1977; Yuan and Madsen, 2015; Zhang and Simons, 2019), waves against the current (Brevik, 1980; Cappietti, 2003; Kemp and Simons, 1983; Klopman, 1994; Roy et al., 2018; Umeyama, 2005, 2009b; Yuan and Madsen, 2015), superposition of bichromatic or random waves over a current (Klopman, 1994; Simons et al., 1994; Supharatid et al., 1993; Umeyama, 2009a; Yuan, 2016), waves and current crossing at an orthogonal direction (Andersen and Faraci, 2003; Bijker, 1967; Faraci et al., 2018; Fernando et al., 2011a; Musumeci et al., 2006; Simons et al., 1992; Visser, 1987), waves and current crossing at a generic angle (Arnskov et al., 1993; Lim and Madsen, 2016) and wave-current flowing over ripples (Brevik and Aas, 1980; Faraci et al., 2008; Fredsøe et al., 1999; Mathisen and Madsen, 1996a,b, 1999), mud bottom (An and Shibayama, 1994), macro-roughness elements (Barman et al., 2018; Singh et al., 2016) and macroalgal mats (Tambroni et al., 2016). Alongside these experimental works, field measurement campaigns within the inner region of the bottom boundary layer have been carried out (Drake and Cacchione, 1992; Hackett et al., 2011; Nayak et al., 2015). The results of these fieldworks are complementary to the experimental findings because, at the laboratory scale, it is impossible to adequately reproduce the large length and time scale separation that occurs between phenomena induced by wave motion and those induced by current.

In the aforementioned literature there is general consensus about the fact that the interaction between waves and currents is strongly non-linear. Indeed, linear superposition of the wave and current velocity fields does not provide

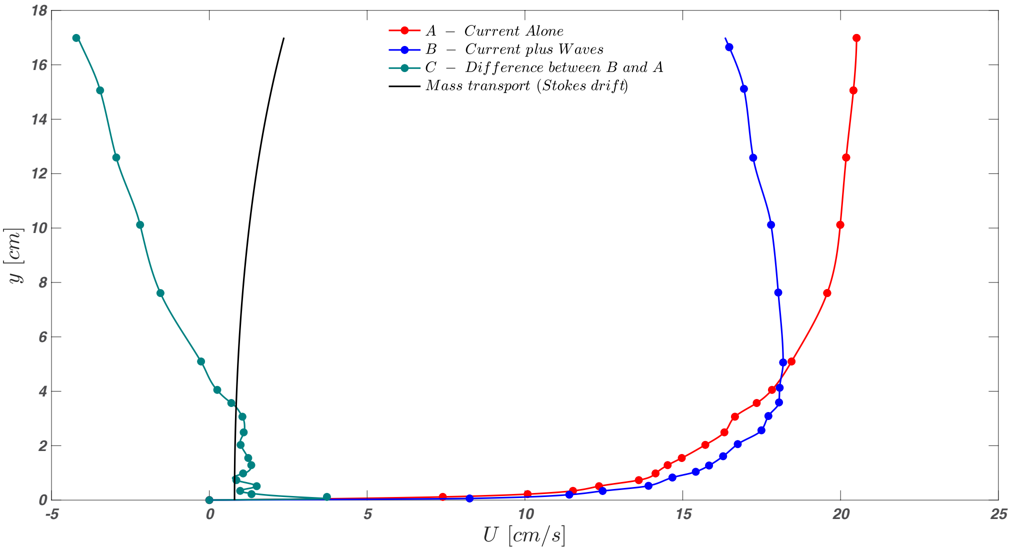

Fig. 3.1 Evidence of the non-linear interaction between waves and current (data from Kemp and Simons (1982), tests CA and WCA5, smooth bed and waves propagating with the current). The mean longitudinal velocity profiles are referred to the current alone case (A), the current plus waves case (B), and the difference between the profile B and A (C). The discrepancy of C with respect to the wave-induced net mass transport (determined with the Stoke drift formula, Eq. (3.1)) in the case of waves alone clearly indicates that the linear superposition does not hold.

the same velocity profiles that laboratory experiments yield. If the linear superposition was applicable, the difference between the measured longitudinal mean velocity profiles of current alone and waves plus current would match the wave mass transport profile, which can be estimated with the second-order Stokes drift velocity formula (Dean and Dalrymple, 1991):

$$U_S = \frac{H^2\,\omega\,k\,\cosh(2ky)}{2\,\sinh^2(kh)} \tag{3.1}$$

where H is the wave height, $\omega = 2\pi/T$ is the wave radial frequency, $T = 1/f_w$ is the wave period, f_w is the wave frequency, $k = 2\pi/L$ is the wave number, L is the wave length, h is the mean water depth and y is the vertical coordinate (with the zero level at the bottom). Fig. 3.1 shows that this is not the case (data are taken from the literature for one experiment only but the result is general).

The non-linearity of the WCI leads to the alteration of the mean velocity profiles with respect to the unperturbed open-channel flow (i.e. current alone).

In the case of waves superimposed to collinear current, the mean velocity increases near the bed and reduces in the outer layer. On the contrary, in the case of waves against the current, a decrease in the mean velocity occurs at the bed and an increase is observed near the free-surface.

The aforementioned aspect concerns the so-called bulk properties of the flow that, despite having practical relevance, reveal little about the mechanics of the turbulence in wave-current coexisting environments (Soulsby et al., 1993). Only in the recent years some works have explored how gravity waves alters the turbulence structure (Carstensen et al., 2010; Nayak et al., 2015; Roy et al., 2017; Singh and Debnath, 2016; Umeyama, 2005, 2009b; Zhang and Simons, 2019) by describing the change in the Reynolds stresses and/or turbulent intensities with respect to the case of current alone.

To assess the effects of gravity waves on the structure of turbulence, the turbulent and wave components of the signal need to be extracted from the raw signals and thus separated. In the relevant literature, the most common method to separate the signal components is the phase-average method (Franca and Brocchini, 2015), which is based on the triple decomposition firstly introduced by Hussain and Reynolds (1970) and divides the signal into mean, periodic (i.e. associated with waves), and turbulent components (see Section 3.2.3 for details). This method is very sensitive to the phase with which the periodic forcing acts (i.e. wave frequency) and if the phase is not precise it inevitably leads to leakages from the wave component to the turbulent component, with consequent overestimation of the latter. An alternative method was developed by Shaw and Trowbridge (2001) that utilises the velocity signals collected simultaneously by two sensors located at different elevations so that the correlation between the two signals is associated with the wave motion only – namely the sensors are located at a distance much larger than the integral scale of the vertical velocity fluctuations.

Notwithstanding the difficulties in filtering out the turbulent component of the signal, the findings reported in the literature are quite consistent, with the Reynolds stresses being dampened compared to the current alone case as a result of the WCI (Mazumder and Ojha, 2007; Roy et al., 2017; Singh and Debnath, 2016; Umeyama, 2005, 2009a,b; van Hoften and Karaki, 1977). Most references point out that the streamwise and wall-normal turbulent intensities rapidly increase moving upwards from the bed and reach the maximum near the bed for $y/h \approx 0.1$, at which point they both start decreasing. While the standard deviation $\sigma_{u'}$ of the longitudinal velocity shows a strong reduction in the outer layer, the standard deviation $\sigma_{v'}$ of the wall-normal velocity decreases more slowly throughout the water column. Furthermore, the profiles of the Reynolds shear stress $-\overline{u'v'}$ reach null values closer to the bed compared to the current alone case. Similar to findings in open-channel flow, near-wall coherent structures in the form of streamwise low- and high-speed streaks were observed also in wave-current flows (Carstensen et al., 2010; Zhang and Simons, 2019).

In hydraulically rough wall flows, both field measurements and laboratory experiments reveal an enhancement in the hydrodynamic roughness, estimated using the velocity profile, that is felt by the combined flow. This phenomenon, called apparent roughness, is particularly evident in those situations where the flow is in the wave dominated regime (i.e. the characteristic wave-induced velocity is similar or greater than the mean velocity of the current). This feature is fundamental to determine the effective shear stress that acts on the seabed in flows characterised by the presence of waves and currents.

Despite the rich literature on the topic, many questions regarding WCI await for an answer. Crucially, results are almost always presented in a dimensional fashion, namely with no appropriate scaling, thus it is unclear which are the relevant length, time, and velocity scales to be used to describe the problem. A comprehensive understanding of the turbulence structure would help untangling the complex effects of WCI. Unfortunately, the literature lacks accurate analyses of the structure of turbulence for currents perturbed by gravity waves.

In order to answer some open questions, in this study novel wave flume experiments were carried out to analyse the turbulence generated by waves propagating on a smooth-bed turbulent open-channel flow collinearly with the current. The wall-turbulence generated by the open-channel flow was used as benchmark and the alterations caused by the passage of waves with varying frequency and amplitude were characterised. The generated waves are in intermediate near-shallow water conditions and the aspect ratio is kept above 5 to minimise the effect of secondary cellular flows in the centreline of the flume. The knowledge gaps that are addressed in this study are summarised in the following, together with relevant information drawn from the results.

i) As far as mean velocity profiles are concerned, it is not clear, from a theoretical point of view, how non-linear wave-current interactions work to generate significant deviations from the current alone case. In Section 3.3.1 a plausible quantitative explanation is provided.

ii) The studies available in the literature rarely provide detailed information about the regularity of the waves that were generated in the flumes and hence about the real forcing used to perturb currents. Further, most experiments were carried out at aspect ratios (i.e. the ratio between the channel width and the flow depth) lower than 5, value that Nezu and Nakagawa (1993) indicated as the threshold below which the secondary cellular flows (Prandtl's secondary flows of the second kind) start to affect turbulent properties also in the mid-section of the channel. This aspect dramatically impacts the behaviour of large-scale structures in smooth-bed open-channel flow (as evidenced in Chapter 2). Moreover, only a few works have analysed waves close to the shallow water conditions, where the wave orbital motion reaches the near-wall part of the flow and strongly interacts with the current boundary layer.

iii) A universal method to separate the turbulence and wave signals from velocity measurements that can be used in both laboratory and field conditions does not exist. In Section 3.2.3 a novel application of the so-called Empirical Mode Decomposition (EMD) is proposed to discern the turbulent signal from the waves generated in the flume which did show a level of irregularity, despite the controlled conditions.

iv) Most results from the literature focus on bulk properties such as mean velocities and bottom shear stress, while little is known about turbulence properties and how the passage of waves alters the structure of turbulence with respect to the undisturbed current case. Section 3.3.2 contains a discussion about the behaviour of the second-order moments, which, in accordance with the literature, seem to be dampened by the passage of waves. The Reynolds shear stresses are discussed further through the lens of the quadrant analysis in Section 3.3.3. By means of spectral analysis of velocity signals, Section 3.3.4 reports on the scales of turbulence that are most affected by waves. This is yet another aspect that has been largely overlooked in the literature, where the fate of the so-called Large-Scale and

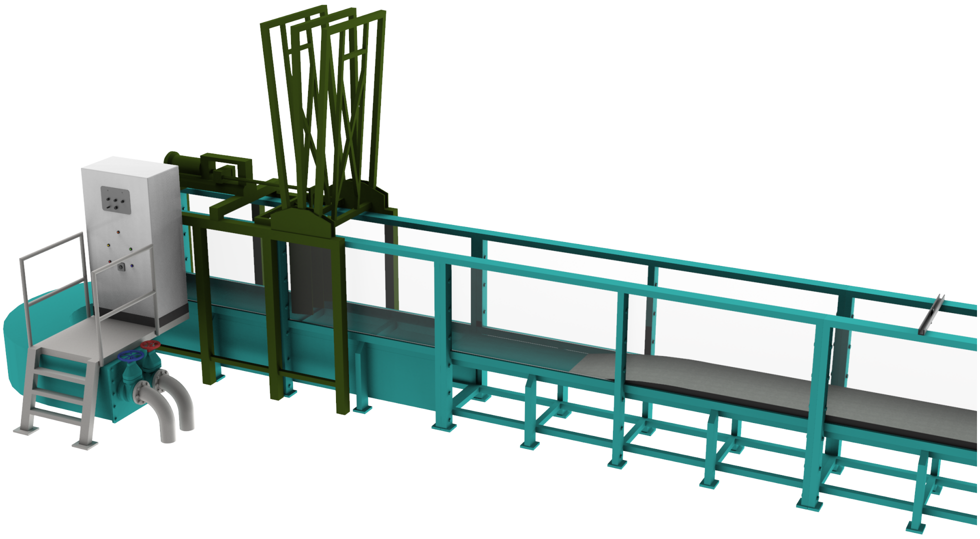

Fig. 3.2 Detail of the flume inlet with the piston-type wavemaker (dark green) and the concrete bottom with the steel ramp (dark grey).

Very-Large-Scale Motions (LSMs and VLSMs) in an open-channel flow with the superimposition of gravity waves has never been investigated.

3.2 Methodology

The experiments were carried out in the same flume facility and with the same setup and instrumentation as those described in Section 2.2. For these reasons, in the following, only the differences with respect to Section 2.2 are reported.

3.2.1 Equipment and hydraulic conditions

The open-channel flume used for the experiments (Fig. 2.6a) allows for the generation of progressive gravity waves by means of a piston-type wavemaker placed in proximity of the flume inlet (Fig. 3.2). The wavemaker is controlled through an ad hoc LabVIEW program and the waves generated within the flume can reach a maximum height of 0.3 m and have a wave period that spans between 0.2 and 6 s. Both regular and irregular waves can be reproduced. The channel outlet can be sealed with a steel cap in order to obtain a water basin in quiescent conditions where pure wave motion can be studied. In those circumstances, just before the outlet, a 2.2 m long porous steel passive wave absorber is installed to prevent wave reflections within the channel. The wave absorber has a parabolic profile with a porosity of 50% and a reflection coefficient K_r ranging from 0.06 to 0.09 (i.e. absorbing 91–94% of the incoming wave energy) for the wave conditions studied in the following (see Tab. 3.1). The reflection coefficient is define as $K_r = H_r/H_i$, i.e. ratio of the reflected wave height (H_r) to the incident wave height (H_i) and was estimated involving a simplified version of the two fixed probes Goda and Suzuki (1976) method (Isaacson, 1991). Three different type of experiments were carried out: waves alone, current alone and waves following a current.

The wave alone experiments were used to study the characteristics of the waves generated with the adopted setup (i.e. steel ramp and concrete blocks, Fig. 2.6b and Fig. 3.2) and they allowed to determine the transfer function of the wavemaker (i.e. the function used to determine actual wave characteristics from imposed oscillatory motion of the wavemaker). Setting a water depth $h = 0.12$ m, the evolution of the wave free-surface was measured through five ultrasonic gauges (sampling frequency f_s equal to 100 Hz) displaced along the flume. In particular, the five gauges were located at a normalised distance x/h from the inlet of 25.8, 175.8, 225.8, 256 and 331, respectively (Fig. 3.3). Ultrasonic gauges have comparable performance in the measurement of the wave surface characteristics with respect to others instrumentations, i.e. resistive or pressure sensors (Marino et al., 2018). In addition, at the test section (located at $x = 30$ m from the origin of the x coordinate, see Fig. 2.6b), a digital camera (Canon EOS 550D) was installed next to the flume side wall to capture the water surface profile. The camera was used in continuous shooting mode with 3.7 frames per second. The image sensor type is 22.3 x 14.9 mm CMOS with approximatively 18.7 megapixels. The ISO sensitivity range is 100–6400, the exposure time range is 30–1/4000 s while the diaphragm number range is f/1–f/64. The camera was placed on a tripod and the distance between the camera and the side glass-wall was 3 m.

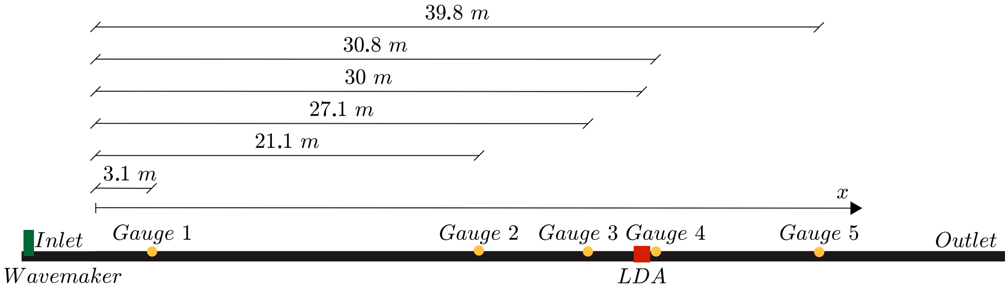

Fig. 3.3 Sketch of the ultrasonic gauges (orange circle) and LDA (red square) locations along the open-channel flume.

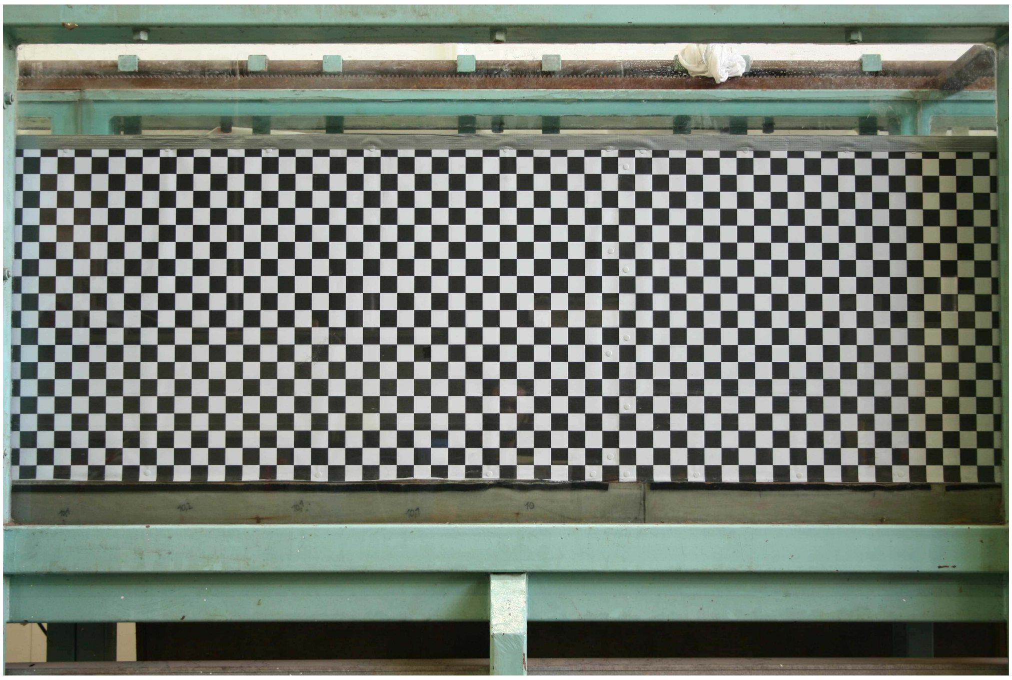

Fig. 3.4 Image of the checkerboard pattern fixed to the side glass wall of the open-channel flume at the test section.

The camera calibration method and analysing procedure was exactly the same as reported in Melis et al. (2019). Briefly, the camera calibration was performed with the MATALB toolbox Single Camera Calibrator App, which calculates extrinsic and intrinsic parameters and lens distortions. For the calibration, a rectangular checkerboard panel was located on the side of the test section (Fig. 3.4) and 23 photos of it were taken so that the algorithm could calculate all relevant parameters accurately. These photos were shot from different positions by moving the tripod, making sure to always frame the whole checkerboard. In addition, the software locates the checkerboard intersection points and provides a matrix with their point coordinates. Based on the camera parameters calculated and the position of the intersection points, images can be converted from pixel to metric coordinates. The mean error associated with the calibration was 0.76 pixel (that corresponds roughly to 0.4 mm).

After the camera calibration was completed, photos of the surface waves could be acquired. In order to obtain a clear water surface identification in the photos, the study area was backlit with two LED panels. In addition, the water was mixed with Rhodamine dye (see Fig. 3.6a in Section 3.2.2).

The wave plus current experiments were carried out first by setting the current alone as described in Sections 2.2–2.3 of Chapter 2 and then by setting off the wavemaker. Test 3 (see Tab. 2.3) was used as the current alone test.

Hereafter, the following abbreviations are adopted: CA for current alone, WA for waves alone and WC for waves plus current.

Tab. 3.1 reports the experimental hydraulic conditions for the WA cases. The parameters h, a, H and L (mean flow depth, wave amplitude, wave height and wave length, respectively) were determined from the free-water surface measurements of the ultrasonic gauge placed in proximity to the LDA system. The measurements lasted 200 s each to have an adequate number of waves passing under the gauge and, at the same time, not to be affected by the reflection from the wave absorber. However, the wave parameters were calculated as the mean of 20 wave cycles for test WA−T1, 30 wave cycles for test WA−T2 and 40 wave cycles for tests WA−T3 to WA−T5 in order not to consider the reflection effects (Tab. 3.1). Also the f_w (T) values were checked

Run	h **[m]**	f_w **[Hz]**	T **[s]**	a **[m]**	H **[m]**	L **[m]**	h/L	ϵ	H/h	U_R
WA−T1	0.12	0.50	2.00	0.005	0.01	2.30	0.052	0.014	0.083	30.6
WA−T2	0.12	0.75	1.33	0.005	0.01	1.40	0.085	0.022	0.083	11.3
WA−T3	0.12	1.00	1.00	0.005	0.01	1.00	0.120	0.031	0.083	5.8
WA−T4	0.12	1.00	1.00	0.010	0.02	1.00	0.120	0.063	0.166	11.6
WA−T5	0.12	1.00	1.00	0.015	0.03	1.00	0.120	0.094	0.250	17.4

Table 3.1 Summary of the hydraulic conditions for the waves alone (WA) cases. The columns indicate, respectively: the mean water depth h; the wave frequency f_w; the wave period $T = 1/f_w$; the characteristic wave amplitude a; the characteristic wave height $H = 2a$; the characteristic wave length L; the relative depth h/L; the wave steepness $\epsilon = ak$, where $k = 2\pi/L$ is the wave number; the relative height H/h and the Ursell number $U_R = HL^2/h^3$.

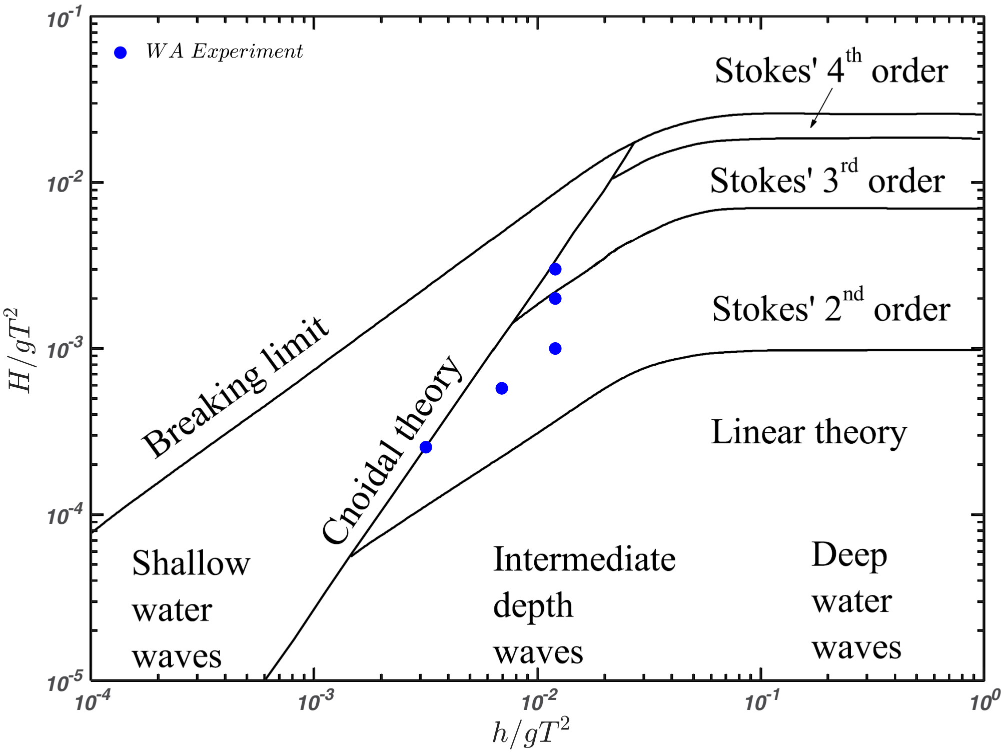

Fig. 3.5 Range of applicability of the different wave theories (adapted from Qi et al., 2019). The blue markers indicate the WA experiments reported in Tab. 3.1.

Run	h **[m]**	u_τ **[m/s]**	U_b $\pitchfork$ **[m/s]**	f_w **[Hz]**	a ‡ **[m]**	L ‡ **[m]**	A_b † **[m]**	U_w † **[m/s]**	Re_b	RE	k_s/A_b	U_b/U_w	**Symbol**
CA	0.12	0.00755	0.1517	–	–	–	–	–	14400	–	–	–	○
WC–T1	0.12	0.00776	0.1517	0.50	0.005	2.30	0.0138	0.0432	14400	656	0.018	3.51	○
WC–T2	0.12	0.00821	0.1517	0.75	0.005	1.40	0.0087	0.0410	14400	393	0.028	3.70	○
WC–T3	0.12	0.00849	0.1517	1.00	0.005	1.00	0.0060	0.0378	14400	250	0.041	4.01	○
WC–T4	0.12	0.00822	0.1517	1.00	0.010	1.00	0.0120	0.0755	14400	1001	0.021	2.01	◇
WC–T5	0.12	0.00794	0.1517	1.00	0.015	1.00	0.0180	0.1133	14400	2252	0.014	1.34	□

Table 3.2 Summary of the hydraulic conditions for the current alone (CA) and waves plus current (WC) cases. The columns indicate, respectively: the mean water depth h; the shear velocity u_τ; the current bulk velocity U_b; the wave frequency f_w; the characteristic wave amplitude $a = H/2$, where H is the wave height; the characteristic wave length L; the longitudinal water particle semi-excursion due to the orbital motion at the bottom A_b; the longitudinal wave orbital velocity at the bottom U_w; the current bulk Reynolds number $Re_b = R_h U_b/\nu$, where R_h is the hydraulic radius and ν is the kinematic viscosity of the water; the wave Reynolds number $RE = A_b^2\omega/\nu$, where $\omega = 2\pi f_w$ is the radial frequency; and the k_s/A_b relative roughness, where k_s is the Nikuradse equivalent sand roughness. Note that the symbol $\pitchfork$ denotes values determined in the current alone case (CA, see Tab. 2.3); the symbol ‡ denotes values determined in the waves alone case (WA, see Tab. 3.1); the symbol † denotes values calculated by using the Airy linear wave theory (Dean and Dalrymple, 1991).

with the water-surface measurements, and the discrepancy between them and the wavemaker frequency inputs was found to be negligible.

Based on the values of the relative depth h/L, it can be inferred that all waves are in the intermediate water conditions, as the shallow water and deep water limits are $h/L < 0.05$ and $h/L > 0.5$, respectively (Dean and Dalrymple, 1991). This indicates that the orbital wave motion is able to reach the channel bottom, although the horizontal excursion of the water particle changes along the y coordinate. The values of the wave steepness ϵ and the relative height H/h indicate no wave breaking conditions (the limit beyond which waves start to break is $\epsilon \approx 0.442$ and $H/h \approx 0.8$, respectively, see Fredsøe and Deigaard, 1992). Also from the analysis of the images no breaking waves are revealed.

The wave steepness, combined with the Ursell number ($U_R = HL^2/h^3$), can be used to delineate regions of validity for the various analytical wave theories (Hedges, 1995). In relatively shallow water, the suitability of a particular theory to describe wave conditions mainly depends on the magnitude of U_R, whereas in deep water, the suitability mainly depends on the wave steepness. Hedges (1995) indicates that the cnoidal wave theory is appropriate when $U_R \gtrsim 40$, while for values of $U_R \lesssim 40$ and $\epsilon \lesssim 0.125$, the Airy or Stokes' II order wave theories are more suitable. To counter-test this, the triplet h, H and T can be used, instead of h, H and L, to define the ranges of wave theories applicability. These ranges are shown in Fig. 3.5 together with the corresponding H/gT^2 and h/gT^2 for the experiments reported in Tab. 3.1. From Fig. 3.5, it is noticeable that most cases fall into the Stokes II order wave theory region.

Tab. 3.2 lists the experimental hydraulic conditions for the CA and WC cases, which represent the core of this Chapter. The velocity in the WC experiments was measured with the LDA in coincidence and non-coincidence mode. In coincidence mode, the measurements were taken over 15 different positions along the vertical coordinate for each test and 1000 wave cycles were measured at each position with a sampling frequency f_s ranging between 50 Hz and 100 Hz. In addition, the velocity was measured at six selected positions in the non-coincidence mode for both the u and v components for reaching a more elevate sampling frequency (that enables resolving a larger portion of the turbulent spectrum) and collecting a larger amount of data points to compute reasonably smooth spectra. These measurements lasted at least 45 minutes each and the f_s varied between 150 Hz and 300 Hz, depending on the hydraulic conditions. Furthermore, similarly to the CA case, 30-minutes long time-series of the free-water surface were recorded by means of the ultrasonic gauges.

For all the experiments, the Froude number Fr of the current was 0.14 and the aspect ratio W/h (i.e. the ratio between the channel width W and the water depth h) was equal to 5.08 so that flow conditions at the mid cross section of the channel could be considered not affected by lateral walls (Nezu and Nakagawa, 1993).

The shear velocities u_τ reported in Tab. 3.2 comprehend both the shear velocity of the CA case (u_{τ_c}) and the shear velocities for the wave plus current cases ($u_{\tau_{wc}}$). For the former, more details can be found in Section. 2.4, while the latter were estimated through the classical Clauser method (Clauser, 1956) and more details will be given in Section. 3.3.1.

The Airy linear wave theory (Dean and Dalrymple, 1991) allows one to estimate the longitudinal water particle semi-excursion A_b and the longitudinal wave orbital velocity U_b at the bottom, by means of which the waves orbital motion can be classified, i.e.:

$$A_b = \frac{H}{2\,\sinh(kh)} \tag{3.2}$$

$$U_w = \omega\, A_b \tag{3.3}$$

where $k = 2\pi/L$ is the wave number and $\omega = 2\pi/T$ is the wave radial frequency. The use of the Airy theory for wave velocity estimation is widely adopted. Previous studies concluded that such theory gives a good approximation of the orbital velocity at the seabed under the wave crest (Kirkgöz, 1986; Soulsby, 2006) and may predict satisfactorily the wave properties over a wider region than that shown in Fig. 3.5 (Grace, 1978; Hedges, 1995).

The wave Reynolds number $RE = A_b^2\omega/\nu$ was calculated from the values of A_b. The values of RE reported in Tab. 3.2, together with the relative roughness k_s/A_b (where k_s is the Nikuradse equivalent sand roughness, equal to 0.25 mm for the concrete bottom used in this work), indicate whether the wave boundary layers were laminar (WA–T2 and WA–T3) or transitional (WA–T1, WA–T4 and WA–T5), following the classification described in Blondeaux (1987). Based on the values of the current Re_b and wave Reynolds number RE (Lodahl et al., 1998), the resulting combined boundary layers were turbulent for all cases considered. Finally, the ratio between the characteristic current velocity and the wave velocity U_b/U_w indicates that all the tests were in the so-called current dominated regime.

3.2.2 Waves characterisation

The aim of this Section is to assess the properties and regularity of the waves (WA) generated by the wavemaker within the open-channel flume and then to quantify their alteration in the combined case (WC). Both ultrasonic free-surface measurements and image processing were used to study the waves alone experiments, in order to check the applicability of standard theories.

Test WA–T2 is used as representative example for the WA experiments because the other tests showed analogue features. It is important to clarify that only wave cycles before the insurgence of reflection effects were considered for the characterisation.

In Fig. 3.6(a–b) photo of the waves generated within the flume and the free-surface profile extracted using the image processing described Section 3.2 are displayed. The photographed wave in Fig. 3.6(a) has slightly greater wave parameters than those obtained from the free-surface measurements of the ultrasonic gauges (Tab. 3.1), indeed it has $a = 0.006$ m and $L = 1.44$ m. The extracted free-surface profile η is compared with the profiles predicted by Airy η_A and Stokes II order η_{II} theory (Dean and Dalrymple, 1991), i.e.:

$$\eta_A = \frac{H}{2}\cos(kx - \omega t) \tag{3.4}$$

$$\eta_{II} = \frac{H}{2}\cos(kx - \omega t) + \frac{H^2 k}{16}\frac{\cosh(kh)}{\sinh^3(kh)}(2 + \cosh(2kh))\cos 2(kx - \omega t) \tag{3.5}$$

where t is the time. Comparing the free-surface profiles in Fig. 3.6(b) there is no substantial difference between η_A and η_{II}. The wave length is

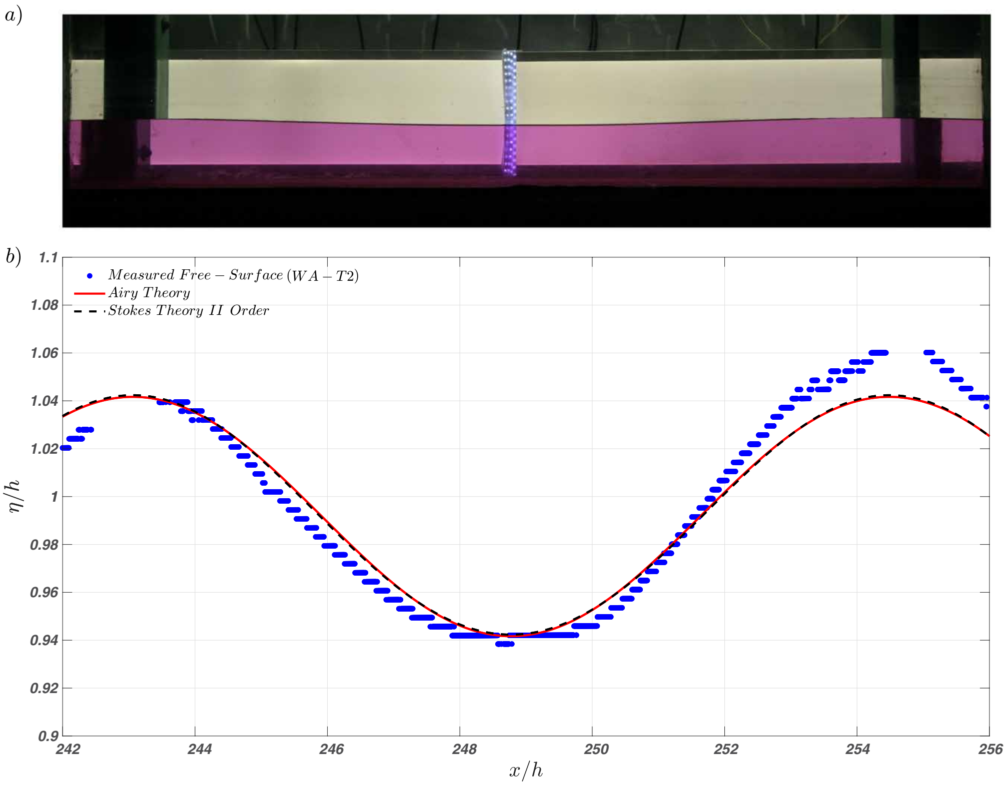

Fig. 3.6 (a) Photo of the surface wave profile (case WA−T2); (b) spatial evolution of the surface wave profile for WA−T2. The blue markers represent the free-surface extracted by the image processing. The red solid line represents the Airy linear theory, while the black dashed line represents the Stokes II order theory.

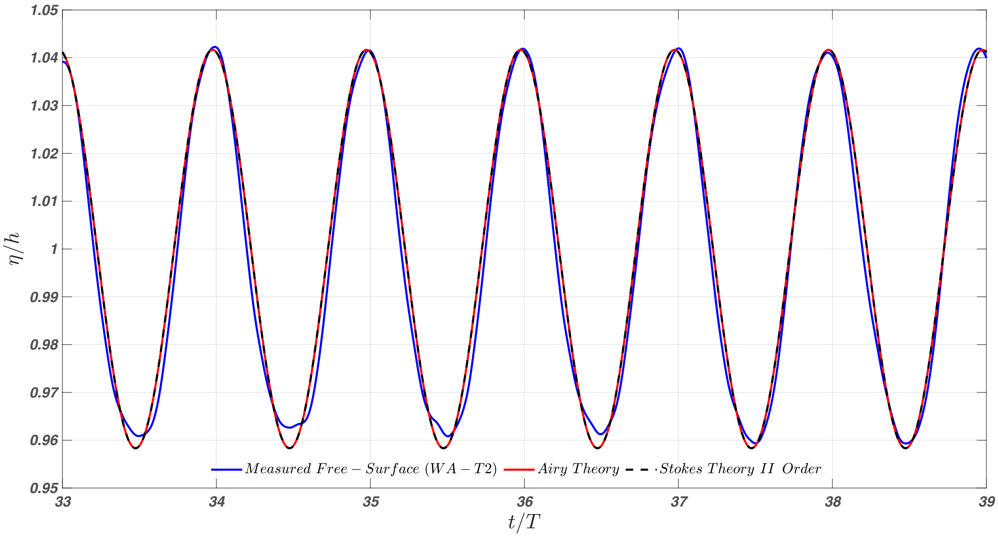

Fig. 3.7 Temporal evolution of the surface wave profile for WA−T2. The blue solid line represents the free-surface measured from the ultrasonic gauge in proximity to the LDA location. The red solid line represents the Airy linear theory, while the black dashed line represents the Stokes II order theory.

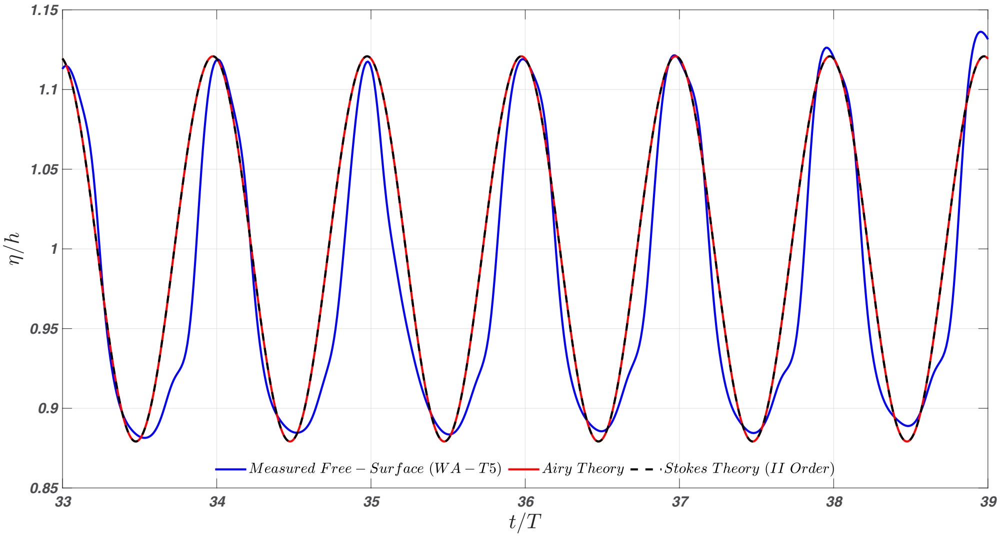

Fig. 3.8 Temporal evolution of the surface wave profile for WA−T5. The blue solid line represents the free-surface measured from the ultrasonic gauge in proximity to the LDA location. The red solid line represents the Airy linear theory, while the black dashed line represents the Stokes II order theory.

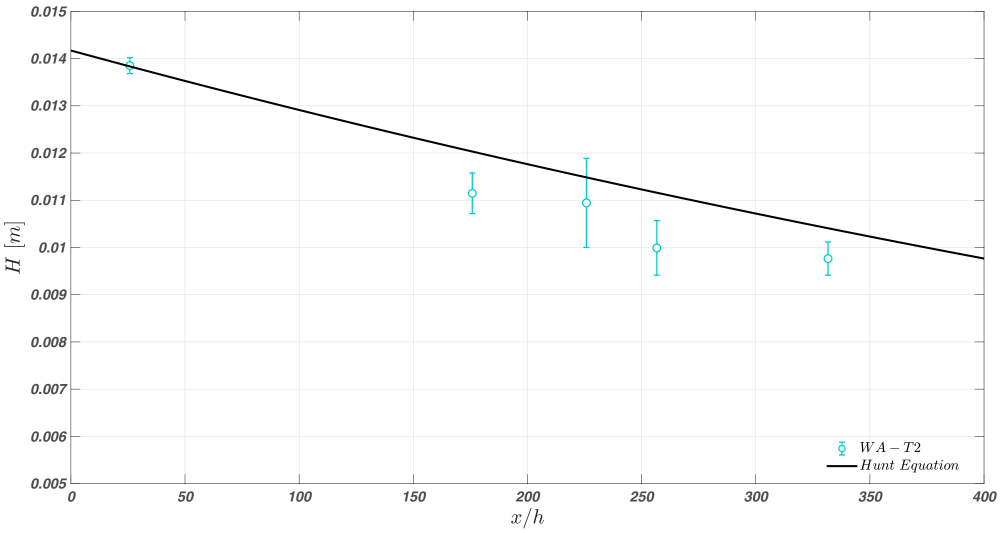

Fig. 3.9 Wave attenuation along the flume. The black solid line represents the equation (Eq. (3.7)) introduced by Hunt (1952). In particular, the markers represent mean values and the bars are twice the standard deviation.

perfectly reconstructed by the theoretical profile. The discrepancy between the theoretical and real amplitudes is of the same order of magnitude as the amplitude standard deviation ($\pm\eta/h = 0.008$) obtained from the measurements of the ultrasonic gauge placed at $x/h = 256$.

The analysis of the temporal evolution of the free-surface allows comparing multiple waves and leads to similar conclusions (Fig. 3.7). Although a slight variation in the wave troughs can be noticed, it is of the same order of magnitude as the ultrasonic gauge measurement uncertainty. Therefore, the agreement between the theory and the measurements is satisfactory. Similarly, considering the more nonlinear case WA−T5 reported in Fig. 3.8, the linear theory well mimics both wave height and length, even if the shape results to be somehow distorted. It follows that the Airy theory can be reasonably well applied to describe the wave surface characteristics for the WA tests.

For evaluating the wave attenuation along the flume, the wave height values are compared with the analytical result of Hunt (1952). The results of the wave attenuation analysis for test WA−T2 along the flume are shown in Fig. 3.9. Hunt (1952) defined the wave attenuation modulus α as:

$$\alpha = \frac{2\,k}{W}\sqrt{\frac{\nu}{2\,\omega}}\left(\frac{k\,W + \sinh(2kh)}{2\,k\,h + \sinh(2kh)}\right) \tag{3.6}$$

thus, the wave height along the flume can be estimated as:

$$H = H_0\,\exp(-\alpha x) \tag{3.7}$$

where H_0 is an initial-value. Here, H_0 was taken equal to the wave height measured at the first ultrasonic gauge. From Fig. 3.9 it can be seen that Eqs. (3.6)–(3.7) underestimate the wave attenuation along the flume, as already reported in previous studies (Grosch et al., 1960; van Hoften and Karaki, 1977). However, it is important to note that the experiments follow the trend indicated by Hunt (1952) reasonably well.

The results displayed in Figs. 3.6–3.9 show that the flume adequately reproduce progressive waves behaviour in intermediate water conditions. Furthermore, the standard theories describe the wave surface properties satisfactorily.

For the waves plus current experiments, the mean ($\overline{T}$ and $\overline{H}$), standard deviation (T_{sd} and H_{sd}) and coefficient of variation (CV_T and CV_H) of T and H recorded at each ultrasonic gauge are reported in Tab. 3.3. It can be seen that, while the wave period was not affected by the presence of the current, the wave height was altered considerably. Both the standard deviation and the coefficient of variation of the wave height are higher in these cases than for the wave alone cases (compare the standard deviation values for test WC−T2 in Tab. 3.3 with those reported for test WA−T2 in Fig. 3.9). Furthermore, the standard deviation and the coefficient of variation of H increase sensibly along the channel length. To allow for a visual comparison, the coefficient of variation of the wave period $CV_T = T_{sd}/\overline{T}$ and height $CV_H = H_{sd}/\overline{H}$ are plotted in Fig. 3.10(a–b) for all WC tests. While the values of CV_T are bounded between 0 and 0.1 with no obvious trend, indicating that values are close to the average, the values of CV_H are more spread and show an increase as the waves move along the channel.

Fig. 3.11 reports the normalised histogram of the wave heights similarly to the approach used by Goda (2010). The ordinate is the probability distribution defined as:

Gauge		WC–T1	WC–T2	WC–T3	WC–T4	WC–T5
Gauge 1	$\overline{T}$	2.001	1.333	0.999	0.999	1.000
	T_{sd}	0.083	0.034	0.022	0.025	0.059
	CV_T	0.041	0.025	0.022	0.025	0.059
	$\overline{H}$	1.045	1.145	1.199	2.334	3.434
	H_{sd}	0.080	0.133	0.194	0.331	0.409
	CV_H	0.076	0.116	0.161	0.142	0.119
Gauge 2	$\overline{T}$	2.000	1.333	1.000	1.000	1.000
	T_{sd}	0.092	0.052	0.044	0.031	0.050
	CV_T	0.046	0.039	0.044	0.031	0.050
	$\overline{H}$	0.935	1.206	1.041	2.187	2.919
	H_{sd}	0.122	0.141	0.216	0.329	0.541
	CV_H	0.130	0.117	0.207	0.150	0.185
Gauge 3	$\overline{T}$	2.000	1.333	0.989	0.998	0.999
	T_{sd}	0.074	0.061	0.045	0.040	0.058
	CV_T	0.037	0.045	0.045	0.040	0.058
	$\overline{H}$	0.915	0.891	1.075	1.607	2.746
	H_{sd}	0.140	0.188	0.249	0.423	0.628
	CV_H	0.153	0.211	0.231	0.263	0.228
Gauge 4	$\overline{T}$	2.000	1.333	1.000	0.999	1.000
	T_{sd}	0.099	0.078	0.049	0.052	0.086
	CV_T	0.049	0.058	0.049	0.052	0.086
	$\overline{H}$	0.803	1.009	1.059	2.091	2.897
	H_{sd}	0.105	0.218	0.259	0.375	0.524
	CV_H	0.131	0.216	0.244	0.179	0.181
Gauge 5	$\overline{T}$	2.000	1.333	1.000	1.000	1.005
	T_{sd}	0.089	0.0781	0.060	0.056	0.064
	CV_T	0.044	0.058	0.060	0.056	0.063
	$\overline{H}$	0.990	0.735	0.844	1.740	2.434
	H_{sd}	0.111	0.213	0.299	0.465	0.639
	CV_H	0.112	0.289	0.354	0.267	0.262

Table 3.3 Statistics of the surface waves in the case of waves plus current: $\overline{T}$ is the mean period; T_{sd} is the period standard deviation; $CV_T = T_{sd}/\overline{T}$ is the period coefficient of variation; $\overline{H}$ is the mean wave height; H_{sd} is the wave height standard deviation and $CV_H = H_{sd}/\overline{H}$ is the wave height coefficient of variation. The values of $\overline{T}$ and T_{sd} are in seconds, while the values of $\overline{H}$ and H_{sd} are in centimetres.

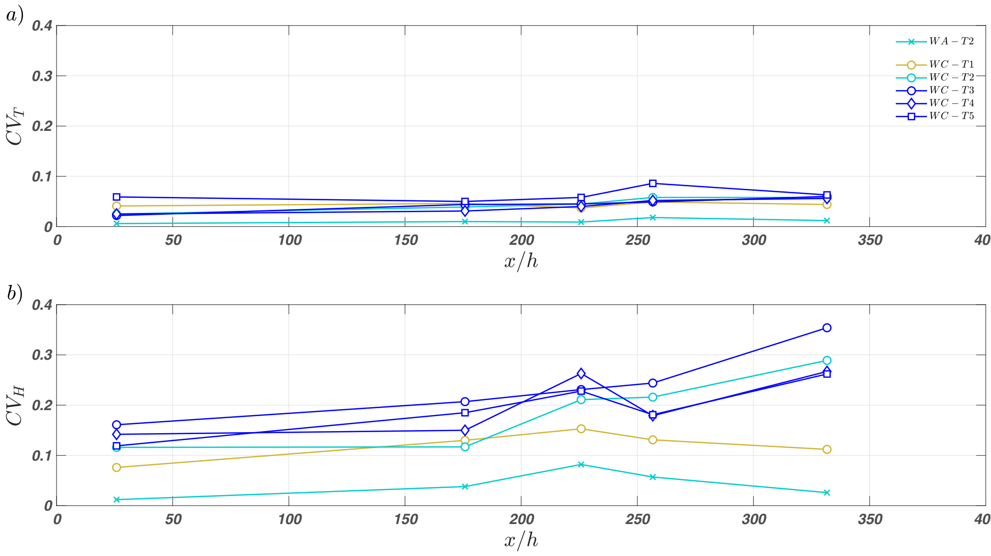

Fig. 3.10 Coefficient of variation of (a) the wave period, and (b) the wave height. Alongside the WC tests, also the representative WA−2 test is reported for comparison.

$$p(H/\overline{H}) = \frac{n}{N_0\Delta} \tag{3.8}$$

where n and Δ are the number of waves in a specific histogram bin and the width of the histogram bin, respectively, and N_0 is the total number of recorded wave heights. In Fig. 3.11 the first column reports the distributions at the first ultrasonic gauge, while the second column reports the distributions at the fourth ultrasonic gauge (namely the probe next to the LDA system). All the experiments show a flattening of the distribution moving from the first to the fourth gauge which is particularly marked in WC−T2 and WC−T3.

In addition to the flattening of the distribution, the increase in the wave height variability caused the wrinkling of the water surface. Even though the amplitude of these disturbances was always smaller than the ultrasonic gauges sampling error, their presence is clearly visible in the frequency spectrum domain (Fig. 3.12a–b). Fig. 3.12(a–b) reports the frequency spectrum $E(f)$ of the free-water surface for test WC−T5, which represented the worst case scenario in terms of water surface disturbances. The period of the occurring perturbations was lower than the wave one because they were usually located between two consecutive wave crests. The small peak in Fig. 3.12(a) has a frequency of ≈ 2 Hz and should be associated with these perturbations, while

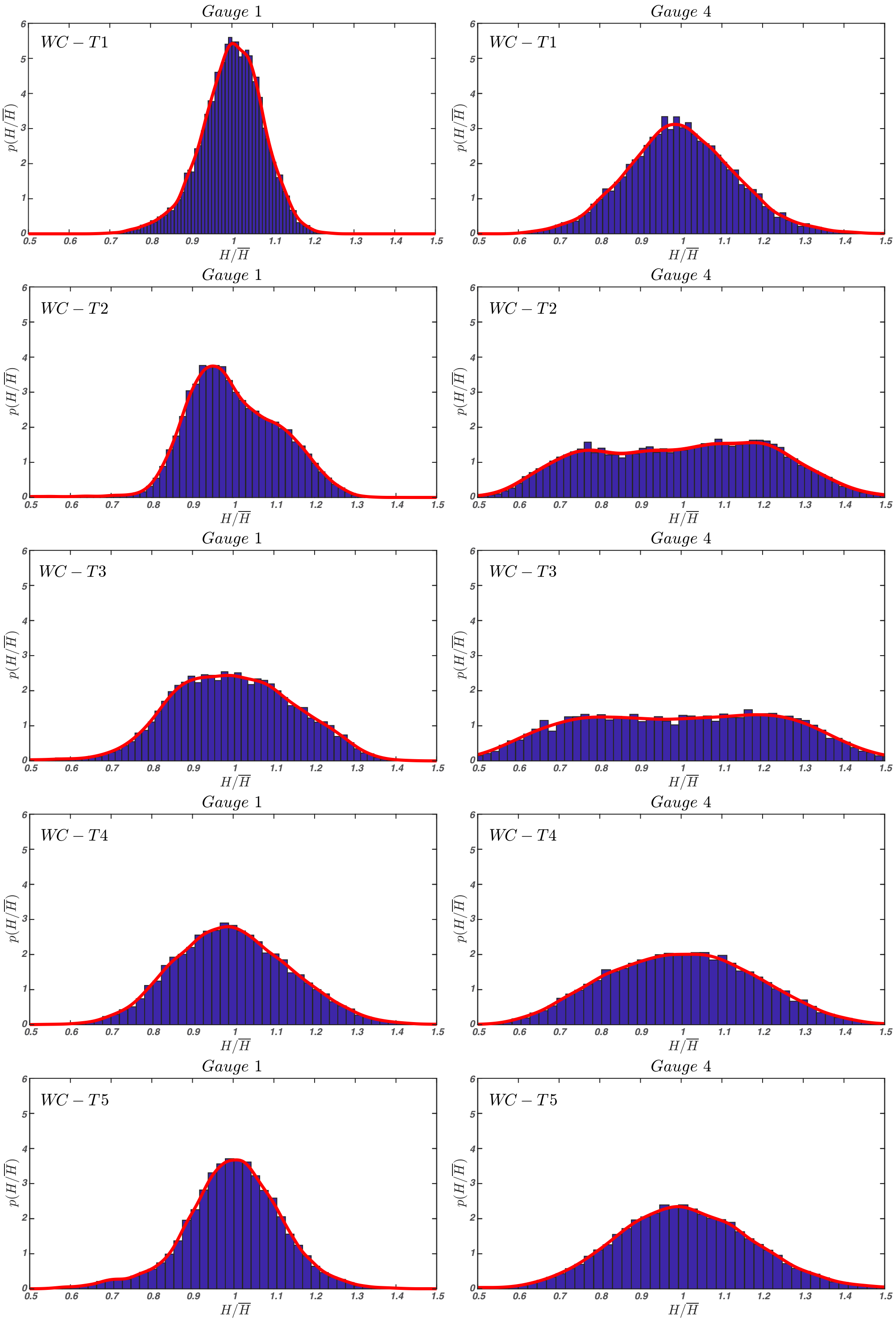

Fig. 3.11 Normalised histograms and relative data-estimated probability density functions (PDF) of wave heights for all the WC experiments recorded at gauge 1 (first column) and gauge 4 (second column).

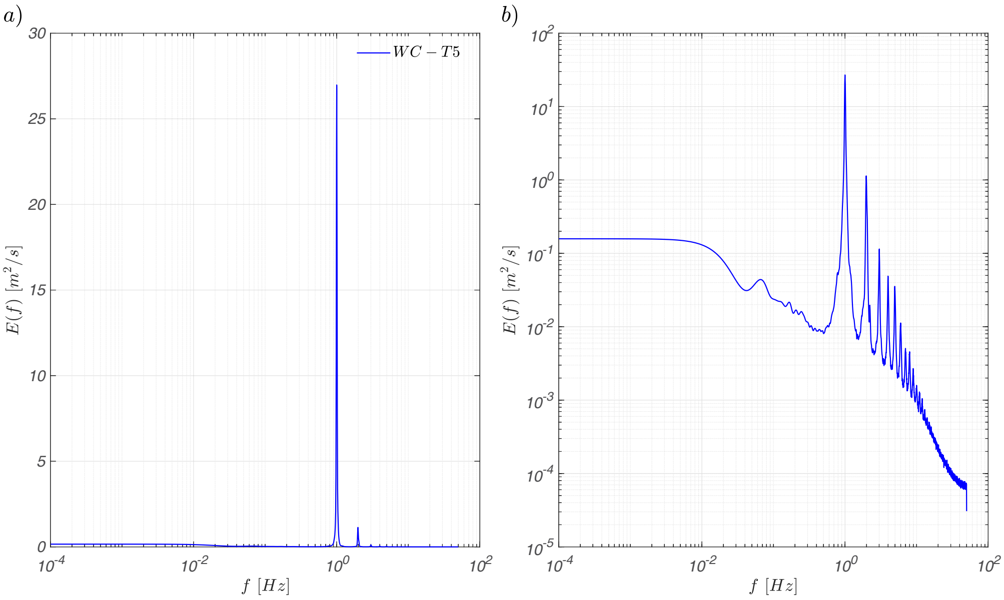

Fig. 3.12 (a) Semi-logarithmic and (b) logarithmic scale representation of the frequency spectrum of the free-water surface for the case WC−T5.

the main peak is associated with the wave motion. An alternative explanation is that the emergence of secondary peaks in the spectrum was associated to the asymmetric shape of the waves due to nonliear effects. As showed in Fig. 3.12(b), the main peak is complemented with secondary peaks at frequencies which are linearly proportional to the main one, indicating a possible organised feature.

This important alteration of the wave surface characteristics in the WC experiments was likely caused by one of the following factors:

i) the up-welling configuration of the inlet, with the waves imposed on the current. As reported by Robinson et al. (2015), the up-welling configuration of the inlet may lead to significant free-surface perturbations because in such a scenario the wavemaker can have difficulties in creating waves;

ii) the interaction of the current boundary layer with the free-surface. In particular, the irregularities in the wave heights could be triggered by turbulent fluctuations associated with the current.

It is not possible to establish which effect is dominant for the experimental setup used in the current study.

As it will be discussed in detail, this wave irregularity both in space and time makes the interpretation of the interaction between waves and turbulence more complicated as it adds more degrees of freedom. On the one hand, this represents a shortcoming, on the other hand it makes the experiments closer to real (i.e. field) conditions were regular monochromatic waves are essentially impossible to encounter (Goda, 2010). This wave irregularity made the decomposition of the signal (i.e. into mean, wave and turbulent component) very challenging using standard techniques reported in the literature. This stimulated the author to employ the Empirical Mode Decomposition (EMD) technique, which now seems to be a leading method for the interpretation of field velocity measurements (Qiao et al., 2016; Schmitt et al., 2009). Therefore the results from this work will find a fairly straightforward comparison with companion field data.

3.2.3 Signal Decomposition

Unsteady turbulent velocity signals can be decomposed according to the so-called triple decomposition (Hussain and Reynolds, 1970). For instance, the longitudinal instantaneous velocity component can be decomposed as:

$$u = U + \tilde{u} + u' \tag{3.9}$$

where U is the time-averaged velocity, $\tilde{u}$ is the periodic component of the velocity (e.g. a periodicity imposed by the passage of a wave) and u' is the turbulent fluctuations. The periodic component $\tilde{u}$ can be determined with $\tilde{u} = \langle u \rangle - U$, where $\langle u \rangle$ is the phase-averaged velocity which is determined by averaging over an ensemble of samples taken at a fixed phase in the imposed oscillation and it is expressed as:

$$\langle u \rangle = \frac{1}{N} \sum_{i=1}^{N} u(t + iT) \tag{3.10}$$

where T is the period of the oscillation and N is the total number of cycles.

This signal analysis procedure, which grounds on the triple decomposition, is referred to as the phase-averaging method (Franca and Brocchini, 2015), and it has been successfully applied to study collinear waves and current situations in which sinusoidal waves were present (Kemp and Simons, 1982, 1983; Singh and Debnath, 2016; Umeyama, 2005, 2009b; Zhang and Simons, 2019).

Nevertheless, due to the high irregularity of the wave motion in the waves plus current experiments reported in this study (see Section 3.2.2), the phase-averaging method is not straightforward to apply because it is difficult to associate a precise phase to each wave which travels with slight changes in height and frequency. Indeed, the ensemble average statistics are strongly dependent on small errors in phase selection. With the purpose of overcoming this pending issue, a different time-series analysis technique, named Empirical Mode Decomposition (EMD), was employed to obtain the different components of the velocity signal.

While there are other options to decompose a signal (e.g., Fourier-based analysis, wavelet analysis, proper orthogonal decomposition, dynamic mode decomposition), the literature identifies EMD as the best option for non-stationary and nonlinear time-series taken from single point measurements (Huang and Wu, 2008). Its primary difference with respect to the other methods is that the EMD is based on the local characteristics of the data, making the method strongly adaptive and fully data-driven. In any case, the robustness of signal decomposition in the WCI context should be the subject of further work.

Empirical Mode Decomposition

The Empirical Mode Decomposition (EMD) was firstly proposed by Huang et al. (1998, 1999, 2003) and it immediately started to be employed in numerous disciplines. Some successful applications in fluid mechanics are: the analysis of turbulent scales in fully developed homogeneous turbulence (Huang and Wu, 2008; Huang et al., 2010), the quantification of the amplitude modulation effects in wall turbulence (Dogan et al., 2019), the study of wave-turbulence properties in the surf zone (Schmitt et al., 2009) or ocean-surface (Qiao et al., 2016), and the analysis of river flow discharge time series for hydrological assessments (Huang et al., 2009).

The EMD technique is particularly suitable to the analysis of non-stationary and nonlinear datasets (Huang et al., 1998, 1999). Differently from most other methods (e.g. spectrogram or wavelet), the basis (functions) of the EMD are directly inferred from the data themselves and no signal features are assumed a priori, not even its stationarity. The main drawback of EMD is that it is fully empirical and no rigorous mathematical foundations have been yet derived, although some theoretical justifications have been proposed (see, Flandrin et al., 2004). Nevertheless, the EMD procedure satisfies the perfect reconstruction property, namely the original signal can be reconstructed completely by summing all the functions that have been inferred from it. Such inferred functions are called Intrinsic Mode Functions (IMFs) and represent the natural oscillatory modes that are embedded in the signal. This set of elemental signals is able to capture the trend (low frequency), as well as high frequency oscillations, the first is left in the residual, which is the resultant signal obtained after all IMFs have been extracted, the latter are separated depending on their characteristics and stored in different IMFs. Each and every individual IMF must satisfy the following conditions (Huang et al., 1998, 1999):

i) "in the whole dataset, the number of extrema (maxima and minima) and the number of zero-crossing must either be equal or differ at most by one";

ii) "at any point, the mean value of the envelope defined by the local maxima and the envelope defined by the local minima is zero".

Hence, the IMF ideally represents zero-mean amplitude and frequency modulation components. The IMFs and the residual are extracted from the signal by means of the so-called sifting process (Huang et al., 1998, 1999, 2003). The first step of the sifting process is the localization of the maxima and minima in the original signal $S(t)$. Subsequently, the upper envelope $e_{max}(t)$ and the lower envelope $e_{min}(t)$ are reconstructed and the mean envelope can be calculated as $m_1(t) = (e_{max}(t) + e_{min}(t))/2$ (Fig. 3.13). At this point, the first component of the signal is determined as $h_1(t) = S(t) - m_1(t)$. Ideally, h_1 should be an IMF and therefore satisfy the aforementioned conditions. However, the h_1 generated by the first round of sifting is rarely a true IMF and can be often defined as a proto-mode function (PMF) that must be further processed until it respects the two IMF conditions. This can be accomplished through an iterative process: the generated $h_1(t)$ is set as the new input time-series and the sifting

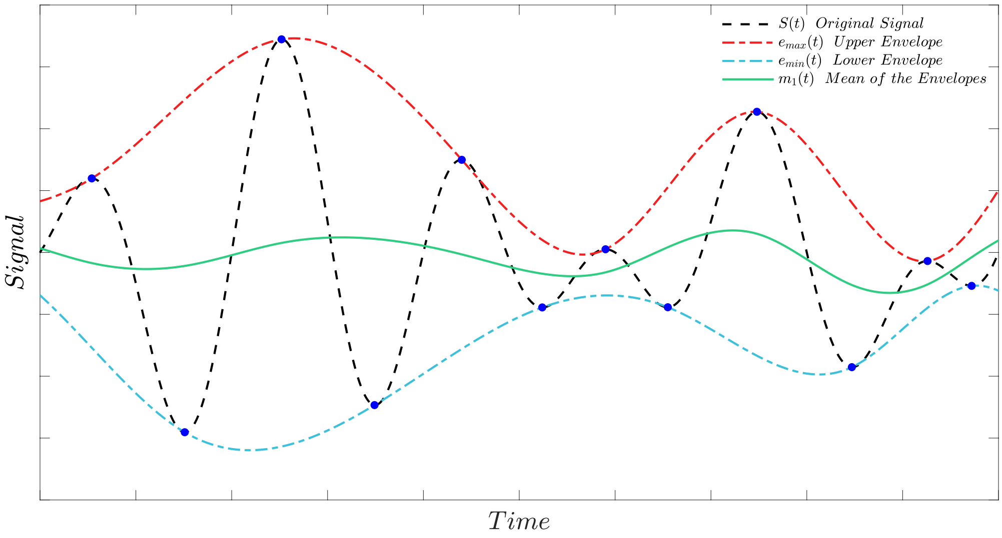

Fig. 3.13 Identification of the signal extrema (blue dots), construction of the upper and lower envelopes and computation of the mean envelope.

process is repeated j times until the first IMF from $h_{1j}(t) = h_{1(j-1)}(t) - m_{1j}(t)$ is obtained. The first IMF being defined as $C_1(t) = h_{1j}(t)$, the residual is obtained from the data by subtraction, i.e. $r_1(t) = S(t) - C_1(t)$. If the residual $r_1(t)$ is a constant, a monotonic function, or a function with at most one local extreme point, the sifting process is ended, otherwise $r_1(t)$ is used as the new input signal and the sifting is repeated again starting from the localization of the maxima and minima in $r_1(t)$.

When no more IMFs can be extracted from $r_n(t)$, the sifting is ended with $(n-1)$ IMFs and a residual extracted. Then, the original signal $S(t)$ can be rewritten as follow:

$$S(t) = \sum_{i=1}^{n-1} C_i(t) + r_n(t) \tag{3.11}$$

where $C_i(t)$ is the ith IMF following the order of extraction from the signal, i.e. $C_1(t)$ being the first extracted and $C_{n-1}(t)$ the last. Furthermore, $C_1(t)$ is the IMF with the highest characteristic frequency oscillation, $C_2(t)$ is the second highest, and so on until $C_{n-1}(t)$, which represents the IMF with the lowest characteristic frequency oscillation of the original time-series $S(t)$. In this way, each IMF refers to an oscillation that has lower frequency than previous one.

The sifting process has two main purposes: (i) to eliminate riding waves, i.e. the presence of a local minimum (e.g. maximum) greater (e.g. lesser) than zero between two successive local maxima (e.g. minima); and (ii) to make the oscillatory profiles more symmetric with respect to zero. For any PMF to become an IMF, the sifting process has to be repeated as many times as necessary to eliminate all the riding waves. Unfortunately, if too many sifting iterations are performed, the IMF reduces to a constant-amplitude frequency-modulated function, which annihilates the intrinsic amplitude variations and makes the results physically meaningless (Huang et al., 2003). In order to overcome this issue and to preserve the natural amplitude variations of the oscillations, the sifting process must be limited to a few iterations, which can be accomplished by introducing a stopping criterion. A plethora of stopping criteria have been suggested in the literature (Tabrizi et al., 2014) and here the Cauchy-Type convergence (SD, see Huang et al., 1998) and the Resolution Factor (RF, see Rato et al., 2008) were tested, with no substantial difference in the resultant IMFs. The SD criterion is based on the normalised squared difference of two consequent sifting results computed as:

$$SD = \frac{\sum\limits_{t=0}^{t=end} \left| h_{i(j-1)}(t) - h_{ij}(t) \right|^2}{\sum\limits_{t=0}^{t=end} h_{i(j-1)}(t)^2} \tag{3.12}$$

When SD reaches a predefined threshold value, the sifting must stop and, in particular, Huang et al. (1998) suggested that the threshold should be in the range $0.2 - 0.3$. The RF criterion pivots on the ratio between the energy of the original signal $S(t)$ and the energy of the average of envelopes $m_i(t)$ at the ith iteration computed as:

$$RF = 10 \log_{10} \left(\frac{S(t)^2}{m_i(t)^2} \right) \tag{3.13}$$

For this stopping criterion, Rato et al. (2008) recommended a threshold value in the range $40 - 60$ dB.

Besides the sifting stopping criterion, other factors that contribute to the outcomes of the EMD procedure are: the extrema localisation, the methods used to interpolate the extrema and calculate the envelopes, the handling of the end-points at the boundaries, and the decomposition stopping criteria (Huang et al., 2003; Rato et al., 2008; Zeiler et al., 2010). The EMD algorithm herein used is based on the one proposed by Rato et al. (2008), who improved the original procedure to minimize the impact of the aforementioned sensitive factors.

Adopted Procedure

The following procedure, based on Rato et al. (2008) algorithm, was adopted to separate the periodic (wave) and turbulent components in the original signals obtained from WC experiments:

Step I Obtain the IMF and the residual components for the signal through the EMD algorithm (Fig. 3.14);

Step II Compute the Fourier spectrum of the IMFs (Fig. 3.15);

Step III Identify in a log-log plot the IMFs that contain the wave signal (i.e. the ones with clear spectral peak/peaks associated with the wave motion);

Step IV Decompose the original waves plus current signal in a wave and a turbulent component. This can be achieved by summing up the IMFs that have been identified in Step III so that the wave signal is obtained. The remaining IMFs are then summed to obtain the turbulent signal;

Step V Perform a visual check of the signal and the wave and turbulent components extracted from it to qualitatively understand whether all the wave oscillations have been separated from the signal (Fig. 3.16);

Step VI If the quality check performed in Step V shows that some wave components are still present in the turbulent signal, then additional IMFs must be classified as wave components, subtracted from the turbulent signal and added to the wave signal. This step must be repeated until the turbulent signal shows no periodicity.

These steps are necessary as it is not straightforward to understand which IMFs contain information about the wave motion. It is found that, generally, no more than 4–5 IMFs, at most, are sufficient to describe the waves.

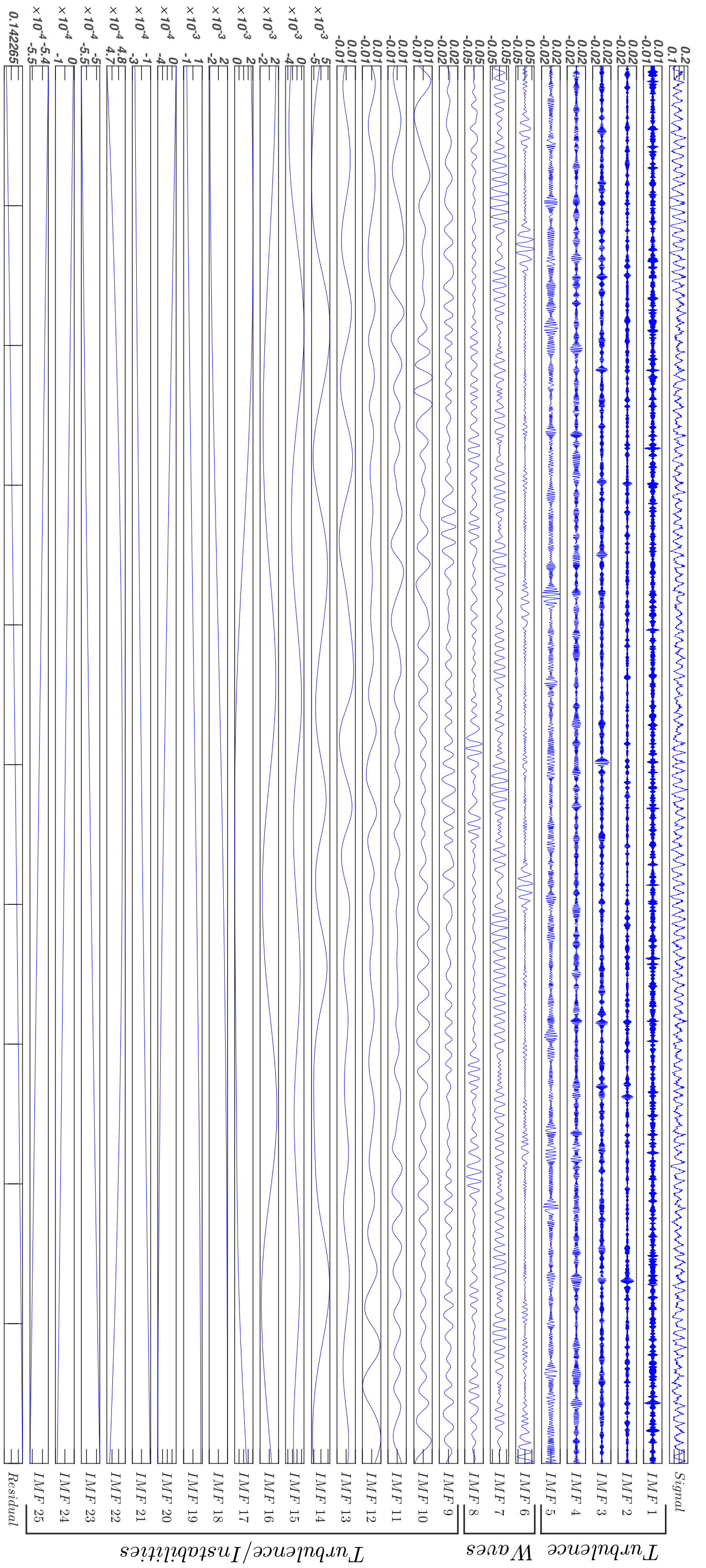

Fig. 3.14 Example of EMD application (test WC–T2, $y/h = 0.1$, longitudinal velocity component). In this case, the wave motion is entirely enclosed inside the IMFs number 6, 7 and 8, as it can be seen in Fig. 3.15. Note that only a small portion of the time series is reported.

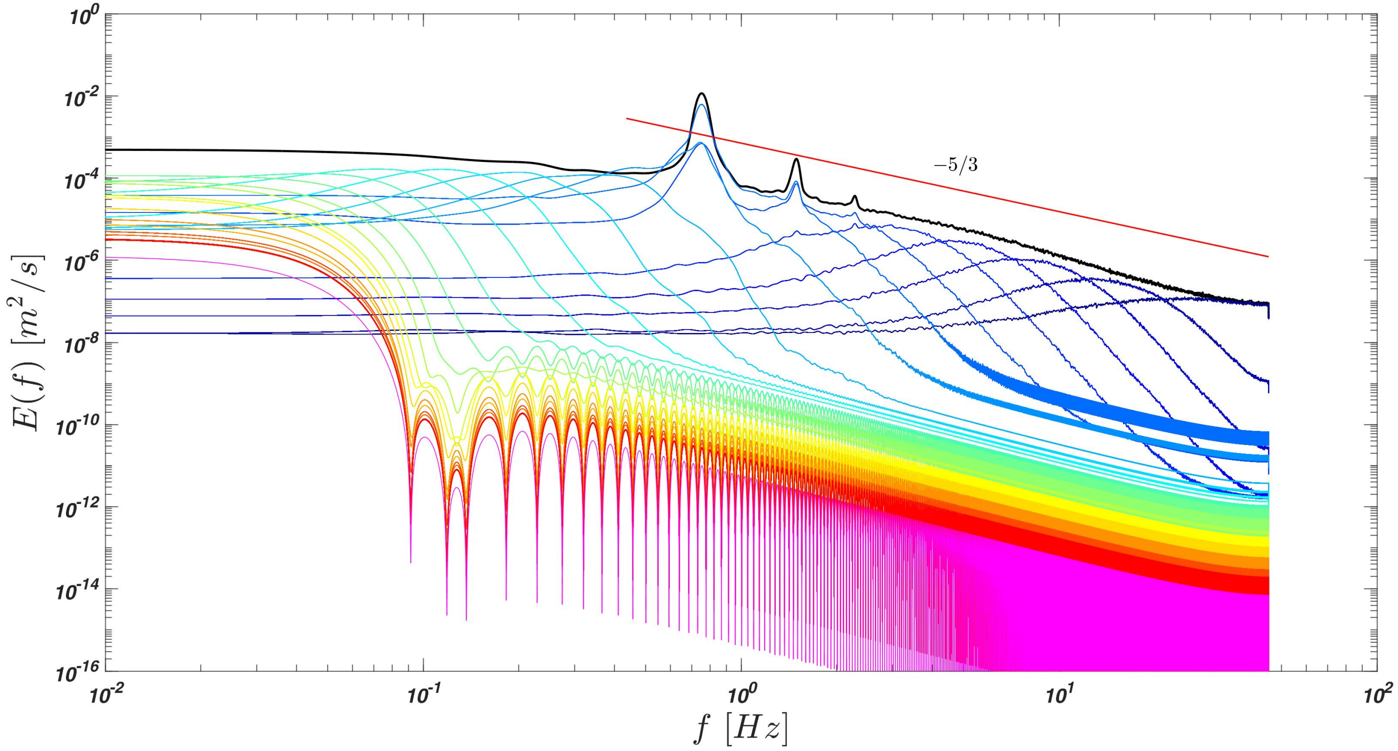

Fig. 3.15 Fourier spectrum of the original signal (thick black line), IMFs (various coloured lines) and residual (magenta line) reported in Fig. 3.14. The straight red line is the Kolmogorov -5/3 spectrum scaling.

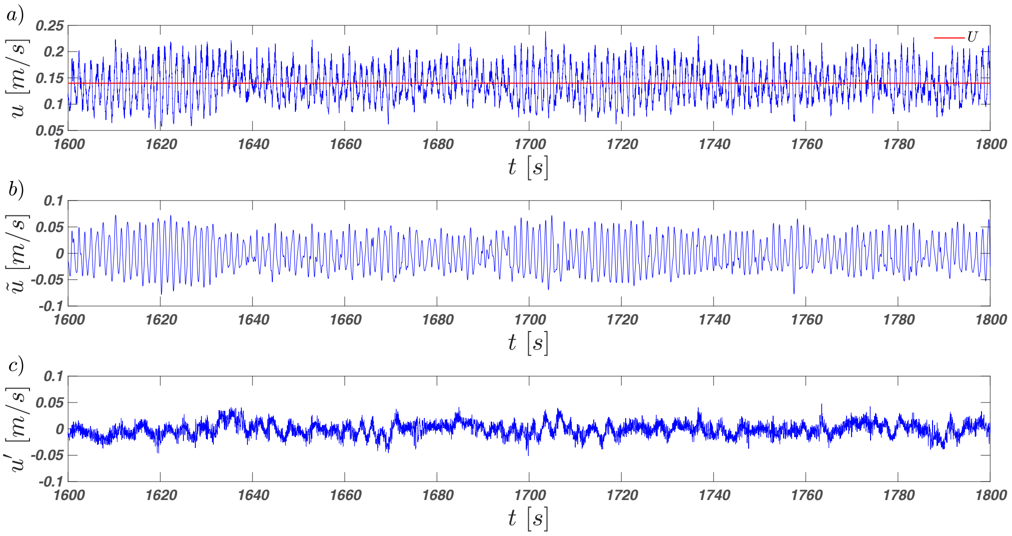

Fig. 3.16 (a) Original signal (blue line) and mean velocity (red line); (b) wave component and (c) turbulent component (test WC–T2, $y/h = 0.1$, longitudinal velocity component).

This procedure was applied to the experiments reported in Tab. 3.2. It is important to highlight that the number of IMFs extracted by the EMD procedure depends on the sampling frequency and on the threshold value chosen for the stopping criterion.

With this procedure, three different signals were obtained: the original or complete waves plus current signal, the signal part associated with the wave component and signal part associated with the turbulent component (as showed in Fig. 3.16).

Furtermore, a visual check of the turbulent spectrum was performed to assess the accuracy with which the adopted procedure separates the wave and the turbulent components around the frequencies interested by the wave motion. It is expected that some IMFs associated with the wave motion contain a background of turbulent energy. In other words, it is plausible that part of the signal energy assigned to turbulence is biased low while part of the signal energy assigned to waves is biased high. This is clearly visible in the example displayed in Fig. 3.17, where the adopted procedure creates an artificial valley in the turbulent spectrum that has no physical meaning (in general, turbulent spectrum decreases progressively). To counteract this problem, the valley was replaced with a straight line (in the log-log representation), similar to what was

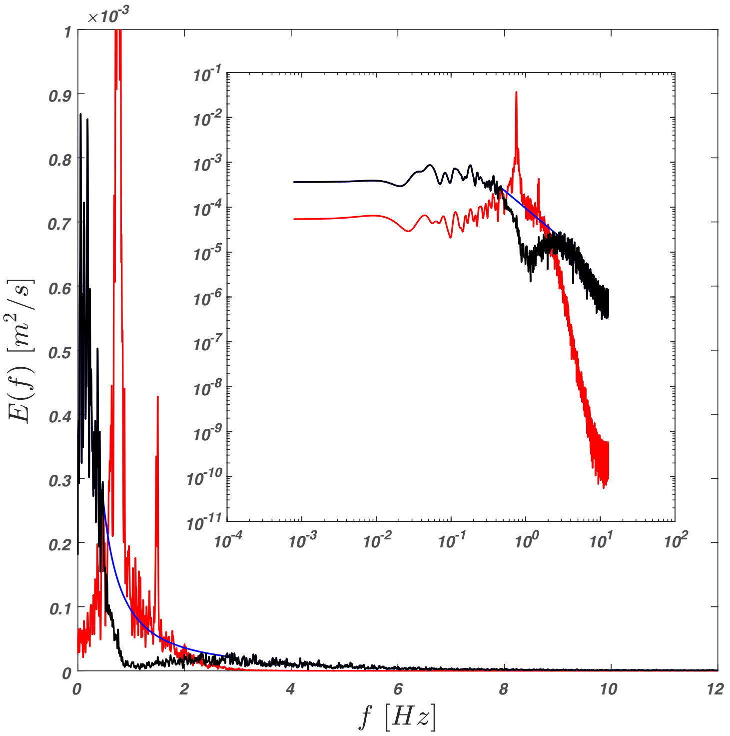

Fig. 3.17 Spectral representations of the longitudinal velocity measurement at $y/h = 0.03$ for test WC−T2. Black, red and blue lines respectively indicate the turbulent component, the wave component and the reconstructed signal. The main plot shows the spectra in linear scale, while the sub-plot reports the same spectra in a log-log scale.

done by Banerjee et al. (2015) and Vettori (2016). The edges of the valley were chosen as the last/first spectral point after/before which an evident changing from the previous/following ten points trend was detected. This way, the loss in spectral energy associated with the EMD procedure was estimated with reasonably good precision at each elevation for each test as:

$$ED_u = \frac{\hat{u'}^2 - u'^2}{\hat{u'}^2} \cdot 100 \tag{3.14}$$

$$ED_v = \frac{\hat{v'}^2 - v'^2}{\hat{v'}^2} \cdot 100 \tag{3.15}$$

where ED_u is the relative spectral energy deficit in percentage for the longitudinal component, and u'^2 and $\hat{u'}^2$ are the longitudinal variance computed as the integral of the spectrum with the artificial valley and after correction, respectively. The same, with different symbols, holds for the vertical component v. Such relationships are physically meaningful on the basis of Parseval's theorem (Bendat and Piersol, 2011), which states that the integral of the Fourier transform equals the variance of the function being transformed (the function being made of real values only). The relative spectral energy deficits were quantified as 20%–30% of the total spectral energy for the longitudinal component and 10%–20% for the vertical component. This further processing step is important because it allows correcting the standard deviations $\sigma_{u'}$ and $\sigma_{v'}$, which otherwise would be underestimated.Having quantified ED_u and ED_v, the corrected standard deviations ($\hat{\sigma}_{u'}$ and $\hat{\sigma}_{v'}$) were calculated as:

$$\hat{\sigma}_{u'} = \sigma_{u'} \sqrt{\frac{100}{100 - ED_u}} \tag{3.16}$$

$$\hat{\sigma}_{v'} = \sigma_{v'} \sqrt{\frac{100}{100 - ED_v}} \tag{3.17}$$

Eqs. (3.16)–(3.17) come out directly from Eqs. (3.14)–(3.15), after some manipulations. In the following, only the corrected estimates (i.e. $\hat{\sigma}_{u'}$ and $\hat{\sigma}_{v'}$) are reported and discussed. However, it is noteworthy that the profiles of $\hat{\sigma}_{u'}$ and $\hat{\sigma}_{v'}$ vary only marginally with respect to the profiles of $\sigma_{u'}$ and $\sigma_{v'}$, with no evident differences in their trends. This outcome encourages the application of EMD for the study of the turbulence in complex flow applications, such as in the case of waves superimposed on a turbulent flow.

3.3 Results

The results of LDA velocity measurements are presented and discussed in four subsections organised as follows: the mean velocity profiles are reported in Section 3.3.1, together with a theoretical argument partly explaining deviations of the WC cases from the benchmark CA; the second-order statistics are explored in Section 3.3.2; the quadrant analysis of the Reynolds shear stresses is showed in Section 3.3.3; finally, the spectral analysis for both the u and v velocity components is presented in Section 3.3.4. It is important to note that, due to the water surface level variation associated with the wave profile, in the WC experiments the LDA velocity measurements were collected up to $y/h \approx 0.83$.

3.3.1 Mean velocity profiles

This Section is devoted to the analysis of time-averaged velocity profiles obtained from the full signal of velocity time series. The vertical profiles of the mean longitudinal velocity for the waves plus current (WC) and current alone (CA) cases (Tab. 3.2) are reported in Fig. 3.18. The presence of waves is associated with a strong modification of the profiles' shape when compared to the CA case. In particular, WC−T1, WC−T2 and WC−T3 are characterized by a higher mean velocity throughout the water column with respect to the CA case, whereas, as also reported from other experimental studies (Kemp and Simons, 1982; Umeyama, 2005; Zhang and Simons, 2019), WC−T4 and WC−T5 display higher velocities near the bed and lower velocities towards the mean free surface level.

Bearing in mind that both the mean flow rate Q and the mean flow depth h did not vary across the cases (both flow meter and ultrasonics gauges measurements confirm no statistically significant changes in Q and h), at a first glance, one would expect that the integral of the mean velocity profile over the flow

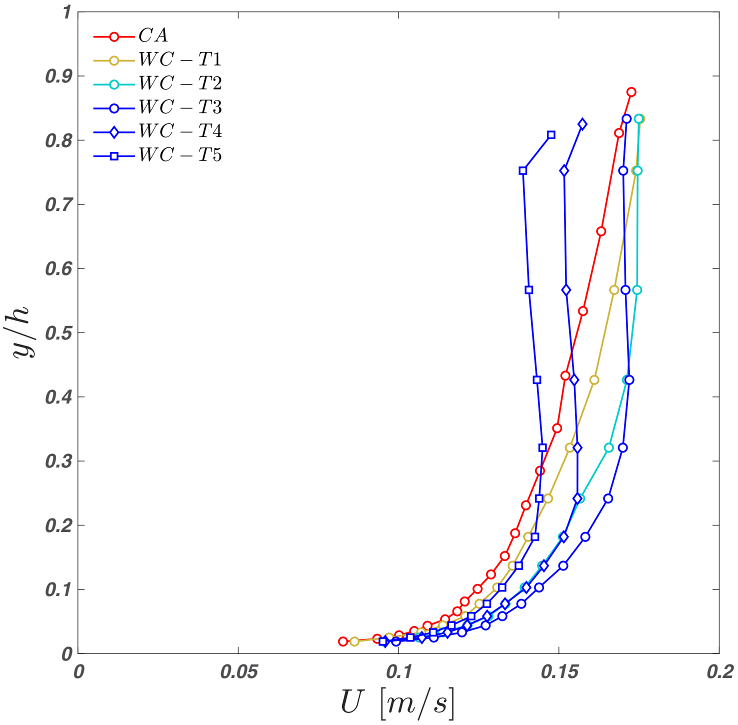

Fig. 3.18 Vertical profiles of the mean longitudinal velocity component for the CA (current alone) and WC experiments (complete waves plus current signal).

depth for WC and CA cases would match on the basis of mass conservation principles. This is not the case, especially for experiments WC−T1, WC−T2 and WC−T3. What follows demonstrates that mass conservation principles are not violated by a mismatch in the integral of mean velocity profiles pertaining to WC experiments. Indeed, such mismatches are to be expected if currents and waves interact non-linearly.

Considering the case of a one-dimensional open-channel flow (plus incompressibility condition), the mass conservation equation can be expressed as:

$$\frac{\partial Q}{\partial s} + \frac{\partial A}{\partial t} = 0 \tag{3.18}$$

where s is the longitudinal spatial coordinate at a generic point, $A = W\,h$ is the wetted area and W is the channel width. The flow rate Q can be re-expressed as:

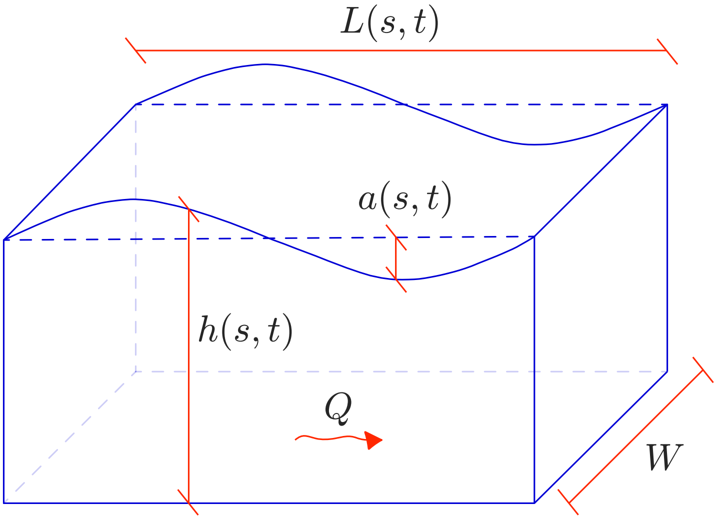

Fig. 3.19 Sketch of a wave with the definitions of the relevant parameters used in the continuity equation.

$$Q(s,t) = A\,U_b = W\,h\,U_b, \tag{3.19}$$

where U_b is the bulk velocity, i.e. the longitudinal velocity averaged over the whole cross section.

When waves (either random or regular) are superimposed to a current (Fig. 3.19), the water depth h and the bulk velocity U_b (and hence Q) are functions of both space and time, i.e. $h = h(s,t)$ and $U_b = U_b(s,t)$. By substituting Eq. (3.19) into Eq. (3.18), the continuity equation is expressed as:

$$\frac{\partial h\,U_b}{\partial s} + \frac{\partial h}{\partial t} = 0 \tag{3.20}$$

Applying the Reynolds decomposition, the variables h and U_b can be expressed as:

$$h(s,t) = \overline{h}(s) + F_h(s,t) \tag{3.21}$$

$$U_b(s,t) = \overline{U_b}(s) + F_U(s,t) \tag{3.22}$$

where $\overline{h}$ and $\overline{U_b}$ indicate the time-averaged values within a characteristic wave period T, while F_h and F_U are the fluctuations. It follows that $\overline{h}$ and $\overline{U_b}$ are defined as:

$$\overline{h} = \frac{1}{T}\int_0^T h(s,t)\,dt \tag{3.23}$$

$$\overline{U_b} = \frac{1}{T}\int_0^T U_b(s,t)\,dt \tag{3.24}$$

and, hence, are dependent on s only. Substituting Eqs. (3.21)–(3.22) into Eq. (3.20), applying the time-averaged operator to each term and after some manipulations, the following expression can be obtained:

$$\frac{\partial}{\partial s}(\overline{h}\,\overline{U_b} + \overline{F_h F_U}) = 0 \tag{3.25}$$

The argument of the partial derivative represents the time-averaged flow rate $\overline{Q}$, which, as the experiments demonstrated, is a conserved quantity. Hence:

$$\overline{Q} = \overline{h}\,\overline{U_b} + \overline{F_h\,F_U} \tag{3.26}$$

where $\overline{h}\,\overline{U_b}$ is the flow rate contribution provided by the the integral of the mean velocity profiles and the $\overline{F_h\,F_U}$ term represents the covariance between the free-water surface and the longitudinal depth-time-averaged velocity fluctuations. In current alone conditions, the latter term is negligible and the total flow rate can be well estimated by $\overline{h}\,\overline{U_b}$, whereas, based on the profiles shown in Fig. 3.18, in the WC case it can be non-negligible and quantifies non-linear interactions. Unfortunately, the exact value of $\overline{F_h\,F_U}$ cannot be investigated further using the measurements of velocity collected during this study (this would require instantaneous measurements of the depth averaged velocities, which cannot be performed with a LDA system), but from the profiles shown in Fig. 3.18, $\overline{F_h\,F_U}$ can be estimated approximately as 5–10% of $\overline{h}\,\overline{U_b}$.

Fig. 3.20(a–b) reports mean velocity profiles plotted in inner and outer scaling. The shear velocities for the WC experiments ($u_{\tau_{wc}}$) were estimated through the classical Clauser method (Clauser, 1956), assuming the occurrence of a logarithmic layer in the near-wall region. In particular, the best data

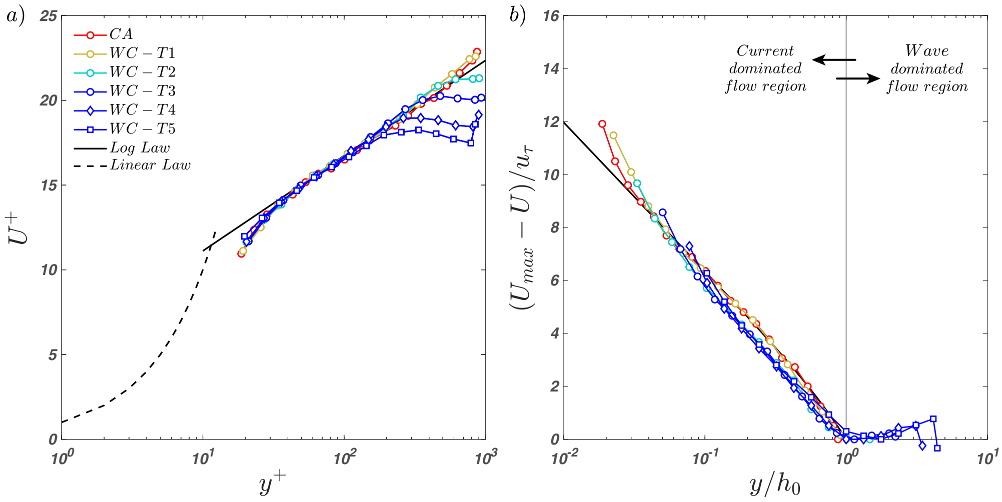

Fig. 3.20 Normalised mean velocity profiles for the longitudinal component: (a) inner, and (b) outer scaling. In (b) the vertical coordinate is normalised using h_0, which represents the distance from the bottom to the elevation where U reaches its maximum.

fitting in the range between $y^+ = 50$ and $y/h = 0.2$, with $\kappa = 0.41$ and $B = 5.5$ (values found in Section 2.4), provides the $u_{\tau_{wc}}$ used for the scaling of the WC tests (Tab. 3.2). The $u_{\tau_{wc}}$ are slightly higher than u_{τ_c} and this agrees with the detected increase in the gradient of the free surface $S_w = \mathrm{d}h/\,\mathrm{d}x$ in the presence of waves. The surface slope S_w was estimated by considering the mean water elevation recorded by the two ultrasonic gauges immediately upstream and downstream the LDA system, giving a value of $-0.815 \cdot 10^{-4}$ for the CA case and spanning from $-0.954 \cdot 10^{-4}$ to $-1.361 \cdot 10^{-4}$ for the WC cases.

By applying the inner scaling, the velocity profiles collapse within a narrow interval. The so-called two-log-profile structure suggested by Grant and Madsen (1979) and subsequently experimentally validated (Fredsøe et al., 1999; Yuan and Madsen, 2015) is not detectable in Fig. 3.20(a). This may be attributable to the fact that the Stokes length $l_S = \sqrt{2\nu/\omega}$, which to some extent quantifies wave boundary layer thickness δ_w in smooth-bed flows (i.e. $\delta_w = 2-4\,l_S$, Nielsen, 1992) ranges from $5.373 \cdot 10^{-4}$ to $7.598 \cdot 10^{-4}$ m that correspond to 4.7 to 6.5 wall units and therefore is fully buried within the buffer layer/viscous sublayer. Thus, it is not surprising that, until now, only rough-bed waves plus current experiments clearly show the presence of two distinct logarithmic layers (as the δ_w is magnified by the bed roughness).

Regarding the outer scaling (Fig. 3.20b), a reasonably good collapse occurs once the appropriate outer length-scale is chosen. It is found that the suitable outer length-scale in the context of wave plus current is h_0, i.e. the distance from the wall at which the mean velocity profile reaches its maximum and beyond which it decreases or maintains a constant value (as in flat plate turbulent boundary layers). By adopting this new outer length-scale h_0 and setting the U_{max} values as the velocity associated with h_0, the WC vertical velocity profiles collapse with the CA profile. Thus, Fig. 3.20(a–b) shows that for each experimental conditions there is a range of elevations where mean velocity profiles collapse both in inner and outer scaling. This is a remarkable result which suggests for the existence of a logarithmic-overlap layer as defined within the remit of asymptotic matching theories (Yaglom, 1979). In the previous literature pertaining to wave-current interaction, the existence of a logarithmic layer was never really demonstrated in this sense and always assumed on the observation that mean velocity profiles did have a log-type shape, i.e. a non physically-based argument.

It is herein introduced (and later in the text further substantiated) the concept that the height h_0 represents a crossover between two different flow regions: (i) the first, between the bed and h_0, where the flow is influenced by the presence of waves but retain, to a good extent, the character of a current (current-dominated flow region); (ii) the second, between h_0 and the free-surface, where the flow is mainly controlled by the wave motion (the wave-dominated flow region). From a physical point of view, the passage between these two regions will not be sharp as conceptualized above and it is plausible that a sizeable transition zone exists. However, as for the boundary layer concept, where the distinction between the turbulent and irrotational flow is set where the mean streamwise velocity U is equal to a certain percentage of the edge velocity U_e imposed by the potential flow (usually the 99%), here the division between the two regions follows a similar idea, i.e. where the mean streamwise velocity U attains its maximum value and after that decreases or remains constant within a certain range (e.g., 5%).

The analysis of second order velocity moments (presented in the next Section) demonstrates that waves alter the flow more through the imposition of vertical than horizontal motion. This suggests that h_0 is dictated by a trade off between two competing mechanisms: the vertical motion imposed by the

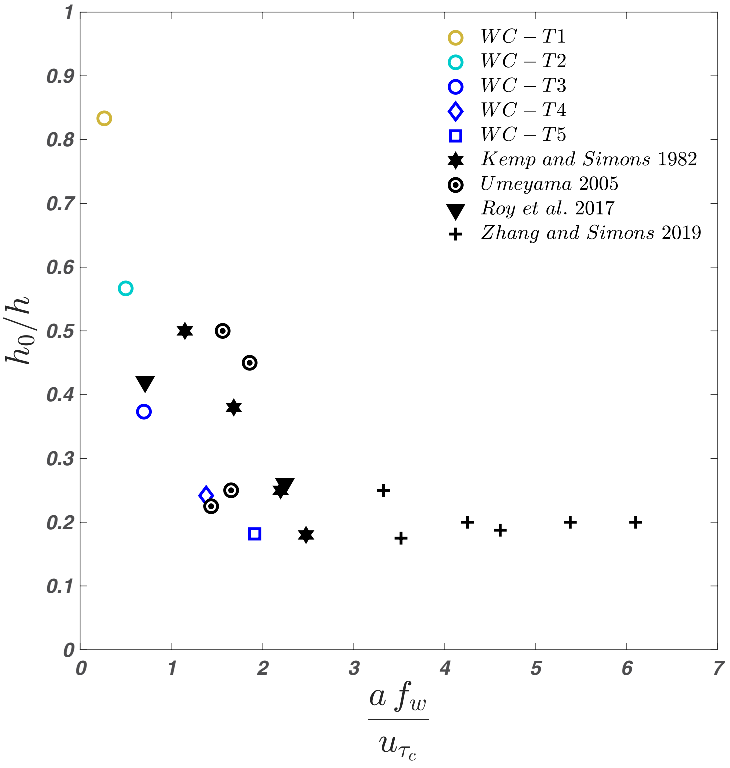

Fig. 3.21 The normalised outer length scale h_0 as a function of the dimensionless parameter $a\,f_w/u_{\tau_c}$. Results from Kemp and Simons (1982), Umeyama (2005), Roy et al. (2017) and Zhang and Simons (2019) are reported for comparison.

wave, which can be quantified by $a\,f_w$ and vertical (turbulent) motion imposed by the current, which scales well with the friction velocity u_{τ_c} (i.e. $\sigma_v \sim u_{\tau_c}$). Therefore, using similarity analysis principles, it is herein argued that h_0/h scales as:

$$\frac{h_0}{h} = F\left(\frac{a\,f_w}{u_{\tau_c}}\right) \tag{3.27}$$

where F stands for *it is function of.* Fig. 3.21 shows that the proposed scaling (Eq. (3.27)) identifies a clear and physically plausible trend in the data presented herein. In particular, for increasing values of $a\,f_w/u_{\tau_c}$, h_0/h decreases, meaning that the stronger is the vertical motion imposed by the waves the more the current-dominated region shrinks towards the bed, which makes sense. Data taken from the literature Kemp and Simons (1982), Umeyama (2005), Roy et al. (2017) and Zhang and Simons (2019) collapse fairly well with those presented herein. The non-negligible scatter is most probably due to the fact that literature data are associated with experimental conditions whereby the boundary layer of the current alone flow did not reach the free surface as in the present work. While data from the literature should be taken with care, Fig. 3.21 indicates that for high values of $a\,f_w/u_{\tau_c}$, h_0/h seems to reach a plateau of about 0.2. Clearly this result needs to be confirmed by further experiments to identify whether this is really a plateau or a very slow decrease. However, the existence of either a plateau or a slowly decreasing region is in line with the "shear sheltering" paradigm developed by Hunt and co-workers (Hunt and Durbin, 1999) whereby strong shear layers work as barriers for the penetration of any external motions. Clearly, in the case of wave-current flows, with increasing of $a\,f_w/u_{\tau_c}$, the motion imposed by the waves has to fight against an increasing shear imposed by the current to reach deeper zones towards the bed. This might explain while, the curve over which data collapse in Fig. 3.21 show a decreasing slope while increasing $a\,f_w/u_{\tau_c}$.

3.3.2 Second order velocity moments

The vertical profiles of the second-order velocity moments are reported in Fig. 3.22(a–c), Fig. 3.22(d–f) and Fig. 3.22(g–i) for the complete signal (σ_u,

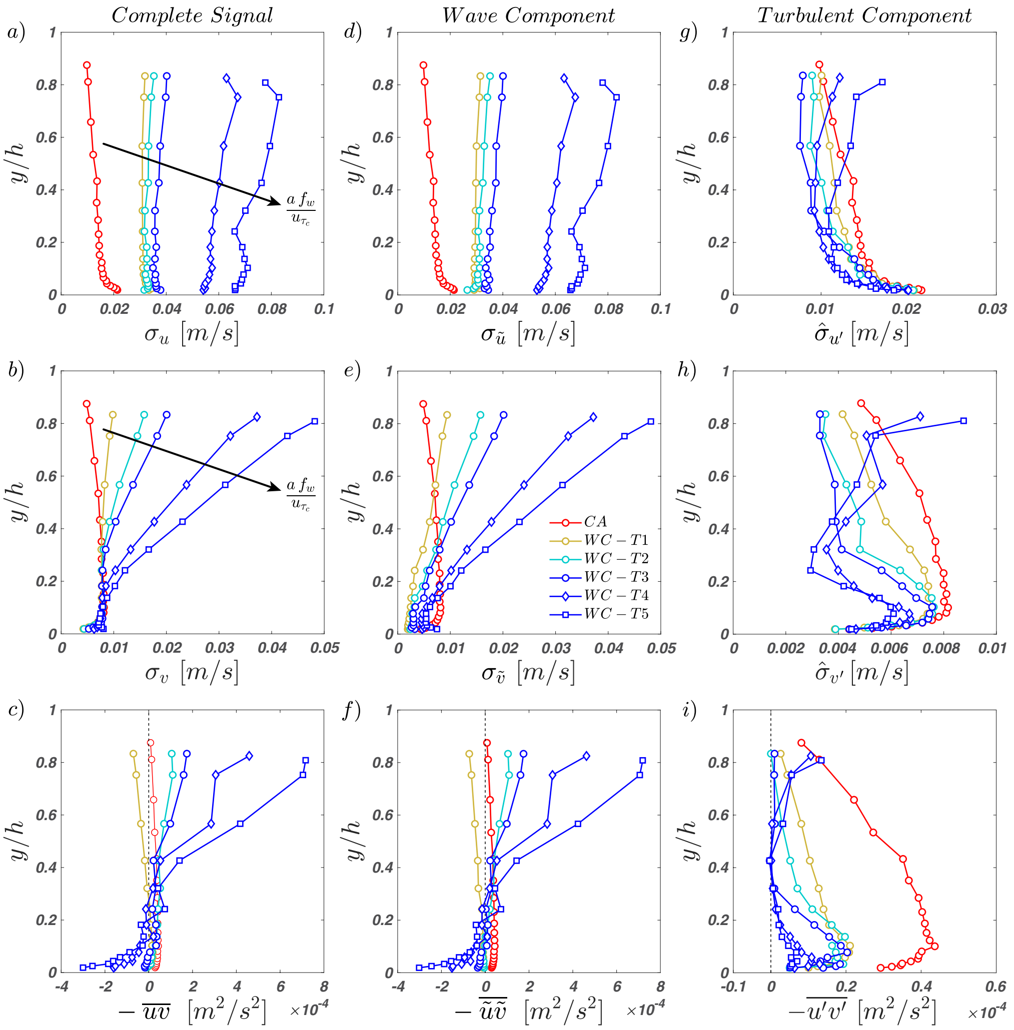

Fig. 3.22 Dimensional second-order velocity moments. Complete waves plus current signal: (a) standard deviation of the longitudinal velocity; (b) standard deviation of the vertical velocity; (c) shear stresses. Wave component: (d) standard deviation of the longitudinal velocity; (e) standard deviation of the vertical velocity; (f) shear stresses. Turbulent component: (g) corrected standard deviation of the longitudinal velocity; (h) corrected standard deviation of the vertical velocity; (i) Reynolds shear stresses. Note the different x-axis limits of panels (g), (h) and (i) with respect to the others.

σ_v and $-\overline{uv}$), the wave ($\sigma_{\tilde{u}}$, $\sigma_{\tilde{v}}$ and $-\overline{\tilde{u}\tilde{v}}$) and the turbulent ($\hat{\sigma}_{u'}$, $\hat{\sigma}_{v'}$ and $-\overline{u'v'}$) component, respectively.

For the complete waves plus current signal, the σ_u increases as the wave frequency and the wave amplitude increases (Fig. 3.22a). Furthermore, σ_u assumes values from 2 to 4 times higher than the standard deviation of the CA case. The profiles of $\sigma_{\tilde{u}}$ (the standard deviation of the wave signal) are very similar to those of the complete signal (Fig. 3.22d), indicating that the waves always dominate the velocity fluctuations with respect to turbulence.

For what concerns σ_v the WC cases closely follow the CA case in the lower part of the water column and deviate from the latter beyond a certain height that depends on $a\,f_w/u_{\tau_c}$. The profiles of $\sigma_{\tilde{v}}$ (Fig. 3.22e) follow closely those of the full signal σ_v although with a negative offset.

The shear stresses for the complete signal $-\overline{uv}$ (Fig. 3.22c) resemble those of the wave component $-\overline{\tilde{u}\tilde{v}}$ (Fig. 3.22f), although in WC−T1 and WC−T2 few differences can be seen near the bottom, where the shear stress values are negative for the wave component and positive for the complete signal.

It is worthy to spend some words on momentum balance. As shown in Nielsen (1992), the total shear stress τ_{tot} in a waves plus current flow can be estimated as:

$$\frac{\tau_{tot}}{\rho} = -UV - \overline{\tilde{u}\tilde{v}} - \overline{u'v'} + \nu\frac{\mathrm{d}U}{\mathrm{d}y} \tag{3.28}$$

where ρ is the flow density. The term $-UV$ is equal to zero only if the flow is horizontally uniform while $-\overline{\tilde{u}\tilde{v}}$ is usually dominant with respect to the Reynolds ($-\overline{u'v'}$) and viscous shear stresses. Eq. (3.28) is taken by assuming that mixed covariances between wave and turbulence component are also zero, i.e. the wave and turbulence events are uncorrelated. In principle the sum of all the shear stress component in Eq. (3.28) should provide an estimate of the shear stress in line with the friction velocity estimations obtained by fitting the mean velocity profiles through the Clauser method discussed in Section 3.3.1. Assuming that the viscous contribution in Eq. (3.28) is negligible (indeed the viscous contribution is worth only a 5% compared to the Reynolds shear stress value), it is evident from Fig. 3.22(i) and Fig. 3.22(f) that the sum of Reynolds and waves components of the shear stress is negative. This means that, in

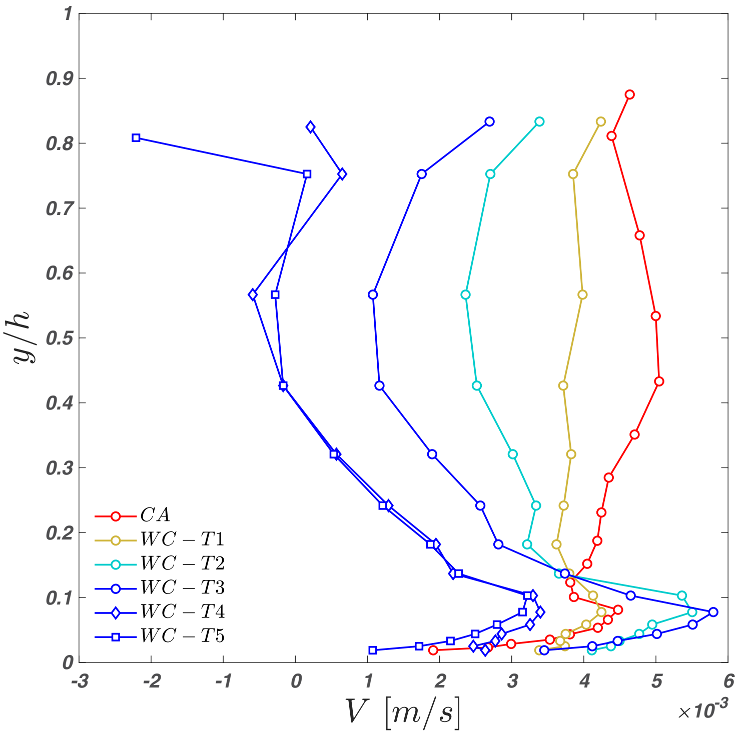

Fig. 3.23 Vertical profiles of the mean wall-normal velocity component for the CA (current alone) and WC experiments (complete wave plus current signal).

order to obtain a positive value of τ_{tot}, the term $-UV$ (which in the present experiments is non zero due to the non uniformity of the time-averaged flow) must be positive and compensating for the negative values imposed by the wave term. Unfortunately, this is not the case. Fig. 3.23 shows that V is almost always positive throughout the flow depth and hence meaning that $-UV$ is also negative. Clearly the available data do not allow for a closure of the momentum balance. However, it should be noted that the value of V (which is of the order of 10^{-3} m/s) is strongly sensitive to small misalignments of the LDA. This might explain the mismatch between τ_{tot} obtained from Eq. (3.28) and the one obtained from the Clauser method.

So far the analysis has been centred on second-order velocity moments obtained either from the full or the wave signal. From this point onwards the turbulent component is analysed in order to shed a light on how the presence of waves affect turbulence characteristics, which is the main focus of the present work.

It can be noted in Fig. 3.22(g–i) that both the standard deviations of the velocities and the Reynolds shear stresses associated with turbulence for the waves plus current cases strongly deviate with respect to the CA case.

The dimensional $\hat{\sigma}_{u'}$ and $\hat{\sigma}_{v'}$ profiles for the WC cases have lower magnitude than those for the CA case (Fig. 3.22g–h), except for the upper part of WC−T4 and WC−T5. The dimensional Reynold shear stresses $-\overline{u'v'}$ show a dramatic reduction in magnitude (Fig. 3.22i), as their values are more than halved compared to those for the CA case. The cases WC−T3 to WC−T5 show nearly null values of $-\overline{u'v'}$ at $y/h \approx 0.3$. The Reynolds shear stress remains null also for y/h higher than 0.3 for the case WC−T3, whereas it increases close to the free surface for the cases WC−T4 and WC−T5.

The weakening of the longitudinal and vertical standard deviations starting from $y/h \approx 0.1$ is revealed also in Singh and Debnath (2016) and Umeyama (2005, 2009a,b), while the strong reduction in $-\overline{u'v'}$ is also reported by Umeyama (2005). Furthermore, a slightly increase in the outer region for the standard deviations is revealed also in Roy et al. (2017), although these authors do not show a net change in the trend as showed in Fig. 3.22(g–h).

Clearly, it is extremely difficult to infer properties of turbulence and to obtain insights into the physics of wave current interaction by assessing dimensional quantities as reported in Fig. 3.22(g–h) (and in much of the past literature). As shown in the following text, the use of an appropriate scaling is quite revealing. The second-order moments in inner and outer scaling are reported in Fig. 3.24(a–f). The Reynold stress profiles do not well collapse in the inner scaling (Fig. 3.24a–c) and the results are similar to those reported in Fig. 3.22(g–i). The situation showed in Fig. 3.24(d–f) is different and the outer scaling unveiling interesting hidden features. By using h_0 as the outer length-scale, the $\hat{\sigma}_{u'}/u_\tau$ profiles collapse fairly well (the reader should be reminded that the turbulence signal was extracted through the EMD technique, which does retain shortcomings, so the collapse of data obtained in for $\hat{\sigma}_{u'}$ is, to the author opinion, quote remarkable) and no obvious turbulence damping can be detected in the u fluctuating component (Fig. 3.24d). On the other hand, the $\hat{\sigma}_{v'}/u_\tau$ profiles drop significantly and the data show a stratification depending on the parameter $a\, f_w/u_{\tau_c}$ (Fig. 3.24e). Furthermore, the extent of the plateau reduced significantly with increasing $a\, f_w/u_{\tau_c}$. This plateau is normally associated with

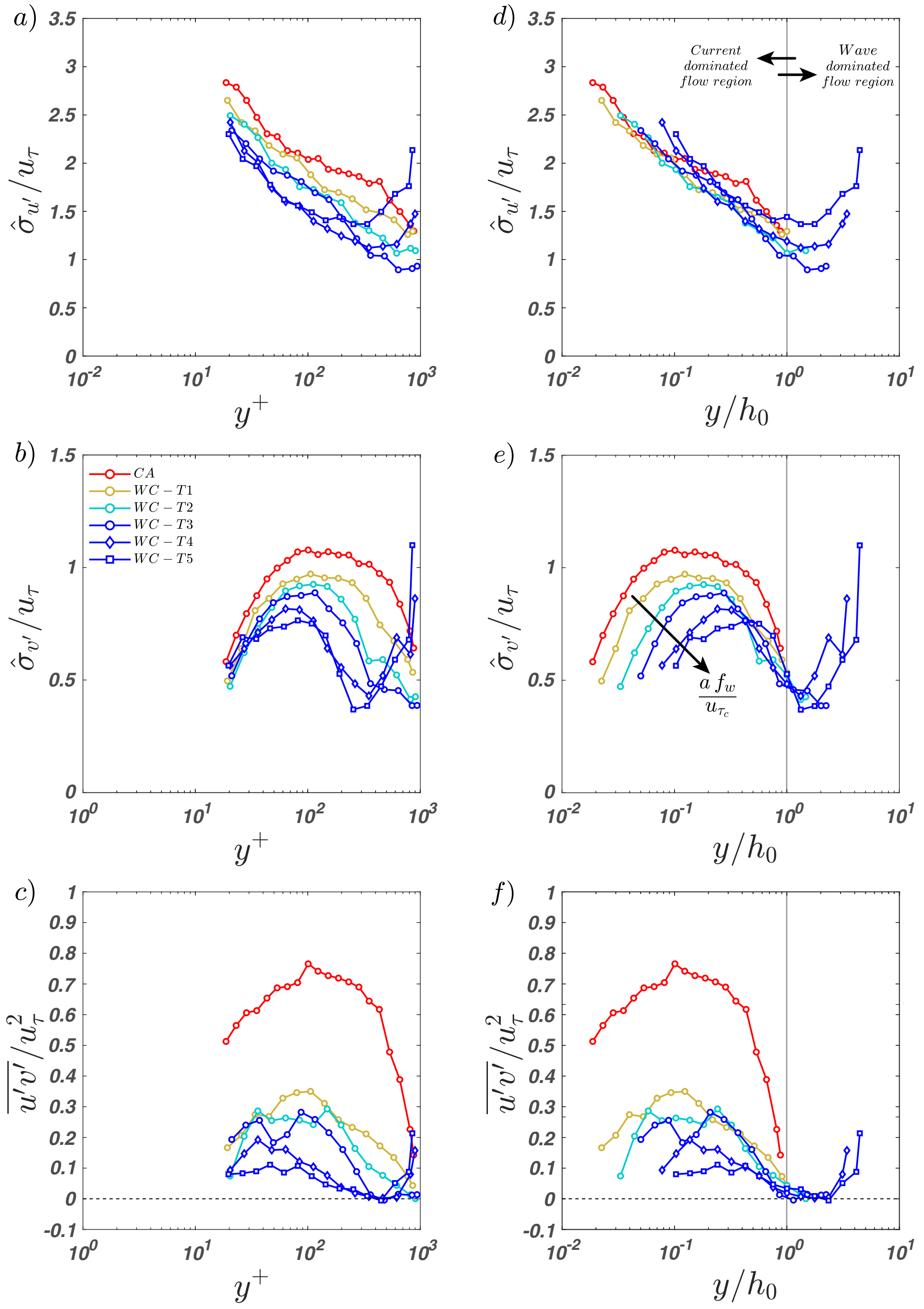

Fig. 3.24 Normalised second-order moments of the turbulent component. Inner scaling: (a) corrected standard deviation of the longitudinal and (b) vertical velocity; (c) Reynold shear stress. Outer scaling: (d) corrected standard deviation of the longitudinal and (e) vertical velocity; (f) Reynold shear stress.

the occurrence of attached eddies in the log-layer meaning that, consistently to what observed from mean velocity profiles (Fig. 3.20a–b), the larger $a\,f_w/u_{\tau_c}$ the more the log layer shrinks. It is interesting to note that the Reynold shear stresses $-\overline{u'v'}/u_\tau^2$ tend to zero for $y/h_0 \approx 1$ (Fig. 3.24f). This confirms that h_0 is an outer length-scale akin to a boundary layer depth whereby below h_0 the wave-current flows behave, to some extent, like wall flows. Moreover, $\hat{\sigma}_{u'}/u_\tau$ and $\hat{\sigma}_{v'}/u_\tau$ and $-\overline{u'w'}/u_\tau^2$ collapse very well at $y/h_0 \approx 1$ and also they undergo a clear local minimum, which confirms that h_0 is a crossover length scale between two flow regions dominated by a different physics. It is important to recall that the Reynold shear stress cannot be corrected to recover the artificial loss experienced in the spectral energy through the EMD technique as it has been done for the standard deviations (Section 3.2.3). For this reason, the damping of $-\overline{u'v'}/u_\tau^2$ in the WC cases, despite being present, could be less pronounced that what shown in Fig. 3.24(f).

3.3.3 Quadrant Analysis

The classical quadrant analysis (Wallace, 2016; Wallace et al., 1972) was also used to study the modification of the bursting cycle caused by waves superimposed on the turbulent flow. The quadrant analysis allows identifying distinct turbulent events by analysing the signs of the synchronous velocity fluctuations. In particular, creating a Cartesian plan with u' on the abscissa and v' on the ordinate, four different quadrants can be defined in an anticlockwise order: quadrant 1 ($\overline{u'v'}_{Q1}$) where $u' > 0$ and $v' > 0$, quadrant 2 ($\overline{u'v'}_{Q2}$) where $u' < 0$ and $v' > 0$, quadrant 3 ($\overline{u'v'}_{Q3}$) where $u' < 0$ and $v' < 0$ and quadrant 4 ($\overline{u'v'}_{Q4}$) where $u' > 0$ and $v' < 0$. These quadrants are associated with the following turbulent events, namely outward interactions, ejections, inward interactions and sweeps, respectively. The inward and outward interactions correspond to high-speed fluid reflected outwards from the wall and low-speed fluid deflected towards the wall, respectively, and account for the excess of shear stress produced by ejections and sweeps during the bursting cycle, since they have opposite sign (Wallace, 2016; Wallace et al., 1972).

The distributions of the normalised quadrant contributions in outer scaling for all the experiments is showed in Fig. 3.25(a–f). As expected, in the CA case (Fig. 3.25a), the ejections dominate the turbulent events, except for

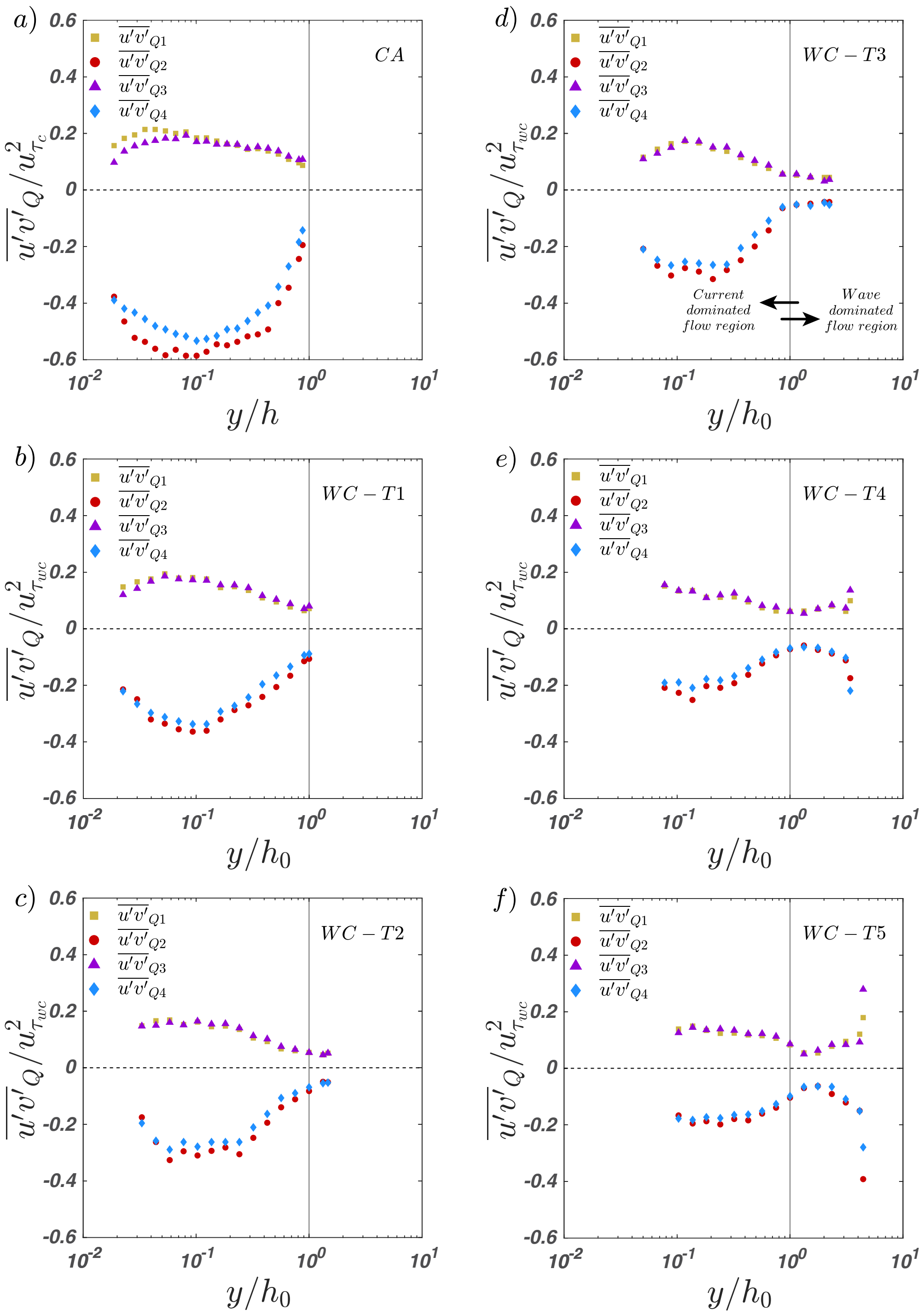

Fig. 3.25 Distributions of the quadrant contributions to the Reynolds shear stress for each experiment (turbulent component) in outer scaling: (a) CA; (b) WC−T1; (c) WC−T2; (d) WC−T3; (e) WC−T4; and (f) WC−T5. In particular, $\overline{u'v'}_{Q1}$ is the outward interaction, $\overline{u'v'}_{Q2}$ is the ejection, $\overline{u'v'}_{Q3}$ is the inward interaction, and $\overline{u'v'}_{Q4}$ is the sweep. The vertical grey line indicates $y = h_0$.

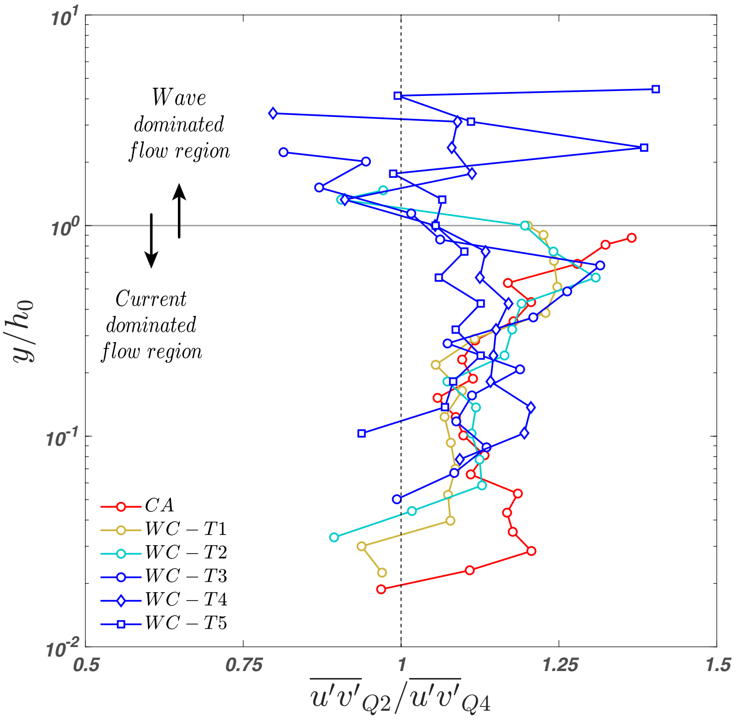

Fig. 3.26 Ratio between the contribution of quadrant 2 ($\overline{u'v'}_{Q2}$) and quadrant 4 ($\overline{u'v'}_{Q4}$) to the Reynolds shear stress in outer scaling (turbulent component).

$y/h < 0.02$ where the sweeps and ejections provide similar contributions (Nezu and Nakagawa, 1993). Similarly, the WC experiments are mainly ejection-dominated, although the difference between the $\overline{u'v'}_{Q2}$ and $\overline{u'v'}_{Q4}$ contribution is less marked than in the CA case. Generally, all the sweep and ejection contributions are smaller in the WC cases than in the CA case, whereas for the outward and inward interactions the values remain roughly comparable. This does not completely agree with the findings of Zhang and Simons (2019), where the $\overline{u'v'}_{Q2}$ and $\overline{u'v'}_{Q4}$ are nearly equivalent to the CA case. Once again, the y/h_0 limit delineates the two different flow regions (indicated in Fig. 3.25(a–f) with a grey line). For $1 \leq y/h_0 \leq 2$ the quadrant contributions are almost null, indicating quasi-isotropic turbulence. For $y/h_0 > 2$, all the quadrant contributions for test WC−T4 and WC−T5 grow, indicating that a new source feeds turbulence in the wave-dominated region.

Fig. 3.26 shows the ratio between ejection and sweep for all the tests. Despite the data scatter, the ratio $\overline{u'v'}_{Q2}/\overline{u'v'}_{Q4}$ for the WC cases seem to be consistent with the CA case when the outer scaling y/h_0 is used.

3.3.4 Spectral analysis

It is now interesting to investigate how, with respect to the benchmark CA case, waves affect velocity spectra in WC experiments. To this end, Fig. 3.27(a–f) and Fig. 3.28(a–f) report 1-D pre-multiplied spectra of the complete signal of the longitudinal and vertical velocity component, respectively. The wavenumnber k_x was computed by invoking the Taylor frozen-turbulence hypothesis in the same manner as reported in Section 2.5.2, i.e. $k_x = 2\pi f/U(y)$, where f is the spectral frequency. It is important to highlight that the Taylor hypothesis is valid for spectral estimates associated with turbulent eddies. Frequencies associated with waves' motion should be transformed into wavenumbers using the waves' celerity.

The pre-multiplied spectra in the CA experiment display the same double peak feature(green and red arrows in Fig. 3.27a) as reported in Fig. 2.17(a–g) that is typical evidence of the occurrence of LSMs and VLSMs in the flow. Note that the remaining panels in Fig. 3.27(b–e) refer to WC experiments where spectral peaks associated with characteristic waves' wavenumbers are much

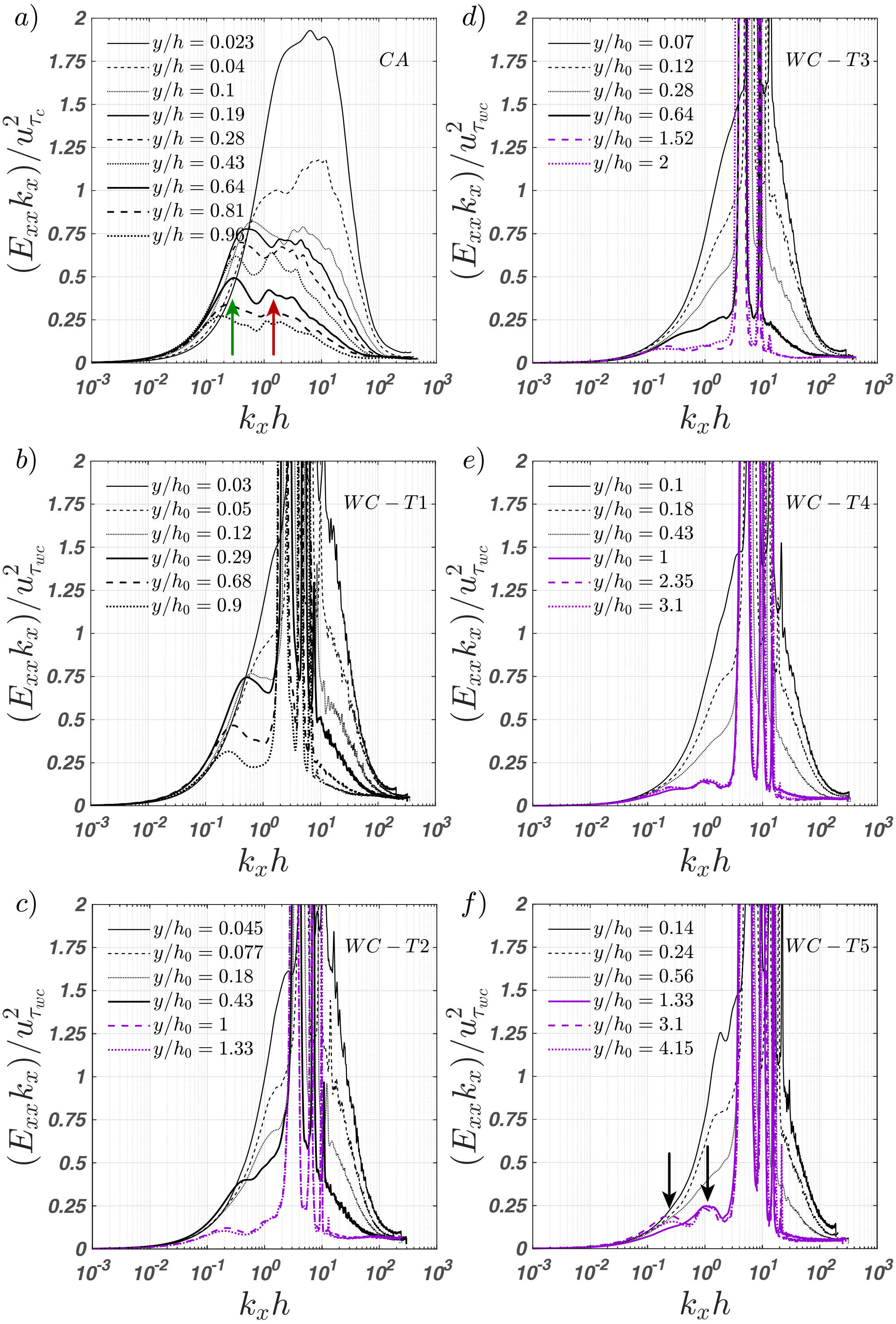

Fig. 3.27 Outer-scaled pre-multiplied 1-D spectra of the longitudinal velocity component (complete wave plus current signal). Each panel reports spectra at different elevations for one experimental condition. Black lines identify vertical elevations below h_0 (i.e. in the current-dominated flow region) whereas purple lines above it (i.e. in the wave-dominated flow region). Red and green arrows in panel a) identify spectral peaks associated with LSMs and VLSMs, respectively. Black arrows in panel (f) identify spectral peaks presumably associated with Langmuir-type turbulence in WC experiments; peaks at similar wavenumbers are also observed in panels (c), (d) and (e).

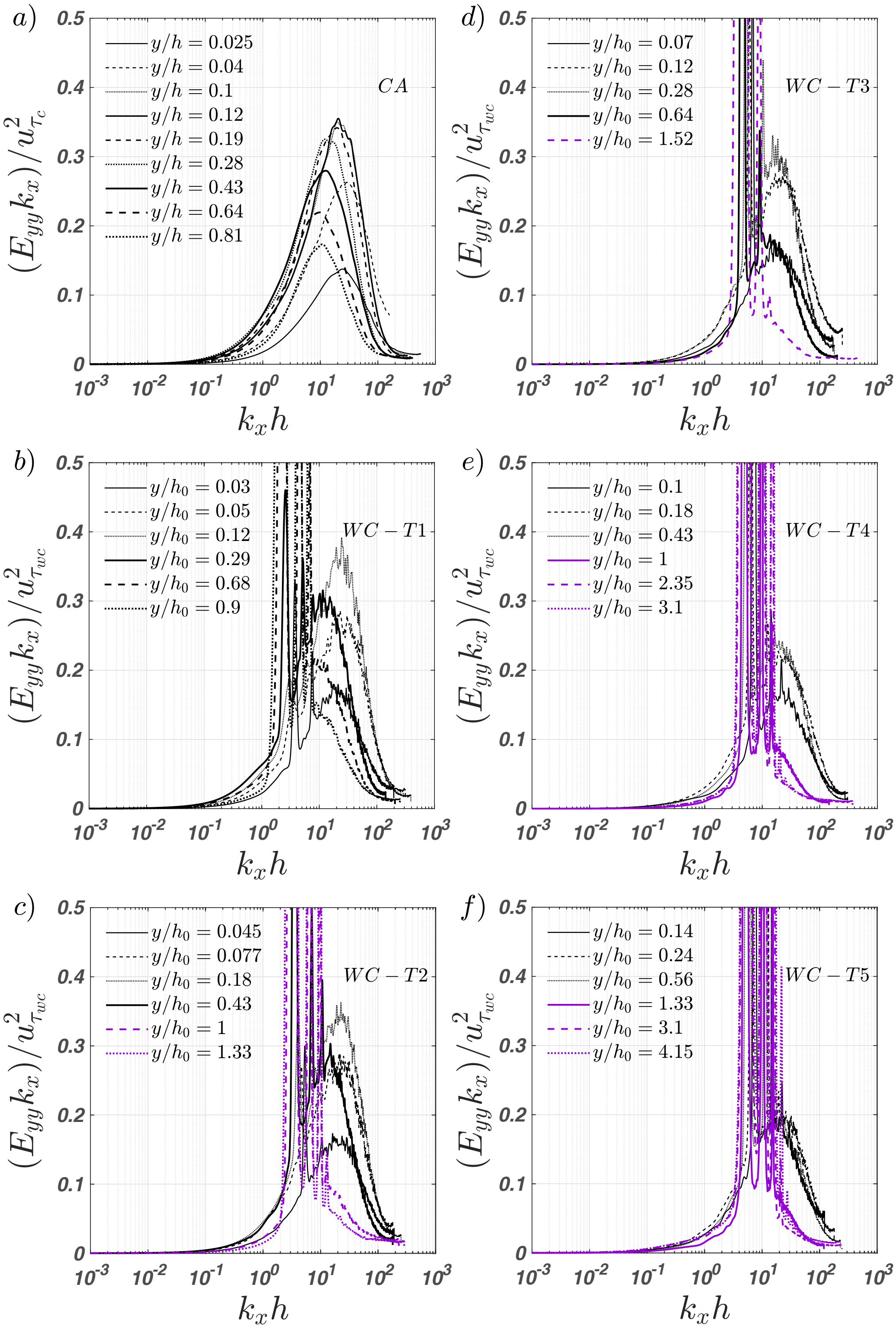

Fig. 3.28 Outer-scaled pre-multiplied 1-D spectra of the vertical velocity component (complete wave plus current signal). Each panel reports spectra at different elevations for one experimental condition. Black lines identify vertical elevations below h_0 (i.e. in the current-dominated flow region) whereas purple lines above it (i.e. in the wave-dominated flow region).

more energetic than the remaining part of spectral estimates. For convenience, such peaks are cut out of the panels to allow for a more comfortable analysis of spectral estimates at turbulence-related wavenumbers, which indeed reveal intriguing features. When waves are weak (i.e. $a\, f_w / u_{\tau_c}$ is low), as in experiment WC−T1, VLSMs can still be identified in the spectra, but they are completely suppressed for all the other WC experiments, which are associated with more intense waves. LSMs cannot be detected in any of the WC experiments because they normally occur at wavenumbers very similar to those associated with the waves. The reason why VLSMs are suppressed is difficult to identify because their generation mechanism is still unknown. However, some working hypotheses can be made. If VLSMs are the result of a concatenation of LSMs as argued by Adrian and co-workers (Kim and Adrian, 1999), the fact that waves have the same wavenumber as LSMs indicates that LSMs may be affected, if not suppressed, by waves, thus removing from the flow the building block of VLSMs. On the other hand, if VLSMs are the result of an outer layer cycle, as argued by Cossu and co-workers (Cossu and Hwang, 2017), then the reason could be different but with the data available from the present work it is hard to identify it.

Spectra pertaining to the wave-dominated flow region (purple lines) also show some rather unexpected features. They all display either one or two peaks (or bumps) at rather low wavenumbers, suggesting that the wave-dominated flow region hosts long turbulence structures (about 25 and 6 times the flow depth for the lowest and highest wavenumber peak, respectively) at scales comparable to LSMs and VLSMs. This is rather counterintuitive because in the current-dominated flow region such structures were suppressed by waves and therefore it becomes unclear why they appear in the wave-dominated flow region. A plausible explanation is provided in Section 3.4.

Fig. 3.28(a−f) shows pre-multiplied spectra of the vertical velocity component. The striking feature of these spectra is that in the current-dominated flow region (i.e. $y/h_0 < 1$) there is a clear scale separation between peaks due to energetic turbulent structures and peaks associated with waves. This indicates that the fluctuations in vertical velocity are induced by a mechanism that is different from waves and, presumably, related to current shear production. Conversely, in the wave-dominated flow region (i.e. $y/h_0 > 1$) there is no such scale separation (i.e. it is impossible to distinguish between a turbulence and waves' spectral peaks), which confirms that turbulence here is associated with mechanisms powered by waves.

3.4 Summary and discussion

The experimental results presented in Section 3.3 provide an interesting picture about turbulence in open-channel flows perturbed by collinear waves. The major outcomes are summarised below.

As surmised in the literature, but never really demonstrated, a genuine logarithmic/overlap layer does occur in WC flows. This is corroborated by Fig. 3.20(a–b) where, for a range of elevations, mean velocity data collapse both in inner and outer scaling, provided that the maximum velocity U_{max} of the profile and the elevation at which it occurs (h_0) are employed to define the velocity defect and the outer length-scale, respectively. Interestingly, h_0 also corresponds to the elevation where Reynolds shear stress reduces to zero, which endorses the hypothesis of h_0 being a length-scale akin to a boundary layer depth below which the flow scales similarly to canonical wall-flows and is dominated by the current.

This hypothesis is further corroborated by the analysis of the Reynolds stress normalised with the appropriate shear velocity (i.e. u_{τ_c} for the CA case and $u_{\tau_{wc}}$ for the WC cases) and plotted versus y/h_0. As shown in Fig. 3.24(a–f) and discussed in Section 3.3.2, in the current-dominated flow region, these profiles display some similarities with the profiles of canonical wall-flows even though they are not free from wave effects. In particular, $\hat{\sigma}_{v'}/u_\tau$ are strongly damped by the presence of waves while $\hat{\sigma}_{u'}/u_\tau$ seem to be weakly affected. The damping of $\hat{\sigma}_{v'}/u_\tau$ strongly depends on the intensity of the vertical motion imposed by the waves, namely $a\,f_w/u_{\tau_c}$. This suggests that waves alter the current more through vertical than horizontal motion and supports the hypothesis that the relative depth h_0/h scales with $a\,f_w/u_{\tau_c}$ (see Fig. 3.21) as this parameter quantifies the ratio between the intensity of vertical motion imposed by the wave ($a\,f_w$) to that of turbulence imposed by the current (u_{τ_c}). Fig. 3.21 shows that h_0/h reduces as $a\,f_w/u_{\tau_c}$ increases, meaning that the current-dominated flow region shrinks towards the bed, leaving space to an overlying region where turbulence is controlled by wave motion, i.e. the wave-dominated flow region.

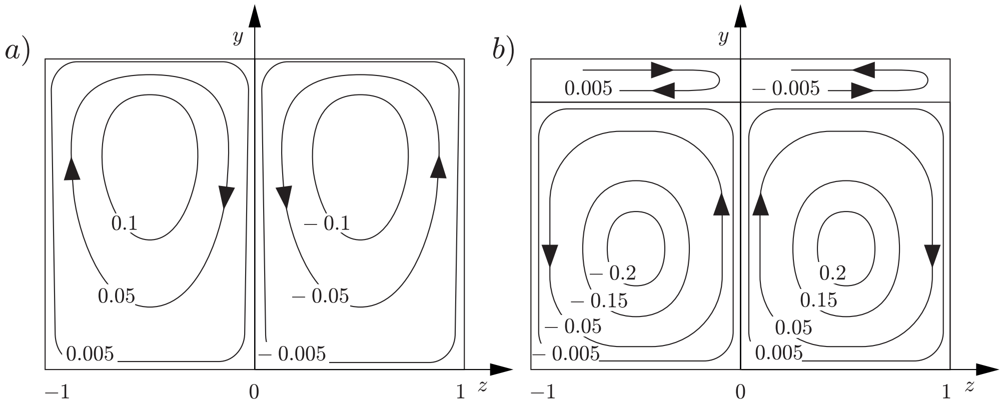

Fig. 3.29 (a) Contours of the transverse stream function associated with the first instability mode as detected by Huang and Mei (2006); (b) contours of the transverse stream function of the second mode of instability detected by Huang and Mei (2006). Figure adapted from Huang and Mei (2006).

Spectral analysis provides important information about the structure of turbulence in both regions. In particular, for $y/h_0 < 1$, it was observed that, provided the parameter $a\,f_w/u_{\tau_c}$ is big enough, the peak associated with VLSMs disappears in the longitudinal velocity spectra pertaining to WC experiments. On the contrary, in the wave-dominated region, turbulence structures at similar wavenumbers to those commonly associated with LSMs and VLSMs seem to re-appear. It is rather difficult to confidently provide a physical explanation for the occurrence of these large-scale structures (especially without having spatial information of the flow as it would be provided by Particle Image Velocimetry, PIV). However, some speculative hypotheses can be made.

Towards this end, it is worth recalling the study by Huang and Mei (2006), which reports a linear stability analysis of turbulent open-channel flows over smooth beds superimposed by waves, exactly as in the present study. Besides linearising the equation of motion and boundary conditions at the free surface and at the bed surface, Huang and Mei (2006) made the following assumptions: the dimensionless water depth was set of order unity $kh = \mathcal{O}(1)$, (ii) the wave steepness $\epsilon = ka$ was small; (iii) the wave orbital velocity was set comparable to the current velocity; all these conditions are reasonably met in the experiments discussed in the present Dissertation.

Interestingly, their stability analysis identified two large-scale unstable modes in the form of cellular structures with longitudinal vorticity (see Fig. 3.29).

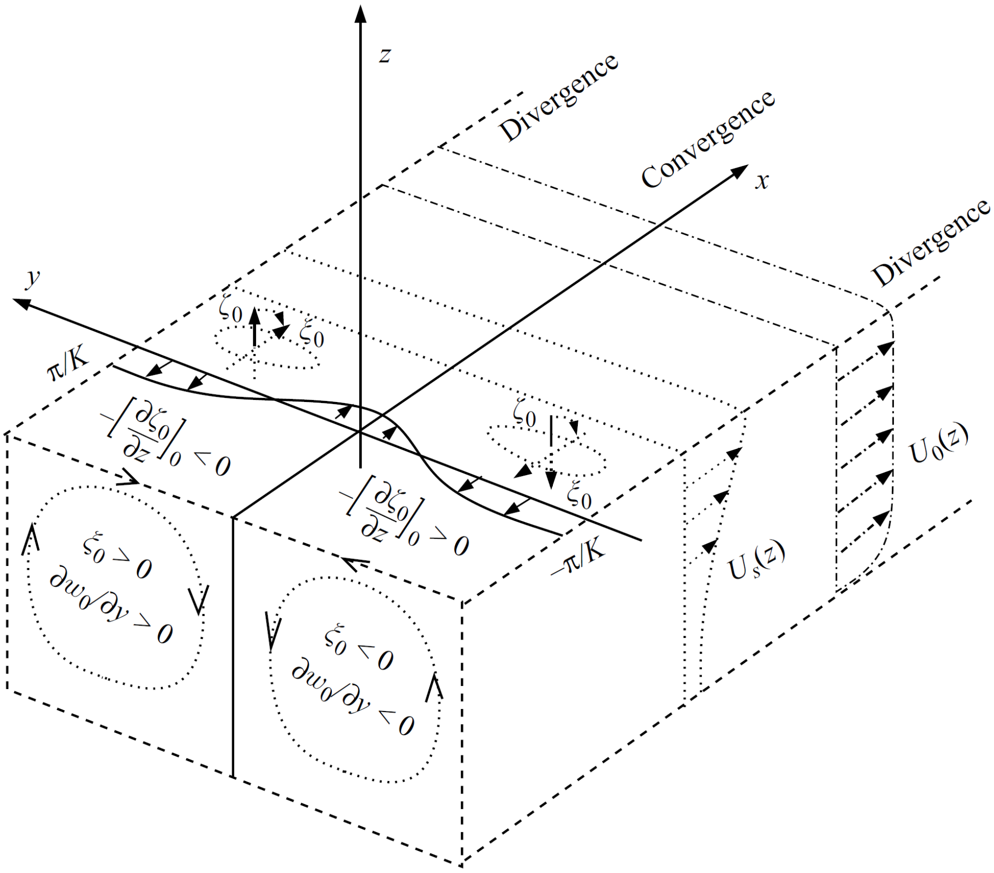

Fig. 3.30 Phenomenology of longitudinal vorticity production in wave-current interaction flows (taken from Huang and Mei (2006)). In particular, U_S is the Stokes drift velocity; U_0 is the mean longitudinal current velocity; w_0 is the vertical velocity; ξ_0 is the longitudinal vorticity; ζ_0 is the vertical vorticity; and K is the dimensionless transverse wave number (it is important to note that Huang and Mei (2006) adopts a different coordinate system compared to the one used in this study, see Fig. 2.6c).

The mathematics underpinning the stability analysis performed by Huang and Mei (2006) is complex but the physical interpretation of the mechanisms leading to the formation of such unstable modes is more straightforward. As in the case of Langmuir turbulence, the key requirements for the production of longitudinal vorticity, and hence of the two unstable modes, are (i) a source of vertical vorticity; and (ii) horizontal shear stress induced by vertical gradients of longitudinal velocities.

According to Huang and Mei (2006), vertical vorticity is introduced by any spanwise perturbation of the longitudinal velocity, imposed e.g. by turbulence. This vertical vorticity then interacts with the Stokes drift shear to generate longitudinal vorticity through vortex tilting and stretching (see Fig. 3.30). The resulting spanwise gradient of the vertical velocity component interacts with the mean shear imposed by the current to generate further vertical vorticity (presumably via vortex stretching) to sustain the whole process of longitudinal vorticity generation.

Unfortunately, since the stability analysis was diagnosed on the $y-z$ plane, Huang and Mei (2006) did not provide clear information about the characteristic longitudinal wavenumber of the detected instabilities and hence it is difficult to compare their theoretical results with the present experimental data (i.e. the wavenumber at which spectral peaks occur in Fig. 3.27c–f). However the recent work by Xuan et al. (2019), indicates that Langmuir turbulence (which is not the one discussed herein and by Huang and Mei (2006), but it does share some similarities) occur in the form of elongated eddies of length eight times their width. Assuming the width of the cells that occur in the present experiments is about h, the estimates provided by Xuan et al. (2019) are close to those of the peak observed at $k_x h = \mathcal{O}(1)$ in Fig. 3.27(c–f). Another difficulty lies in the fact that in the present data large scale structures seem to be bounded within the wave-dominated flow region whereas the instabilities detected by Huang and Mei (2006) cover the entire flow depth. This could be a shortcoming of the linear nature of the equations used by Huang and Mei (2006) or, alternatively, associated with their use of an infinitely large open-channel flow, whereas the flows investigated herein are obviously laterally bounded and this might generate important three-dimensional effects.

More in line with our observations, Huang and Mei (2006) observed that the unstable modes occur only if the wave steepness ϵ is greater than a critical value of 0.02 and the larger the wave steepness the stronger their growth rate. Note that in the experiments presented herein, the wave steepness ϵ is 0.014 (WC−T1) 0.022 (WC−T2), 0.031 (WC−T3), 0.063 (WC−T4) and 0.094 (WC−T5). Except for WC−T1, which does not show signs of these instabilities at low wavenumbers and indeed whose steepness is below 0.02, all remaining cases are characterised by values of ϵ above 0.02 and present evidence of instabilities in line with the modes reported by Huang and Mei (2006) in the wave-dominated flow region. It is also worth noting that WC−T5 is characterised by the highest value of ϵ and the most pronounced spectral peaks at low wavenumbers (see Fig. 3.27f).

To the author's opinion the experimental data presented in this Dissertation provide enough evidence to support the speculative idea that, in the wave-dominated flow region, turbulence is organized in eddies similar to Langmuir cells as argued by Huang and Mei (2006). To the best of the author's knowledge, the present work could be the first to provide evidence of the occurrence of such large turbulence length-scales in combined wave-current flows.

Chapter 4

Conclusions and future works

This Dissertation is devoted to the study of turbulence in smooth-bed open-channel flows. Experiments were carried out in a long laboratory flume able to generate currents and waves superimposed to currents. Longitudinal and vertical velocity components were measured at high sampling frequency by means of a 2-D LDA system that was traversed mainly along the bed-normal coordinate so that vertical profiles of velocity statistics could be obtained and compared among different flow conditions.

Two sets of experiments were carried out: the first devoted to the study of turbulence in unperturbed open-channel flows (i.e. with no superimposed waves). The second devoted to identifying and quantifying the effects of collinear gravity waves on turbulence in open-channel flows.

The two sets of experiments and experimental data were presented and discussed in Chapter 2 and Chapter 3, respectively. These Chapters were written in stand-alone mode, namely as they were two journal papers. Chapter 2 (or more precisely a shorter version of it) has already been published whereas Chapter 3 is on its way to submission.

Despite being two separate pieces of work, the two Chapters do have common research threads. Clearly, the existence of VLSMs and LSMs is a relevant topic that was addressed in both pieces of work, whereby Chapter 2 worked as the benchmark for Chapter 3.

Another common research theme is surely "scaling". Both Chapters address the problem of data collapse pertaining to various velocity statistics, using different characteristic velocity and length-scales. In this context, Chapter 2 is probably still focused on the scaling of LSMs and VLSMs' wavelengths, whereas Chapter 3 addresses scaling in a more general sense (i.e. for a wide range of velocity statistics) in waves plus current flows.

Using the data collected during the flume experiments, the objectives set in Section 1.2 were addressed. These objectives are briefly reported below in ***bold italic*** followed by the key relevant outcomes.

To identify the presence of LSMs and VLSMs in smooth-bed open-channel flows, highlighting the differences compared to canonical wall-flows.

LSM and VLSM's signature is clearly visible in 1-D pre-multiplied spectra of the longitudinal velocity fluctuations. Differently from canonical wall-flows (i.e. boundary layers, pipe or closed-channel flows), the double peak feature persists throughout most of the water column, i.e. over $y/h = 0.8$, while the VLSM footprint appears for von Kármán numbers Re_τ as low as 725.

To study the progressive alteration of LSMs and VLSMs induced by the presence of the side walls, including a comprehensive scaling picture that considers open-channel flows with different aspect ratios.

The VLSM wavelengths and their intensity are reduced as the aspect ratio of the flow decreases, expecially in the outer layer. For what concerns the LSM scaling, no remarkable difference was found with respect to open-channel flows and other wall-flows. Velocity measurements carried at different positions along the spanwise coordinate reveal that both the wavelength and the spectral energy associated with VLSMs depend on the distance from the walls. Also the non-dimensional LSM energy peak decreases in intensity while approaching the sidewall but is not altered in wavenumber until $y/h \approx 0.9$. Since in open-channel flows the shape and intensity of secondary flows vary with the aspect ratio and across the channel cross-section, the results herein reported support the existence of a link between secondary currents and VLSMs, as suggested by Adrian and Marusic (2012) (verbatim from Adrian and Marusic (2012) "the close relationship between meandering VLSMs of turbulence structure research and the long cellular motions of open-channel flow research is impossible to ignore. It seems likely, in fact, that they are one and the same").

It was discovered that the aspect ratio W/h controls the wavelength of VLSMs, whereas the other non-dimensional parameters (Re_τ and x/h) have marginal or negligible effect. The non-dimensional VLSM wavelengths λ_x/h increases as the aspect ratio increases. Differently, the wavelength of LSMs is independent of the non-dimensional parameters considered and scales well with the outer length-scale of the flow h. These results suggest that the two motions may form independently of each other, as previously argued by Cameron et al. (2017).

To assess the effect of gravity waves on turbulence in open-channel flows depending on wave frequencies and amplitudes, with a special focus on:

The scaling of first and second-order velocity statistics.

A novel inner-outer scaling of the vertical profiles of the longitudinal velocity components in combined wave-current flows was presented. The inner length and velocity scales are the usual δ_ν and u_τ (the $u_{\tau_{wc}}$ for the waves plus current cases were determined by the classical Clauser method), while the outer length and velocity scales that allow the velocity profiles to collapse in the overlapping layer are the U_{max} and the elevation h_0 at which U_{max} occurs. It was also found that the position of h_0 depends on the ratio between the vertical wave strength $a\,f_w$ and the vertical motion imposed by the current, which is appropriately represented by u_{τ_c}. A plausible theoretical explanation for the change in the shape of the mean velocity profiles in the presence of the waves was proposed. This change is associated with the covariance between free-surface oscillations and the depth-time-averaged longitudinal velocity fluctuations which takes into account the non-linear interactions between waves and current.

The effects of gravity waves on the wall turbulence were identified by using a innovative signal analysis technique developed by Huang et al. (1998, 1999) for non-stationary time series, i.e. the Empirical Mode Decomposition (EMD). In agreement wiht the literature, a general reduction in turbulent intensities and Reynolds shear stress was revealed by using the classical outer scaling (i.e. using the flow depth h). Successively, the adoption of a new outer length-scale h_0 highlighted that the longitudinal turbulent intensities are dimly affected by the waves, while the vertical turbulent intensities and the Reynolds shear stresses feel the effect of the waves vertical motions, which becomes stronger as $a\, f_w / u_{\tau_c}$ increases. All these second-order moments reach their minimum for $y/h_0 \approx 1$, proving that h_0 is the most appropriate outer length-scale for this type of flows and indicating the presence of two distinct regions in the water column: (i) a current-dominated flow region where the turbulence is produced by shearing ($y/h_0 < 1$); (ii) a wave-dominate flow region where the turbulence is produced by a different mechanism ($y/h_0 > 1$). By considering the results of the spectral analysis, it can be hypothesised that the turbulence in this latter region is a Langmuir-type turbulence.

The fate of LSMs and VLSMs.

The longitudinal 1-D pre-multiplied spectra reveal other interesting results. As the $a\, f_w / u_{\tau_c}$ increases, the spectral footprint of the VLSMs disappears also in the current-dominated flow region. The mechanisms responsible for this suppression are not fully understood and will be a matter of future work. Somewhat unexpectedly, two spectral peaks at wavelengths commensurate to those of LSMs and VLSMs, appears in the wave-dominated flow region and become more pronounced as the wave steepness increases. Their long wavelength and near-surface collocation support the hypothesis that they are Langmuir-type cells argued by the theoretical work of Huang and Mei (2006).

4.1 Recommendations for future studies

Future works should address by creating controlled disturbances on VLSMs or LSMs length-scales and by studying the relative effects. One way to pursue this objective is to vary the characteristics of the bed by using different bed surface roughness and roughness elements (e.g. ridges) similarly to what has been explored by Zampiron et al. (2020). This could lead to new insights into the linkages between LSMs, VLSMs and secondary currents.

Experiments with a turbulent open-channel flow over a bed with increasing hydraulic roughness along the streamwise direction are also worth investigating. These experiments, through measurements of the velocity components in different longitudinal positions, would allow assessing the evolution of the LSMs and VLSMs and their response to different roughness as well as their behaviour in proximity of bed surface discontinuities.

Furthermore, higher aspect ratio in smooth-bed open-channel flow experiments should be considered to gain a global view of the VLSM evolution in open-channel flow (aspect ratio of 12.2 was the upper limit imposed by the flume facility that was used in this study).

The hypothesis of Langmuir-type cells formation in wave-current flows in near shallow water conditions should be verified either by means of PIV measurements or through some other experimental visualization technique (for instance with the addition of dye in the wave-dominated flow region).

Finally, also Eq. (3.26), which was obtained from theoretical arguments, should be verified. To achieve this, PIV measurements of the whole water depth should be used to adequately quantify the importance of the cross-correlation term under different wave conditions.

References

R. J. Adrian. Hairpin vortex organization in wall turbulence. *Phys. Fluids*, 19 (4):041301, 2007.

R. J. Adrian and I. Marusic. Coherent structures in flow over hydraulic engineering surfaces. *J. Hydraul. Res.*, 50(5):451–464, 2012.

R. J. Adrian, C. D. Meinhart, and C. D. Tomkins. Vortex organization in the outer region of the turbulent boundary layer. *J. Fluid Mech.*, 422:1–54, 2000.

H.-E Albrecht, N. Damaschke, M. Borys, and C. Tropea. *Laser Doppler and phase Doppler measurement techniques.* Springer-Verlag, Berlin/Heidelberg, Germany, 2003.

N. N. An and T. Shibayama. Wave-current interaction with mud bed. In *Proc. 24th Int. Conf. Coast. Eng.*, pages 2913–2927. 1994.

K. H. Andersen and C. Faraci. The wave plus current flow over vortex ripples at an arbitrary angle. *Coast. Eng.*, 47(4):431–441, 2003.

M. M. Arnskov, J. Fredsøe, and B. M. Sumer. Bed shear stress measurements over a smooth bed in three-dimensional wave-current motion. *Coast. Eng.*, 20(3-4):277–316, 1993.

C. Auel, I. Albayrak, and R. M. Boes. Turbulence characteristics in supercritical open channel flows: effects of Froude number and aspect ratio. *J. Hydraul. Eng.*, 140(4):04014004, 2014.

F. Bagherimiyab and U. Lemmin. Large-scale coherent flow structures in rough-bed open-channel flow observed in fluctuations of three-dimensional velocity, skin friction and bed pressure. *J. Hydraul. Res.*, 56(6):806–824, 2018.

W. T. Bakker and T. van Doorn. Near-bottom velocities in waves with a current. In *Proc. 16th Int. Conf. Coast. Eng.*, pages 1394–1413. 1978.

B. J. Balakumar and R. J. Adrian. Large-and very-large-scale motions in channel and boundary-layer flows. *Phil. Trans. R. Soc. Lond. A*, 365(1852): 665–681, 2007.

T. Banerjee, M. Muste, and G. G. Katul. Flume experiments on wind induced flow in static water bodies in the presence of protruding vegetation. *Adv. Water Resour.*, 76:11–28, 2015.

K. Barman, S. Roy, and K. Debnath. Wave-current generated turbulence over hemisphere bottom roughness. *Estuar. Coast. Shelf Sci.*, 202:1–17, 2018.

J. H. Bell and R. D. Mehta. Contraction design for small low-speed wind tunnels. *NASA STI/Recon Technical Report N*, 89:13753, 1988.

J. S. Bendat and A. G. Piersol. *Random data: Analysis and measurement procedures (IV Edition).* John Wiley & Sons, New York City, New York, US, 2011.

E. W. Bijker. Some considerations about scales for coastal models with movable bed. *Publ. No. 50, Delft Hydraulic Laboratory*, page 142, 1967.

P. Blondeaux. Turbulent boundary layer at the bottom of gravity waves. *J. Hydraul. Res.*, 25(4):447–464, 1987.

P. Blondeaux. Mechanics of coastal forms. *Annu. Rev. Fluid Mech.*, 33(1): 339–370, 2001.

I. Brevik. Flume experiment on waves and currents II. Smooth bed. *Coast. Eng.*, 4:89–110, 1980.

I. Brevik and B. Aas. Flume experiment on waves and currents. I. Rippled bed. *Coast. Eng.*, 3:149–177, 1980.

G. Calvani, S. Francalanci, and L. Solari. A physical model for the uprooting of flexible vegetation on river bars. *J. Geophys. Res.: Earth Surface*, 124(4): 1018–1034, 2019.

S. M. Cameron, V. I. Nikora, and M. T. Stewart. Very-large-scale motions in rough-bed open-channel flow. *J. Fluid Mech.*, 814:416–429, 2017.

S. M. Cameron, V. I. Nikora, M. T. Stewart, and A. Zampiron. Large and very large scale motions in rough-bed open-channel flow. *E3S Web of Conferences - River Flow 2018*, 40(05061), 2018.

S. M. Cameron, V. I. Nikora, and I. Marusic. Drag forces on a bed particle in open-channel flow: effects of pressure spatial fluctuations and very-large-scale motions. *J. Fluid Mech.*, 863:494–512, 2019.

S. M. Cameron, V. I. Nikora, and M. J. Witz. Entrainment of sediment particles by very large-scale motions. *J. Fluid Mech.*, 888:A7, 2020.

L. Cappietti. Laboratory experiments on the hydrodynamics of waves on adverse currents. In *WIT Transactions on The Built Environment*, volume 70, pages 283–291. 2003.

L. Cappietti. Lattice Boltzmann numerical simulations of wave-current interaction within the boundary layer. In *5th Inter. Conference on Coastal Dynamics*, pages 1–13. 2006.

A. H. Cardoso, W. H. Graf, and G. Gust. Uniform flow in a smooth open channel. *J. Hydraul. Res.*, 27(5):603–616, 1989.

A. H. Cardoso, W. H. Graf, and G. Gust. Steady gradually accelerating flow in a smooth open channel. *J. Hydraul. Res.*, 29(4):525–543, 1991.

G. Caroppi, K. Västilä, J. Järvelä, P. M. Rowiński, and M. Giugni. Turbulence at water-vegetation interface in open channel flow: Experiments with natural-like plants. *Adv. Water. Resour.*, 127:180–191, 2019.

S. Carstensen, B. M. Sumer, and J. Fredsøe. Coherent structures in wave boundary layers. Part 1. oscillatory motion. *J. Fluid Mech.*, 646:169–206, 2010.

M. Cellino and U. Lemmin. Influence of coherent flow structures on the dynamics of suspended sediment transport in open-channel flow. *J. Hydraul. Res.*, 130(11):1077–1088, 2004.

L. P. Chamorro, C. Hill, S. Morton, C. Ellis, R. E. A. Arndt, and F. Sotiropoulos. On the interaction between a turbulent open channel flow and an axial-flow turbine. *J. Fluid Mech.*, 716:658–670, 2013.

L. P. Chamorro, C. Hill, V. S. Neary, B. Gunawan, R. E. A. Arndt, and F. Sotiropoulos. Effects of energetic coherent motions on the power and wake of an axial-flow turbine. *Phys. Fluids*, 27(5):055104, 2015.

F. Charru, B. Andreotti, and P. Claudin. Sand ripples and dunes. *Annu. Rev. Fluid Mech.*, 45:469–493, 2013.

K. A. Chauhan, P. A. Monkewitz, and H. M. Nagib. Criteria for assessing experiments in zero pressure gradient boundary layers. *Fluid Dyn. Res.*, 41 (2):021404, 2009.

J. B. Christoffersen and I. G. Jonsson. Bed friction and dissipation in a combined current and wave motion. *Ocean Eng.*, 12(5):387–423, 1985.

F. H. Clauser. The turbulent boundary layer. *Adv. Appl. Math.*, 4:1–51, 1956.

F. Coscarella, R. Gaudio, and C. Manes. Near-bed eddy scales and clear-water local scouring around vertical cylinders. *J. Hydraul. Res.*, pages 1–14, 2020.

C. Cossu and Y. Hwang. Self-sustaining processes at all scales in wall-bounded turbulent shear flows. *Phil. Trans. R. Soc. Lond. A*, 375(2089):20160088, 2017.

R. K. Cowen and S. Sponaugle. Larval dispersal and marine population connectivity. *Annu. Rev. Mar. Sci.*, 1:443–466, 2009.

A. M. F. da Silva and M. S. Yalin. *Fluvial processes: II Edition.* CRC Press/Balkema, Leiden, The Netherlands, 2017.

Dantec Dynamics. *LDA and PDA - Reference Manual.* Dantec Dynamics A/S, Skovlunde, Denmark, 2011.

B. Dargahi. Controlling mechanism of local scouring. *J. Hydraul. Eng.*, 116 (10):1197–1214, 1990.

B. Dargahi. Experimental study and 3D numerical simulations for a free-overflow spillway. *J. Hydraul. Eng.*, 132(9):899–907, 2006.

A. G. Davies, R. L. Soulsby, and H. L. King. A numerical model of the combined wave and current bottom boundary layer. *J. Geophys. Res.: Oceans*, 93(C1): 491–508, 1988.

D. B. De Graaff and J. K. Eaton. Reynolds-number scaling of the flat-plate turbulent boundary layer. *J. Fluid Mech.*, 422:319–346, 2000.

C. M. de Silva, K. Kevin, R. Baidya, N. Hutchins, and I. Marusic. Large coherence of spanwise velocity in turbulent boundary layers. *J. Fluid Mech.*, 847:161–185, 2018.

A. A. de Souza Machado, K. Spencer, W. Kloas, M. Toffolon, and C. Zarfl. Metal fate and effects in estuaries: a review and conceptual model for better understanding of toxicity. *Sci. Total Environ.*, 541:268–281, 2016.

R. G. Dean and R. A. Dalrymple. *Water Wave Mechanics for Engineers and Scientists*, volume 2. World Scientific, Singapore, 1991.

J. C. del Álamo and J. Jiménez. Spectra of the very large anisotropic scales in turbulent channels. *Phys. Fluids*, 15(6):L41–L44, 2003.

J. C. del Álamo and J. Jiménez. Estimation of turbulent convection velocities and corrections to Taylor's approximation. *J. Fluid Mech.*, 640:5–26, 2009.

S. Dey, S. Sarkar, and L. Solari. Near-bed turbulence characteristics at the entrainment threshold of sediment beds. *J. Hydraul. Eng.*, 137(9):945–958, 2011.

E. Dogan, R. Örlü, D. Gatti, R. Vinuesa, and P. Schlatter. Quantification of amplitude modulation in wall-bounded turbulence. *Fluid Dyn. Res.*, 51(1): 011408, 2019.

D. E. Drake and D. A. Cacchione. Wave-current interaction in the bottom boundary layer during storm and non-storm conditions: observations and model predictions. *Cont. Shelf. Res.*, 12(12):1331–1352, 1992.

Y. Duan, Q. Chen, D. Li, and Q. Zhong. Contributions of very large-scale motions to turbulence statistics in open channel flows. *J. Fluid Mech.*, 892: A3, 2020.

F. Durst, J. Jovanović, and J. Sender. LDA measurements in the near-wall region of a turbulent pipe flow. *J. Fluid Mech.*, 295:305–335, 1995.

K. R. Dyer and R. L. Soulsby. Sand transport on the continental shelf. *Annu. Rev. Fluid Mech.*, 20(1):295–324, 1988.

A. Errico, V. Pasquino, M. Maxwald, G. B. Chirico, L. Solari, and F. Preti. The effect of flexible vegetation on flow in drainage channels: estimation of roughness coefficients at the real scale. *Ecol. Eng.*, 120:411–421, 2018.

A. Errico, G. F. C. Lama, S. Francalanci, G. B. Chirico, L. Solari, and F. Preti. Flow dynamics and turbulence patterns in a drainage channel colonized by common reed (*Phragmites australis*) under different scenarios of vegetation management. *Ecol. Eng.*, 133:39–52, 2019.

M. P. Escudier, A. K. Nickson, and R. J. Poole. Turbulent flow of viscoelastic shear-thinning liquids through a rectangular duct: Quantification of turbulence anisotropy. *J. Nonnewton Fluid. Mech.*, 160(1):2–10, 2009.

C. Faraci, E. Foti, and R. E. Musumeci. Waves plus currents at a right angle: The rippled bed case. *J. Geophys. Res.: Oceans*, 113(C7), 2008.

C. Faraci, P. Scandura, R. E. Musumeci, and E. Foti. Waves plus currents crossing at a right angle: near-bed velocity statistics. *J. Hydraul. Res.*, 56 (4):464–481, 2018.

P. C. Fernando, J. Guo, and P. Lin. Wave–current interaction at an angle 1: experiment. *J. Hydraul. Res.*, 49(4):424–436, 2011a.

P. C. Fernando, P. Lin, and J. Guo. Wave–current interaction at an angle 2: theory. *J. Hydraul. Res.*, 49(4):437–449, 2011b.

H. H. Fernholz and P. J. Finley. The incompressible zero-pressure-gradient turbulent boundary layer: an assessment of the data. *Prog. Aerosp. Sci.*, 32 (4):245–311, 1996.

P. Flandrin, G. Rilling, and P. Goncalves. Empirical Mode Decomposition as a filter bank. *IEEE Signal Process. Lett.*, 11(2):112–114, 2004.

M. J. Franca and M. Brocchini. Turbulence in rivers. In *Rivers–Physical, Fluvial and Environmental Processes*, pages 51–78. Springer-Verlag, Berlin/Heidelberg, Germany, 2015.

M. J. Franca and U. Lemmin. Detection and reconstruction of large-scale coherent flow structures in gravel-bed rivers. *Earth Surf. Process. Landf.*, 40 (1):93–104, 2015.

S. Francalanci, M. Bendoni, M. Rinaldi, and L. Solari. Ecomorphodynamic evolution of salt marshes: Experimental observations of bank retreat processes. *Geomorphology*, 195:53–65, 2013.

J. Fredsøe. Turbulent boundary layer in wave-current motion. *J. Hydraul. Eng.*, 110(8):1103–1120, 1984.

J. Fredsøe and R. Deigaard. *Mechanics of Coastal Sediment Transport*, volume 3. World Scientific, Singapore, 1992.

J. Fredsøe, K. H. Andersen, and B. M. Sumer. Wave plus current over a ripple-covered bed. *Coast. Eng.*, 38(4):177–221, 1999.

B. Ganapathisubramani, E. K. Longmire, and I. Marusic. Characteristics of vortex packets in turbulent boundary layers. *J. Fluid Mech.*, 478:35–46, 2003.

C. B. George and J. F. A. Sleath. Measurements of combined oscillatory and steady flow over a rough bed. *J. Hydraul. Res.*, 17(4):303–313, 1979.

A. Ghesemi, J. Fox, and A. Husic. Predicting macroturbulence energy and timescales for flow over a gravel bed: Experimental results and scaling laws. *Geomorphology*, 332:122–137, 2019.

Y. Goda. *Random Seas and Design of Maritime Structures (III Edition)*, volume 33. World Scientific, Singapore, 2010.

Y. Goda and Y. Suzuki. Estimation of incident and reflected waves in random wave experiments. In *Proc. 15th Int. Conf. Coast. Eng.*, pages 828–845. 1976.

R. A. Grace. Surface wave heights from pressure records. *Coast. Eng.*, 2:55–67, 1978.

S. B. Grant, M. Azizian, P. Cook, F. Boano, and M. A. Rippy. Factoring stream turbulence into global assessments of nitrogen pollution. *Science*, 359 (6381):1266–1269, 2018.

W. D. Grant and O. S. Madsen. Combined wave and current interaction with a rough bottom. *J. Geophys. Res.: Oceans*, 84(C4):1797–1808, 1979.

W. D Grant and O. S. Madsen. The continental-shelf bottom boundary layer. *Annu. Rev. Fluid Mech.*, 18(1):265–305, 1986.

D. I. Grinvald and V. I. Nikora. *River turbulence.* Hydrometeoizdat, Leningrad, Russia, 1988.

J. Groeneweg and J. A. Battjes. Three-dimensional wave effects on a steady current. *J. Fluid Mech.*, 478:325–343, 2003.

J. Groeneweg and G. Klopman. Changes of the mean velocity profiles in the combined wave–current motion described in a GLM formulation. *J. Fluid Mech.*, 370:271–296, 1998.

C. E. Grosch, L. W. Ward, and S. J. Lukasik. Viscous dissipation of shallow water waves. *Phys. Fluids*, 3(3):477–479, 1960.

M. Guala, S. E. Hommema, and R. J. Adrian. Large-scale and very-large-scale motions in turbulent pipe flow. *J. Fluid Mech.*, 554:521–542, 2006.

J. S. Guasto, R. Rusconi, and R. Stocker. Fluid mechanics of planktonic microorganisms. *Annu. Rev. Fluid Mech.*, 44:373–400, 2012.

E. E. Hackett, L. Luznik, A. R. Nayak, J. Katz, and T. R. Osborn. Field measurements of turbulence at an unstable interface between current and wave bottom boundary layers. *J. Geophys. Res.: Oceans*, 116(C2), 2011.

S. Hallegatte, C. Green, R. J. Nicholls, and J. Corfee-Morlot. Future flood losses in major coastal cities. *Nat. Clim. Change*, 3(9):802–806, 2013.

C. A. Hannan. Planktonic larvae may act like passive particles in turbulent near-bottom flows. *Limnol. Oceanogr.*, 29(5):1108–1116, 1984.

M. He, X. F. Gao, and W. H. Xu. Numerical simulation of wave-current interaction using the SPH method. *J. Hydrodynam.*, 30(3):535–538, 2018.

T. S. Hedges. Regions of validity of analytical wave theories. In *Proc. of the Institution of Civil Engineers–Water, Maritime and Energy*, pages 111–114. 1995.

F. M. Henderson. *Open channel flow.* Macmillan Publishing Co. Inc, New York City, New York, US, 1966.

L. E. Holmedal, D. Myrhaug, and H. Rue. The sea bed boundary layer under random waves plus current. *Cont. Shelf Res.*, 23(7):717–750, 2003.

S. Hommema and R. Adrian. Similarity of apparently random structures in the outer region of wall turbulence. *Exp. Fluids*, 33(1):5–12, 2002.

S. Hoyas and J. Jiménez. Scaling of the velocity fluctuations in turbulent channels up to $Re_\tau = 2003$. *Phys. Fluids*, 18(1):011702, 2006.

N. E. Huang and Z. Wu. A review on Hilbert-Huang transform: Method and its applications to geophysical studies. *Reviews of geophysics*, 46(2), 2008.

N. E. Huang, Z. Shen, S. R. Long, M. C. Wu, H. H. Shih, Q. Zheng, N. C. Yen, C. C. Tung, and H. H. Liu. The empirical mode decomposition and the Hilbert spectrum for nonlinear and non-stationary time series analysis. *Proc. R. Soc. Lond. A*, 454(1971):903–995, 1998.

N. E. Huang, Z. Shen, and S. R. Long. A new view of nonlinear water waves: the Hilbert spectrum. *Annu. Rev. Fluid Mech.*, 31(1):417–457, 1999.

N. E. Huang, M. C. Wu, S. R. Long, S. S. P. Shen, W. Qu, P. Gloersen, and K. L. Fan. A confidence limit for the empirical mode decomposition and hilbert spectral analysis. *Proc. R. Soc. Lond. A*, 459(2037):2317–2345, 2003.

Y. X. Huang, F. G. Schmitt, Z. M. Lu, and Y. L. Liu. Analysis of daily river flow fluctuations using empirical mode decomposition and arbitrary order Hilbert spectral analysis. *J. Hydrol.*, 373(1-2):103–111, 2009.

Y. X. Huang, F. G. Schmitt, Z. M. Lu, P. Fougairolles, Y. Gagne, and Y. L. Liu. Second-order structure function in fully developed turbulence. *Phys. Rev. E*, 82(2):026319, 2010.

Z. Huang and C. C. Mei. Effects of surface waves on a turbulent current over a smooth or rough seabed. *J. Fluid Mech.*, 497:253–287, 2003.

Z. Huang and C. C. Mei. Wave-induced longitudinal vortices in a shallow current. *J. Fluid Mech.*, 551:323–356, 2006.

M. Huettel, P. Berg, and J. E. Kostka. Benthic exchange and biogeochemical cycling in permeable sediments. *Annu. Rev. Mar. Sci.*, 6:23–51, 2014.

M. Hultmark, M. Vallikivi, S. C. C. Bailey, and A. J. Smits. Turbulent pipe flow at extreme Reynolds numbers. *Phys. Rev. Lett.*, 108(9):094501, 2012.

C. J. Humbyrd. *Turbulent combined wave-current boundary layer model for application in coastal waters.* MSc Thesis, Massachusetts Institute of Technology (MIT), Cambridge, Massachusetts, US, 2012.

J. C. R. Hunt and P. A. Durbin. Perturbed vortical layers and shear sheltering. *Fluid. Dyn. Res.*, 24(6):375, 1999.

J. N. Hunt. Viscous damping of waves over an inclined bed in a channel of finite width. *Houille Blanche*, pages 836–842, 1952.

D. Hurther, U. Lemmin, and E. A. Terray. Turbulent transport in the outer region of rough-wall open-channel flows: the contribution of large coherent shear stress structures (LC3S). *J. Fluid Mech.*, 574:465–493, 2007.

A. K. M. F. Hussain. Coherent structures and turbulence. *J. Fluid Mech.*, 173: 303–356, 1986.

A. K. M. F. Hussain and W. C. Reynolds. The mechanics of an organized wave in turbulent shear flow. *J. Fluid Mech.*, 41(2):241–258, 1970.

N. Hutchins and I. Marusic. Evidence of very long meandering features in the logarithmic region of turbulent boundary layers. *J. Fluid Mech.*, 579:1–28, 2007a.

N. Hutchins and I. Marusic. Large-scale influences in near-wall turbulence. *Phil. Trans. R. Soc. Lond. A*, 365(1852):647–664, 2007b.

N. Hutchins, W. T. Hambleton, and I. Marusic. Inclined cross-stream stereo particle image velocimetry measurements in turbulent boundary layers. *J. Fluid Mech.*, 541:21–54, 2005.

N. Hutchins, T. B. Nickels, I. Marusic, and M. S. Chong. Hot-wire spatial resolution issues in wall-bounded turbulence. *J. Fluid Mech.*, 635:103–136, 2009.

Y. Hwang and Y. Bengana. Self-sustaining process of minimal attached eddies in turbulent channel flow. *J. Fluid Mech.*, 795:708–738, 2016.

Y. Hwang and C. Cossu. Self-sustained process at large scales in turbulent channel flow. *Phys. Rev. Lett.*, 105(4):044505, 2010.

Y. Hwang, A. P. Willis, and C. Cossu. Invariant solutions of minimal large-scale structures in turbulent channel flow for Re_τ up to 1000. *J. Fluid Mech.*, 802, 2016.

M. Isaacson. Measurement of regular wave reflection. *J. Waterw. Port Coast. Oc. Eng.*, 117(6):553–569, 1991.

R. G. Jackson. Sedimentological and fluid-dynamic implications of the turbulent bursting phenomenon in geophysical flows. *J. Fluid Mech.*, 77(3):531–560, 1976.

J. Jiménez. Coherent structures in wall-bounded turbulence. *J. Fluid Mech.*, 842, 2018.

G. H. Jirka, H. Herlina, and A. Niepelt. Gas transfer at the air–water interface: Experiments with different turbulence forcing mechanisms. *Exp. Fluids*, 49 (1):319–327, 2010.

G. G. Katul. The anatomy of large-scale motion in atmospheric boundary layers. *J. Fluid Mech.*, 858:1–4, 2019.

P. H. Kemp and R. R. Simons. The interaction between waves and a turbulent current: waves propagating with the current. *J. Fluid Mech.*, 116:227–250, 1982.

P. H. Kemp and R. R. Simons. The interaction of waves and a turbulent current: waves propagating against the current. *J. Fluid Mech.*, 130:73–89, 1983.

K. Kevin, J. Monty, and N. Hutchins. The meandering behaviour of large-scale structures in turbulent boundary layers. *J. Fluid Mech.*, 865, 2019.

H. Kim, B. A. O'Connor, I. Park, and Y. Lee. Modeling effect of intersection angle on near-bed flows for waves and currents. *J. Waterw. Port Coast. Oc. Eng.*, 127(6):308–318, 2001.

K. C. Kim and R. J. Adrian. Very large-scale motion in the outer layer. *Phys. Fluids*, 11(2):417–422, 1999.

M. S. Kirkgöz. Particle velocity prediction at the transformation point of plunging breakers. *Coast. Eng.*, 10(2):139–147, 1986.

M. S. Kirkgöz. Turbulent velocity profiles for smooth and rough open channel flow. *J. Hydraul. Eng.*, 115(11):1543–1561, 1989.

M. S. Kirkgöz and M. Ardiçlioğlu. Velocity profiles of developing and developed open channel flow. *J. Hydraul. Eng.*, 123(12):1099–1105, 1997.

B. A. Kironoto. The universality of the Kàrmàn constant on non-uniform open-channel flow. In *11th Cong. of APD-IAHR*, pages 579–586. 1998.

B. A. Kironoto and W. H. Graf. Turbulence characteristics in rough non-uniform open-channel flow. In *Proc. of the Institution of Civil Engineers – Water, Maritime and Energy*, pages 336–348. 1995.

G. Klopman. Vertical structure of the flow due to waves and currents. *Progress Rep. No. H840. 30, Part II, Delft Hydraulic Laboratory*, 1994.

D. W. Knight, J. D. Demetriou, and M. E. Hamed. Boundary shear in smooth rectangular channels. *J. Hydraul. Eng.*, 110(4):405–422, 1984.

J. R. W. Lacey and A. G. Roy. Fine-scale characterization of the turbulent shear layer of an instream pebble cluster. *J. Hydraul. Eng.*, 134(7):925–936, 2008.

K. Y. Lim and O. S. Madsen. An experimental study on near-orthogonal wave–current interaction over smooth and uniform fixed roughness beds. *Coast. Eng.*, 116:258–274, 2016.

C. R. Lodahl, B. M. Sumer, and J. Fredsøe. Turbulent combined oscillatory flow and current in a pipe. *J. Fluid Mech.*, 373:313–348, 1998.

F. López and M. H. García. Wall similarity in turbulent open-channel flow. *J. Eng. Mech.*, 125(7):789–796, 1999.

H. Lundgren. Turbulent currents in the presence of waves. In *Proc. 13th Int. Conf. Coast. Eng.*, pages 623–634. 1972.

O. S. Madsen. Spectral wave-current bottom boundary layer flows. In *Proc. 24th Int. Conf. Coast. Eng.*, pages 384–398. 1994.

O. S. Madsen and W. D. Grant. Quantitative description of sediment transport by waves. In *Proc. 15th Int. Conf. Coast. Eng.*, pages 1092–1112. 1976.

C. Manes, D. Pokrajac, and I. McEwan. Double-averaged open-channel flows with small relative submergence. *J. Hydraul. Eng.*, 133(8):896–904, 2007.

C. Manes, D. Poggi, and L. Ridolfi. Turbulent boundary layers over permeable walls: scaling and near-wall structure. *J. Fluid Mech.*, 687:141–170, 2011.

M. Marino, I. C. Rabionet, R. E. Musumeci, and E. Foti. Reliability of pressure sensors to measure wave height in the shoaling region. *Proc. 36th Int. Conf. Coast. Eng.*, (36):10–10, 2018.

I. Marusic and J. P. Monty. Attached eddy model of wall turbulence. *Annu. Rev. Fluid Mech.*, 51:49–74, 2019.

I. Marusic, B. J. McKeon, P. A. Monkewitz, H. M. Nagib, A. J. Smits, and K. R. Sreenivasan. Wall-bounded turbulent flows at high Reynolds numbers: recent advances and key issues. *Phys. Fluids*, 22(6):065103, 2010.

I. Marusic, J. P. Monty, M. Hultmark, and A. J. Smits. On the logarithmic region in wall turbulence. *J. Fluid Mech.*, 716, 2013.

P. P. Mathisen and O. S. Madsen. Waves and currents over a fixed rippled bed: 1. Bottom roughness experienced by waves in the presence and absence of currents. *J. Geophys. Res.: Oceans*, 101(C7):16533–16542, 1996a.

P. P. Mathisen and O. S. Madsen. Waves and currents over a fixed rippled bed: 2. Bottom and apparent roughness experienced by currents in the presence of waves. *J. Geophys. Res.: Oceans*, 101(C7):16543–16550, 1996b.

P. P. Mathisen and O. S. Madsen. Waves and currents over a fixed rippled bed: 3. Bottom and apparent roughness for spectral waves and currents. *J. Geophys. Res.: Oceans*, 104(C8):18447–18461, 1999.

B. S. Mazumder and S. P. Ojha. Turbulence statistics of flow due to wave–current interaction. *Flow Meas. Instrum.*, 18(3-4):129–138, 2007.

S. McCrary. Implementing algorithms to measure common statistics. *White Paper - Berkeley Research Grup (BRG)*, pages 1–18, 2015.

B. J. McKeon and J. F. Morrison. Asymptotic scaling in turbulent pipe flow. *Phil. Trans. R. Soc. Lond. A*, 365(1852):771–787, 2007.

M. Melis, D. Poggi, G. O. D. Fasanella, S. Cordero, and G. G. Katul. Resistance to flow on a sloping channel covered by dense vegetation following a dam break. *Water Resour. Res.*, 55(2):1040–1058, 2019.

C. Meneveau and I. Marusic. Generalized logarithmic law for high-order moments in turbulent boundary layers. *J. Fluid Mech.*, 719, 2013.

J. P. Monty, J. A. Stewart, R. C. Williams, and M. S. Chong. Large-scale features in turbulent pipe and channel flows. *J. Fluid Mech.*, 589:147–156, 2007.

J. P. Monty, N. Hutchins, H. C. H. Ng, I. Marusic, and M. S. Chong. A comparison of turbulent pipe, channel and boundary layer flows. *J. Fluid Mech.*, 632:431–442, 2009.

D. B. Moog and G. H. Jirka. Air-water gas transfer in uniform channel flow. *J. Hydraul. Eng.*, 125(1):3–10, 1999.

J. F. Morrison, B. J. McKeon, W. Jiang, and A. J. Smits. Scaling of the streamwise velocity component in turbulent pipe flow. *J. Fluid Mech.*, 508: 99–131, 2004.

R. E. Musumeci, L. Cavallaro, E. Foti, P. Scandura, and P. Blondeaux. Waves plus currents crossing at a right angle: Experimental investigation. *J. Geophys. Res.: Oceans*, 111(C7), 2006.

D. Myrhaug. A theoretical model of combined wave and current boundary layers near a rough sea bottom. In *Proc. 3rd Offshore Mechanics and Arctic Eng.*, pages 559–568, 1984.

D. Myrhaug and O. H. Slaattelid. A rational approach to wave-current friction coefficients for rough, smooth and transitional turbulent flow. *Coast. Eng.*, 14(3):265–293, 1990.

H. Nakagawa and I. Nezu. Prediction of the contributions to the reynolds stress from bursting events in open-channel flows. *J. Fluid Mech.*, 80(1):99–128, 1977.

H. Nakagawa and I. Nezu. Structure of space-time correlations of bursting phenomena in an open-channel flow. *J. Fluid Mech.*, 104:1–43, 1981.

A. R. Nayak, C. Li, B. T. Kiani, and J. Katz. On the wave and current interaction with a rippled seabed in the coastal ocean bottom boundary layer. *J. Geophys. Res.: Oceans*, 120(7):4595–4624, 2015.

H. M. Nepf. Flow and transport in regions with aquatic vegetation. *Annu. Rev. Fluid Mech.*, 44:123–142, 2012.

B. Neumann, A. T. Vafeidis, J. Zimmermann, and R. J. Nicholls. Future coastal population growth and exposure to sea-level rise and coastal flooding – A global assessment. *PLoS One*, 10(3):e0118571, 2015.

I. Nezu. Open-channel flow turbulence and its research prospect in the 21st century. *J. Hydraul. Eng.*, 131(4):229–246, 2005.

I. Nezu and H. Nakagawa. *Turbulence in Open-Channel Flows.* A. A. Balkema, Rotterdam, The Netherlands, 1993.

I. Nezu and W. Rodi. Open-channel flow measurements with a Laser Doppler Anemometer. *J. Hydraul. Eng.*, 112(5):335–355, 1986.

P. Nielsen. *Coastal Bottom Boundary Layers and Sediment Transport*, volume 4. World Scientific, Singapore, 1992.

V. I. Nikora and D. Goring. Eddy convection velocity and Taylor's hypothesis of 'frozen' turbulence in a rough-bed open-channel flow. *J. Hydrosci. Hydraul. Eng.*, 18(2):75–91, 2000a.

V. I. Nikora and D. Goring. Flow turbulence over fixed and weakly mobile gravel beds. *J. Hydraul. Eng.*, 126(9):679–690, 2000b.

M. Olabarrieta, R. Medina, and S. Castanedo. Effects of wave–current interaction on the current profile. *Coast. Eng.*, 57(7):643–655, 2010.

K. Onitsuka, J. Akiyama, and S. Matsuoka. Prediction of velocity profiles and reynolds stress distributions in turbulent open-channel flows with adverse pressure gradient. *J. Hydraul. Res.*, 47(1):58–65, 2009.

R. Örlü, T. Fiorini, A. Segalini, G. Bellani, A. Talamelli, and P. H. Alfredsson. Reynolds stress scaling in pipe flow turbulence — first results from CICLoPE. *Phil. Trans. R. Soc. Lond. A*, 375(2089):20160187, 2017.

T. Pähtz, A. H. Clark, M. Valyrakis, and O. Durán. The physics of sediment transport initiation, cessation, and entrainment across aeolian and fluvial environments. *Rev. Geophys.*, page e2019RG000679, 2020.

A. E. Perry and M. S. Chong. On the mechanism of wall turbulence. *J. Fluid Mech.*, 119:173–217, 1982.

A. E. Perry, S. Henbest, and M. S. Chong. A theoretical and experimental study of wall turbulence. *J. Fluid Mech.*, 165:163–199, 1986.

C. Peruzzi, D. Poggi, L. Ridolfi, and C. Manes. On the scaling of large-scale structures in smooth-bed turbulent open-channel flows. *J. Fluid Mech.*, 889: A1, 2020.

A. T. Piper, C. Manes, F. Siniscalchi, A. Marion, R. M. Wright, and P. S. Kemp. Response of seaward-migrating European eel (*Anguilla anguilla*) to manipulated flow fields. *Proc. R. Soc. Lond. B*, 282(1811):20151098, 2015.

D. Poggi, A. Porporato, and L. Ridolfi. An experimental contribution to near-wall measurements by means of a special Laser Doppler Anemometry technique. *Exp. Fluids*, 32(3):366–375, 2002.

D. Poggi, A. Porporato, and L. Ridolfi. Analysis of the small-scale structure of turbulence on smooth and rough walls. *Phys. Fluids*, 15(1):35–46, 2003.

D. Poggi, G. G. Katul, J. D. Albertson, and L. Ridolfi. An experimental investigation of turbulent flows over a hilly surface. *Phys. Fluids*, 19(3): 036601, 2007.

S. B. Pope. *Turbulent flows.* Cambridge University Press, Cambridge, UK, 2000.

A. Porporato and L. Ridolfi. Some dynamical properties of a differential model for the bursting cycle in the near-wall turbulence. *Phys. Fluids*, 14(12): 4278–4283, 2002.

S. Proust and V. I. Nikora. Compound open-channel flows: effects of transverse currents on the flow structure. *J. Fluid Mech.*, 885:A24, 2020.

J. H. Pu, S. Tait, Y. Guo, Y. Huang, and P. R. Hanmaiahgari. Dominant features in three-dimensional turbulence structure: comparison of non-uniform accelerating and decelerating flows. *Environ. Fluid Mech.*, 18(2):395–416, 2018.

W. G. Qi, C. F. Li, D. S. Jeng, F. P. Gao, and Z. Liang. Combined wave-current induced excess pore-pressure in a sandy seabed: Flume observations and comparisons with theoretical models. *Coast. Eng.*, 147:89–98, 2019.

F. Qiao, Y. Yuan, J. Deng, D. Dai, and Z. Song. Wave–turbulence interaction-induced vertical mixing and its effects in ocean and climate models. *Phil. Trans. R. Soc. Lond. A*, 374(2065):20150201, 2016.

E. Quaranta, C. Katopodis, R. Revelli, and C. Comoglio. Turbulent flow field comparison and related suitability for fish passage of a standard and a simplified low-gradient vertical slot fishway. *River. Res. Appl.*, 33(8): 1295–1305, 2017.

M. Rashidi. Burst–interface interactions in free surface turbulent flows. *Phys. Fluids*, 9(11):3485–3501, 1997.

M. Rashidi and S. Banerjee. Turbulence structure in free-surface channel flows. *Phys. Fluids*, 31(9):2491–2503, 1988.

R. T. Rato, M. D. Ortigueira, and A. G. Batista. On the HHT, its problems, and some solutions. *Mech. Syst. Signal. Process.*, 22(6):1374–1394, 2008.

S. Rawat, C. Cossu, Y. Hwang, and F. Rincon. On the self-sustained nature of large-scale motions in turbulent Couette flow. *J. Fluid Mech.*, 782:515–540, 2015.

A. Robinson, D. Ingram, I. Bryden, and T. Bruce. The effect of inlet design on the flow within a combined waves and current flumes, test tank and basins. *Coast. Eng.*, 95:117–129, 2015.

S. K. Robinson. Coherent motions in the turbulent boundary layer. *Annu. Rev. Fluid Mech.*, 23(1):601–639, 1991.

J. F. Rodríguez and M. H. García. Laboratory measurements of 3-D flow patterns and turbulence in straight open channel with rough bed. *J. Hydraul. Res.*, 46(4):454–465, 2008.

E. Rodríguez-López, P. J. K. Bruce, and O. R. H. Buxton. A robust post-processing method to determine skin friction in turbulent boundary layers from the velocity profile. *Exp. Fluids*, 56(4):68, 2015.

V. Roussinova, N. Biswas, and R. Balachandar. Revisiting turbulence in smooth uniform open channel flow. *J. Hydraul. Res.*, 46(sup1):36–48, 2008.

A. G. Roy, T. Buffin-Belanger, H. Lamarre, and A. D. Kirkbride. Size, shape and dynamics of large-scale turbulent flow structures in a gravel-bed river. *J. Fluid Mech.*, 500:1–27, 2004.

S. Roy, K. Debnath, and B. S. Mazumder. Distribution of eddy scales for wave current combined flow. *Appl. Ocean Res.*, 63:170–183, 2017.

S. Roy, S. S. Samantaray, and K. Debnath. Study of turbulent eddies for wave against current. *Ocean Eng.*, 150:176–193, 2018.

F. G. Schmitt, Y. X. Huang, Z. M. Lu, Y. L. Liu, and N. Fernandez. Analysis of velocity fluctuations and their intermittency properties in the surf zone using empirical mode decomposition. *J. Mar. Syst.*, 77(4):473–481, 2009.

W. J. Shaw and J. H. Trowbridge. The direct estimation of near-bottom turbulent fluxes in the presence of energetic wave motions. *J. Atmos. Ocean. Technol.*, 18(9):1540–1557, 2001.

C. Shen and U. Lemmin. Application of an acoustic particle flux profiler in particleladen open-channel flow. *J. Hydraul. Res.*, 37(3):407–419, 1999.

L. Shen, X. Zhang, D. K. P. Yue, and G. S. Triantafyllou. The surface layer for free-surface turbulent flows. *J. Fluid Mech.*, 386:167–212, 1999.

A. B. Shvidchenko and G. Pender. Macroturbulent structure of open-channel flow over gravel beds. *Water Resour. Res.*, 37(3):709–719, 2001.

J. A. Sillero, J. Jiménez, and R. D. Moser. Two-point statistics for turbulent boundary layers and channels at Reynolds numbers up $\delta^+ \approx 2000$. *Phys. Fluids*, 26(10):105109, 2014.

R. R. Simons, T. J. Grass, and M. Mansour-Tehrani. Bottom shear stresses in the boundary layers under waves and currents crossing at right angles. In *Proc. 23th Int. Conf. Coast. Eng.*, pages 604–617. 1992.

R. R. Simons, T. J. Grass, W. M. Saleh, and M. Mansour-Tehrani. Bottom shear stresses under random waves with a current superimposed. In *Proc. 24th Int. Conf. Coast. Eng.*, pages 565–578. 1994.

S. K. Singh and K. Debnath. Combined effects of wave and current in free surface turbulent flow. *Ocean Eng.*, 127:170–189, 2016.

S. K. Singh, K. Debnath, and B. S. Mazumder. Spatially-averaged turbulent flow over cubical roughness in wave-current co-existing environment. *Coast. Eng.*, 114:77–85, 2016.

A. J. Smits, B. J. McKeon, and I. Marusic. High–Reynolds number wall turbulence. *Annu. Rev. Fluid Mech.*, 43:353–375, 2011.

L. Soldini, A. Piattella, A. Mancinelli, R. Bernetti, and M. Brocchini. Macrovortices–induced horizontal mixing in compound channels. *Ocean Dyn.*, 54(3-4):333–339, 2004.

T. Song and Y. M. Chiew. Turbulence measurement in nonuniform open-channel flow using Acoustic Doppler Velocimeter (ADV). *J. Eng. Mech.*, 127 (3):219–232, 2001.

R. L. Soulsby. Simplified calculation of wave orbital velocities. *Report TR 155, HR Wallingford*, 2006.

R. L. Soulsby, L. Hamm, G. Klopman, D. Myrhaug, R. R. Simons, and G. P. Thomas. Wave-current interaction within and outside the bottom boundary layer. *Coast. Eng.*, 21(1-3):41–69, 1993.

P. M. Steffler, N. Rajaratnam, and A. W. Peterson. LDA measurements in open channel. *J. Hydraul. Res.*, 111(1):119–130, 1985.

A. Stocchino and M. Brocchini. Horizontal mixing of quasi-uniform straight compound channel flows. *J. Fluid Mech.*, 643:425–435, 2010.

A. Stocchino, G. Besio, S. Angiolani, and M. Brocchini. Lagrangian mixing in straight compound channels. *J. Fluid Mech.*, 675:168–198, 2011.

A. N. Sukhodolov, V. I. Nikora, and V. M. Katolikov. Flow dynamics in alluvial channels: the legacy of Kirill V. Grishanin. *J. Hydraul. Res.*, 49(3):285–292, 2011.

B. M. Sumer. Flow–structure–seabed interactions in coastal and marine environments. *J. Hydraul. Res.*, 52(1):1–13, 2014.

B. M. Sumer, T. U. Petersen, L. Locatelli, J. Fredsøe, R. E. Musumeci, and E. Foti. Backfilling of a scour hole around a pile in waves and current. *J. Waterw. Port Coast. Oc. Eng.*, 139(1):9–23, 2013.

S. Supharatid, H. Tanaka, and N. Shuto. Interaction of nonlinear wave and current. In *Proc. 23th Int. Conf. Coast. Eng.*, pages 672–683. 1993.

A. A. Tabrizi, L. Garibaldi, A. Fasana, and S. Marchesiello. Influence of stopping criterion for sifting process of empirical mode decomposition (EMD) on roller bearing fault diagnosis. In *Advances in Condition Monitoring of Machinery in Non-Stationary Operations*, pages 389–398. Springer-Verlag, Berlin/Heidelberg, Germany, 2014.

N. Tambroni, P. Blondeaux, and G. Vittori. A simple model of wave–current interaction. *J. Fluid Mech.*, 775:328–348, 2015.

N. Tambroni, J. F. da Silva, R. W. Duck, S. J. McLelland, C. Venier, and S. Lanzoni. Experimental investigation of the impact of macroalgal mats on the wave and current dynamics. *Adv. Water Resour.*, 93:326–335, 2016.

A. Tamburrino and J. S. Gulliver. Large flow structures in a turbulent open channel flow. *J. Hydraul. Res.*, 37(3):363–380, 1999.

G. I. Taylor. The spectrum of turbulence. *Proc. R. Soc. Lond. A*, 164(919): 476–490, 1938.

H. Tennekes and J. L. Lumley. *A first course in turbulence.* MIT Press, Boston, Massachusetts, US, 1972.

A. Tominaga and I. Nezu. Velocity profiles in steep open-channel flows. *J. Hydraul. Eng.*, 118(1):73–90, 1992.

A. Tominaga, I. Nezu, K. Ezaki, and H. Nakagawa. Three-dimensional turbulent structure in straight open channel flows. *J. Hydraul. Res.*, 27(1):149–173, 1989.

C. D. Tomkins and R. J. Adrian. Spanwise structure and scale growth in turbulent boundary layers. *J. Fluid Mech.*, 490:37–74, 2003.

A. A. Townsend. Equilibrium layers and wall turbulence. *J. Fluid Mech.*, 11 (1):97–120, 1961.

A. A. Townsend. *The structure of turbulent shear flow (II Edition).* Cambridge University Press, Cambridge, UK, 1976.

G. Trinci, G. L. Harvey, A. J. Henshaw, W. Bertoldi, and F. Hölker. Life in turbulent flows: interactions between hydrodynamics and aquatic organisms in rivers. *Wiley Interdiscip. Rev.: Water*, 4(3):e1213, 2017.

C. Tropea, A. L. Yarin, and J. F. Foss. *Springer handbook of experimental fluid mechanics.* Springer-Verlag, Berlin/Heidelberg, Germany, 2007.

J. H. Trowbridge and S. J. Lentz. The bottom boundary layer. *Annu. Rev. Mar. Sci.*, 10:397–420, 2018.

J. H. Trowbridge and O. S. Madsen. Turbulent wave boundary layers: 1. Model formulation and first-order solution. *J. Geophys. Res.: Oceans*, 89 (C5):7989–7997, 1984a.

J. H. Trowbridge and O. S. Madsen. Turbulent wave boundary layers: 2. Second-order theory and mass transport. *J. Geophys. Res.: Oceans*, 89(C5): 7999–8007, 1984b.

M. Umeyama. Reynolds stresses and velocity distributions in a wave-current coexisting environment. *J. Waterw. Port Coast. Oc. Eng.*, 131(5):203–212, 2005.

M. Umeyama. Mean velocity changes due to interaction between bichromatic waves and a current. *J. Waterw. Port Coast. Oc. Eng.*, 135(1):11–23, 2009a.

M. Umeyama. Changes in turbulent flow structure under combined wave-current motions. *J. Waterw. Port Coast. Oc. Eng.*, 135(5):213–227, 2009b.

M. Umeyama. Coupled PIV and PTV measurements of particle velocities and trajectories for surface waves following a steady current. *J. Waterw. Port Coast. Oc. Eng.*, 137(2):85–94, 2011.

W. Van Balen, W. S. J. Uijttewaal, and K. Blanckaert. Large-eddy simulation of a mildly curved open-channel flow. *J. Fluid Mech.*, 630:413–442, 2009.

T. van Doorn. Experimental investigation of near-bottom velocities in water waves without and with a current. *Report on Investigation M1423, Delft Hydraulic Laboratory*, 1981.

J. D. A. van Hoften and S. Karaki. Interaction of waves and a turbulent current. In *Proc. 15th Int. Conf. Coast. Eng.*, pages 404–422. 1977.

C. Vanderwel and B. Ganapathisubramani. Turbulent boundary layers over multiscale rough patches. *Bound.-Layer Meteorol.*, 172(1):1–16, 2019.

J. G. Venditti, J. L. Best, M. Church, and R. J. Hardy. *Coherent Flow Structures at Earth's Surface.* John Wiley & Sons, Chichester, UK, 2013.

D. Vettori. *Hydrodynamic performance of seaweed farms: an experimental study at seaweed blade scale.* PhD thesis, University of Aberdeen, 2016.

D. Vettori and V. I. Nikora. Flow-seaweed interactions of *Saccharina latissima* at a blade scale: turbulence, drag force, and blade dynamics. *Aquat. Sci.*, 81 (4):61, 2019.

P. J. Visser. Wave basin experiments on bottom friction due to current and waves. In *Proc. 20th Int. Conf. Coast. Eng.*, pages 807–821. 1987.

J. M. Wallace. Quadrant analysis in turbulence research: history and evolution. *Annu. Rev. Fluid Mech.*, 48:131–158, 2016.

J. M. Wallace, H. Eckelmann, and R. S. Brodkey. The wall region in turbulent shear flow. *J. Fluid Mech.*, 54(1):39–48, 1972.

G. Wang and D. H. Richter. Two mechanisms of modulation of very-large-scale motions by inertial particles in open channel flow. *J. Fluid Mech.*, 868: 538–559, 2019.

Z. Q. Wang and N. S. Cheng. Secondary flows over artificial bed strips. *Adv. Water Resour.*, 28(5):441–450, 2005.

T. Wei and W. Willmarth. Reynolds-number effects on the structure of a turbulent channel flow. *J. Fluid Mech.*, 204:57–95, 1989.

L. Xinyu, C. Changzhi, and D. Zengnan. Turbulent flows in smooth-wall open channels with different slope. *J. Hydraul. Res.*, 33(3):333–347, 1995.

A. Xuan, B. Q. Deng, and L. Shen. Study of wave effect on vorticity in Langmuir turbulence using wave-phase-resolved large-eddy simulation. *J. Fluid Mech.*, 875:173–224, 2019.

A. M. Yaglom. Similarity laws for constant-pressure and pressure-gradient turbulent wall flows. *Annu. Rev. Fluid Mech.*, 11(1):505–540, 1979.

J. Yuan. Turbulent boundary layers under irregular waves and currents: Experiments and the equivalent-wave concept. *J. Geophys. Res.: Oceans*, 121 (4):2616–2640, 2016.

J. Yuan and O. S. Madsen. Experimental and theoretical study of wave–current turbulent boundary layers. *J. Fluid Mech.*, 765:480–523, 2015.

A. Zampiron, S. Cameron, and V. I. Nikora. Secondary currents and very-large-scale motions in open-channel flow over streamwise ridges. *J. Fluid Mech.*, 887:A17, 2020.

A. Zeiler, R. Faltermeier, I. R. Keck, A. M. Tomé, C. G. Puntonet, and E. W. Lang. Empirical mode decomposition - An introduction. In *The 2010 Int. Joint Conference on Neural Networks (IJCNN)*, pages 1–8. IEEE, 2010.

J. S. Zhang, Y. Zhang, D. S. Jeng, P. L. F. Liu, and C. Zhang. Numerical simulation of wave–current interaction using a RANS solver. *Ocean Eng.*, 75: 157–164, 2014.

X. Zhang and R. Simons. Experimental investigation on the structure of turbulence in the bottom wave-current boundary layers. *Coast. Eng.*, 152: 103511, 2019.

Q. Zhong, D. Li, Q. Chen, and X. Wang. Coherent structures and their interactions in smooth open channel flows. *Environ. Fluid Mech.*, 15(3): 653–672, 2015.

Q. Zhong, Q. Chen, H. Wang, D. Li, and X. Wang. Statistical analysis of turbulent super-streamwise vortices based on observations of streaky structures near the free surface in the smooth open channel flow. *Water Resour. Res.*, 52(5):3563–3578, 2016.

“When I meet God, I’m going to ask him two questions: why relativity? And why turbulence? I really believe he’ll have an answer for the first.”
Werner Karl Heisenberg, Nobel Prize in Physics (1932)